저작자표시-비영리-변경금지 2.0 대한민국

이용자는 아래의 조건을 따르는 경우에 한하여 자유롭게

- 이 저작물을 복제, 배포, 전송, 전시, 공연 및 방송할 수 있습니다.

다음과 같은 조건을 따라야 합니다:

저작자표시. 귀하는 원저작자를 표시하여야 합니다.

비영리. 귀하는 이 저작물을 영리 목적으로 이용할 수 없습니다.

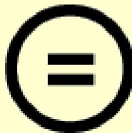

변경금지. 귀하는 이 저작물을 개작, 변형 또는 가공할 수 없습니다.

- 귀하는, 이 저작물의 재이용이나 배포의 경우, 이 저작물에 적용된 이용허락조건을 명확하게 나타내어야 합니다.
- 저작권자로부터 별도의 허가를 받으면 이러한 조건들은 적용되지 않습니다.

저작권법에 따른 이용자의 권리는 위의 내용에 의하여 영향을 받지 않습니다.

이것은 이용허락규약(Legal Code)을 이해하기 쉽게 요약한 것입니다.

Disclaimer

dCollection

이학박사 학위논문

Investigation of transparent *p*-CuI and *n*-stannate thin-film diodes for a UV photodetector application

UV 광검출기 적용을 위한 *p*-CuI 및 *n*-stannate
박막 다이오드의 연구

2022년 8월

서울대학교 대학원

물리천문학부

이 정 혁

Investigation of transparent *p*-CuI and *n*-stannate thin-film diodes for a UV photodetector application

UV 광검출기 적용을 위한 투명 *p*-CuI 및 *n*-stannate 박막 다이오드의 연구

지도 교수 김 기 훈

이 논문을 이학박사 학위논문으로 제출함

2022년 8월

서울대학교 대학원

물리천문학부

이 정 혁

이정혁의 이학박사 학위논문을 인준함

2022년 8월

위 원 장 ______ 이 규 철 ______ (인)

부위원장 ______ 김 기 훈 ______ (인)

위 원 ______ 홍 승 훈 ______ (인)

위 원 ______ 최 현 용 ______ (인)

위 원 ______ 이 상 렬 ______ (인)

Investigation of transparent *p*-CuI and *n*-stannate thin-film diodes for a UV photodetector application

Jeong Hyuk Lee

Supervised by

Professor Kee Hoon Kim

A dissertation Submitted to the Faculty of

Seoul National University

in Partial Fulfillment of

the Requirements for the Degree of

Doctor of Philosophy

August 2022

Department of physics and Astronomy

Graduate School

Seoul National University

Abstract

Over the past decades, transparent conducting materials (TCMs) especially for the transparent conducting oxides (TCOs), such as binary oxides of ZnO, In_2O_3, TiO_2, SnO_2, etc., have been commonly used for many optoelectronic device applications in solar cells, field-effect transistors (FETs), and light-emitting diodes (LEDs). Although those materials showed good performance, they still have a few improvement points, for instance, high-temperature thermal stability and room-temperature mobility. To develop the enhanced device, we searched for a new TCO system and finally found donor-doped $BaSnO_3$ (BSO) that has wide-bandgap energy of 3.0 eV, the high room-temperature electron mobility of 320 $cm^2 V^{-1} s^{-1}$ at an electron carrier density of ~10^{20} cm^{-3}, and outstanding thermal stability at high temperature among various perovskite oxides.

In order to exploit such superior properties, we tried to investigate the La-doped $BaSnO_3$ (LBSO) thin films on perovskite oxide substrates, such as $SrTiO_3$(001) (STO), epitaxially grown by pulsed-laser deposition (PLD) method. The resultant LBSO films exhibit high electron mobility of about 70 $cm^2 V^{-1} s^{-1}$, though the mobility has shown much lower than that of single-crystal due to a mainly large lattice mismatch of about 5% between the LBSO film and the STO substrate. Furthermore, the LBSO films show good thermal stability, which is consistent with the single-crystal feature, and have degenerate semiconductor behavior, which means constant carrier concentration as a function of temperature.

To facilitate those excellent properties, tons of research for the BSO-based FETs and *pn* diodes as fundamental building blocks of optoelectronic devices have been studied very recently. Especially for the *pn* junctions, various BSO-based *pn* diodes have been tried to realize the high-performing devices. However, the *p*-type materials as a counterpart of *n*-

type TCOs commonly show very low hole carrier density, typically less than 10^{15} cm^{-3} at room temperature, presumably due to the low carrier activation. Moreover, it exhibited rather a small hole mobility that can't be measured by the conventional Van der Pauw technique. The main bottleneck of the *p*-type oxides is that the oxygen *p* orbitals in the top valance band induce a flat band to result in a large hole effective mass. To achieve a good *pn* junction, meaning that the diode interface is clean without any defects, it would be desirable to figure out which material system is appropriate for the donor-doped BSO system. However, very limited studies have been reported so far, due to the above reasons. Therefore, once the BSO-based transparent *pn* diodes with a novel *p*-type TCM are realized, it will definitely be valuable for next-generation integrated devices.

The γ-phase of copper iodide (CuI) with direct wide-bandgap energy (E_g) of 3.1 eV has recently attracted numerous attention as an emergent transparent *p*-type semiconductor. One of the reasons for this is that the CuI shows high hole mobility, being higher than that of other conventional *p*-type oxides, presumably due to the iodine *p* orbitals resulting in a smaller hole effective mass than the oxides. In terms of conductivity only, there are many *p*-type oxides with high conductivity, however, those materials usually have low transparency, which can be a bottleneck to optoelectronic applications. Thus, the figure of merit (FOM) of a semiconductor, which is defined as the ratio of the electrical conductivity to the optical absorption coefficient, is important for devices. In other words, the high FOM means that the material shows a high electrical conductivity as well as high transparency since the absorption increases with the decrease of the transmittance. In this regard, the CuI is a promising *p*-type TCM for applying various applications, such as FET, LED, and UV photodetector.

In order to grow the CuI thin films, various deposition techniques have been reported,

including iodization of sputtered Cu film, pulsed-laser deposition (PLD), thermal evaporation, spin-coating, etc. Among those techniques, the most conventional method was the iodization of sputtered Cu film. However, the iodized films have shown a very rough surface due to the large volume expansion, being able to induce deterioration of the clean interface. The thermal evaporation of CuI powder gives the high-quality CuI film with a high hole carrier density, high hole mobility, and high transparency. To study the physical properties of CuI films grown, we tried to make the CuI films by two methods; thermal evaporation and iodization of Cu film.

To further investigate the diode properties, *p*-type CuI film with a (111) orientation was grown by the thermal evaporation on top of an epitaxial *n*-type $BaSnO_{3-\delta}$ (001) film on $SrTiO_3$(001) substrate deposited by the PLD for realizing transparent CuI/$BaSnO_{3-\delta}$ heterojunction. As the CuI film thickness increases from 30 to 400 nm, the hole carrier density has been decreased from 6.0×10^{19} to 1.0×10^{19} cm^{-3}. According to the change of the hole carrier density, the interesting thing is that the corresponding current rectification ratio of the *pn* diode has been enhanced from ~10 to ~10^6. To understand that diode transport mechanism, an energy band diagram exhibiting the type-II band alignment was proposed to describe the heterojunction diode. According to the Anderson heterojunction diode model, the thickness-dependent current rectification ratio resutls from the shift of the built-in potential due to the change in hole carrier density. Consequently, the origin of the best-performing CuI/$BaSnO_{3-\delta}$ diode, which exhibits a high current rectification ratio of 6.75×10^5 at ±2 V and an ideality factor of ~1.5, was understood systematically.

In order to reach the high current rectification ratio of BSO-based *pn* diodes, it is required a high-quality BSO film with an epitaxial growth mode on a lattice-matched substrate such as STO, and a rather high growth temperature of above 800 °C. Such a

constraint should be overcome for practical applications, such as low-cost and flexible devices. Thus, it will be worthwhile to realize a heterojunction diode consisting of an alternative *n*-type film that can be grown at a relatively low-temperature growth condition comparable to that of the CuI film. For this motivation, we tried to find a new *n*-type material system for practical applications and adopted a novel *n*-type amorphous semiconductor SiZnSnO (SZTO) film, which shows a high optical bandgap of 3.7 eV with field-effect mobility of about 38 $cm^2 V^{-1} s^{-1}$. Furthermore, the electrical performance of the *n*-type SZTO film under ambient conditions is much more stable than that of the most well-known amorphous *n*-type InGaZnO (IGZO) film, presumably due to reduced oxygen vacancies by strong Si-O binding energy than the Ga-O. In addition to the better oxygen controllability, the *n*-type SZTO film is composed of non-toxic and abundant compounds of Si and Sn. Therefore, the SZTO system is desirable as a transparent passive layer to fabricate practical devices combined with the CuI system.

The advanced application direction of the *p*-CuI/*n*-SZTO diode is a self-powered UV photodetector using the direct bandgap feature of the CuI. The self-powered UV photodetector refers to that the *pn* diode can generate sufficient photocurrent from the UV light without any external power. Nowadays, various photodetectors made of *p*-CuI and *n*-type TCMs have been investigated actively. Because, once a CuI-based photodetector is realized, UV performance of the photodetector, such as responsivity and reproducibility, is to be expected high under UV conditions. Thus, we tried to test the photodetector performance with the high-performing *p*-CuI/*n*-SZTO diode to check whether the diode can be a promising platform for an optoelectronic device. Moreover, to understand a device operation principle, a qualitative study for the diode energy band diagram and the responsivity origin was conducted. Based on the systematic study of the CuI/SZTO diode, photocurrent experiments have been performed under self-powered conditions. Upon

varying with the junction area, the photodetector performance of the CuI/SZTO photodetector has been changed by the pinhole effects, which are the main source of the leakage current.

Based on all the experimental investigations, we proposed that the CuI film is a promising *p*-type semiconductor, being able to grow the film at room temperature, and the stannate films are new *n*-type semiconductors to realize CuI-based optoelectronics, especially for the UV PD. The realized *p*-CuI/*n*-SZTO diode can be utilized as a self-powered UV PD. Another potential merit of the CuI/SZTO PD is the capability of flexible devies since the CuI film exhibits high film quality on top of amorphous materials. Therefore, as novel semiconductors and its optoelectronic device, the CuI/SZTO diode is desirable to widely investigate its physical properties systematically.

Keywords : barium stannate ($BaSnO_3$), Si-suppressed zinc-tin stannate (SiZnSnO), copper iodide (CuI), *pn* heterojunction diode, current rectification ratio, self-powered UV photodetector

Student Number : 2015-20346

Contents

Abstract i

Contents vi

List of Tables ix

List of Figures x

Chapter 1 Introduction 1

1.1 Transparent conducting materials 1

1.2 Transparent perovskite barium stannate : $BaSnO_3$ 2

1.3 A new promising *p*-type semiconductor : copper iodide (CuI) 3

Chapter 2 Physical properties of transparent *p*-CuI/*n*-$BaSnO_{3-\delta}$ heterojunction diodes 6

2.1 Overview 6

2.2 CuI film growth I : iodization of sputtered Cu film 9

2.3 CuI film growth II : evaporated CuI film 12

2.4 Integration of *p*-CuI and *n*-BSO thin films for transparent heterojunction diodes 18

2.5 Current-voltage (*IV*) characteristics of the realized *p*-CuI/*n*-BSO diodes 22

2.6 A high current rectification ratio of the *p*-CuI/*n*-BSO diode among BSO-based

heterojunctions 2 9

2.7 Summary 3 0

Chapter 3 Characteristics of a transparent *p*-CuI/*n*-SiZnSnO heterojunction diode 3 2

3.1 Overview 3 2

3.2 Introduction of a novel *n*-type amorphous semiconductor : SiZnSnO 3 3

3.3 Annealing effects on the evaporated CuI films 3 5

3.4 Realization of transparent *p*-CuI/*n*-SZTO diodes 3 9

3.5 Current rectifying behavior of the *p*-CuI/*n*-SZTO diodes 4 4

3.6 Diode curve fitting simulation 5 1

3.7 Comparison of a high current rectification ratio of the *p*-CuI/*n*-SZTO heterojunction diode 6 0

3.8 The electronic band alignment and the type-II energy band diagram 6 2

3.9 Summary 6 5

Chapter 4 Investigation of a self-powered CuI/SiZnSnO UV photodetector 67

4.1 Overview 67

4.2 Establishment of the photocurrent measurement setup 68

4.3 Characterization of the CuI/SZTO photodetector 70

4.4 Photocurrent of CuI/SZTO diode under the self-powered mode at 0 V 73

4.5 The physical origin of the responsivity curve on the CuI/SZTO photodetector 80

4.6 Enhancement of the responsivity by reducing pinhole effects on the CuI/SZTO photodetector 86

4.7 Various photodetector performances on the improved CuI/SZTO diode 89

4.8 Comparison of the high responsivity of the self-powered CuI/SZTO UV photodetector 93

4.9 Summary 95

References........97

Appendix A Attempt to develop the membrane transferring technique for oxide free-standing films........101

A.1 Overview........ 101

A.2 Experimentals 103

A.3 Results and discussions 105

A.4 Summary 111

A.5 References 111

List of publications 113

국문 초록 115

List of Tables

Table 2.1 Information of figure of merit (FOM) for various *p*-type TCMs........................ 8

Table 2.2 Numerical fitting parameters obtained by diode curve fitting for the *IV* curve of the *p*-CuI/*n*-BSO heterojunction diode.. 26

Table 2.3 Input parameters of the Anderson diode model for the *p*-CuI/*n*-BSO heterojunction, where m_o is the electron mass... 27

Table 3.1 Summary of diode parameters for various different *pn* junctions, consisting of the *p*-CuI films. 62

Table 3.2 Various input parameters of the Anderson heterojunction diode model for the annealed *p*-CuI/*n*-SZTO diode, where m_o is the electron mass. 64

Table 4.1 Summary of various photodetector parameters for CuI-based self-powered UV photodetectors. 93

List of Figures

Figure 1.1 Crystal structure of cubic perovskite for $BaSnO_3$ with a lattice constant of 4.116 Å. 3

Figure 1.2 Crystal structure of zincblende for CuI with a lattice constant of 6.054 Å. 4

Figure 2.1 Summary of the figure of merit (FOM) at various *p*-type TCMs, including CuI and other *p*-type oxides. 7

Figure 2.2 Schematic procedure of CuI film making using iodization of sputtered Cu films. 9

Figure 2.3 Cu and CuI films on the glass substrate before and after the iodization process. 10

Figure 2.4 Transmittance as a function of wavelength of the bare glass substrate and the CuI(100 nm)/glass. 11

Figure 2.5 Surface topography images of Cu/glass and CuI/glass with root-mean-square surface roughness values and surface profile along the red dashed lines in each image. 11

Figure 2.6 X-ray diffraction (XRD) patterns for metal Cu and polycrystalline CuI film on the glass substrate. 12

Figure 2.7 A photograph of evaporated CuI film on the glass substrate with a film thickness of 120 nm. 13

Figure 2.8 (a) Optical transmittance data on evaporated CuI(120 nm)/glass and Cu-iodized CuI(100 nm)/glass. (b) The absorption coefficient of the CuI film estimated using the Tauc plot. 13

Figure 2.9 Surface morphology of the CuI(120 nm) film on the glass substrate grown by the thermal evaporation technique. The bottom panel exhibits a surface profile along the red dashed line in the figure. 15

Figure 2.10 X-ray θ- 2θ scan results of CuI(120 nm)/glass, which exhibit the preferential alignment of the CuI film along the (111) plane. 16

Figure 2.11 Current-voltage (*IV*) curve of the CuI film for confirming the linear behavior, indicating the ohmic contacts between the film and tungsten probe tips. 17

Figure 2.12 Hole carrier density (p), electrical resistivity (ρ), and hole mobility (μ_h) as a function of the thickness of the CuI films (t_{CuI}) grown on glass substrate by the thermal evaporation method. 18

Figure 2.13 Current-voltage (IV) curve of the BLSO film to check the ohmic contact between the film and tungsten probe tips. 20

Figure 2.14 Schematic structure and actual photograph of the fabricated CuI/BSO/BLSO/STO sample without metallic electrode depositions. 20

Figure 2.15 Optical transmittance spectra of STO substrate (black dotted line), BSO/BLSO/STO (red dashed line), and CuI/BSO/BLSO/STO (blue solid line). The Thickness of each layer is 0.5 mm, 100 nm, 100 nm, and 120 nm for STO substrate, BSO, BLSO, and CuI films, respectively. 21

Figure 2.16 XRD θ - 2θ scan results of CuI/BSO/BLSO/STO, CuI/STO, and CuI/glass specimens, all of which show the preferential orientation of the CuI (111) plane regardless of bottom materials. 22

Figure 2.17 The current density-voltage (jV) curves of the *p*-CuI/*n*-BSO heterojunction diodes for various CuI film thicknesses (t_{CuI}). 23

Figure 2.18 The current rectification ratio (I_F/I_R) and built-in potential (V_{bi}) in the *p*-CuI/*n*-BSO diodes at various t_{CuI}. 24

Figure 2.19 the current-voltage (IV) and the current-density voltage (jV) curves of the *p*-CuI(400 nm)/*n*-BSO(100 nm) diode. Red solid lines in the IV curve represent linear extrapolation to determine the turn-on voltage. The red dotted lines in the jV curve display the fitting curves based on the diode equation (Equation 2.6). 25

Figure 2.20 A proposed energy band diagram of the *p*-CuI(400 nm)/*n*-BSO heterojunction diode, exhibiting the best performance. 27

Figure 2.21 The cartoon figure of the electronic structure of *p*-CuI/*n*-BSO heterojunction with the demonstration of free carriers. 28

Figure 2.22 Comparison of the current rectification ratios (I_F/I_R) for various BSO-based *pn* heterojunction diodes. 29

Figure 3.1 Room temperature hole carrier density p, electrical resistivity ρ, and hole mobility μ_h as a function of the CuI film thickness t_{CuI}. The black and red symbols represent the data of the as-grown and annealed CuI films on glass substrates, respectively. In the case of annealed CuI(11 nm)/glass, Hall resistivity could not be measured due to the high resistance. 36

Figure 3.2 X-ray θ - 2θ and ω scan results of representative CuI(54 nm)/glass and FWHM values as a function of t_{CuI} before and after the thermal annealing. 37

Figure 3.3 Surface morphology of as-grown and annealed CuI(140 nm)/glass measured by AFM in a contact mode. The bottom panels display surface line profiles along the green dotted lines presented in the images. A root-mean-square (rms) surface roughness in the whole area of 2 μm × 2 μm decreases from 5.46 nm to 4.03 nm after

the thermal annealing. 38

Figure 3.4 Current-voltage (IV) characteristics of Au/Ni/CuI and ITO/SZTO/SiO_2/Si, respectively. The IV curves were measured at room temperature without any light exposure. Schematic drawings are presented the measurement configuration of the two-probe contact method. 39

Figure 3.5 An actual photograph and a schematic structure of the p-CuI/n-SZTO diode grown on the ITO deposited glass substrate for optical characterization. The CuI(110 nm)/SZTO(27 nm) (orange dashed line) were deposited on top of the ITO/glass substrate (green dashed line), exhibiting optical transparency. 40

Figure 3.6 Optical transmittance (T_λ), reflectance (R), and absorbance (A) spectra of the CuI(110 nm)/SZTO/ITO/glass. The black solid line represents the T_λ of a bare glass substrate (t = 1 mm).. 41

Figure 3.7 XRD θ - 2θ scan results of the CuI(110 nm)/SZTO/ITO/glass and SZTO/ITO/glass. The CuI film exhibits the preferential orientation of the CuI (111) plane and the additional peaks represent a polycrystalline ITO film indicated as I. 43

Figure 3.8 A schematic structure of the p-CuI/n-SiZnSnO (SZTO) diode grown on the ITO deposited glass substrate, which was used for electrical characterization. The CuI film of circular shape disk with a diameter of 50 μm was fabricated in two thicknesses of 20 nm and 140 nm, while the thicknesses of SZTO and ITO films were fixed as 27 nm and 50 nm, respectively. The metallic Au/Ni (t = 50/5 nm) films were subsequently deposited on top of the CuI film using the stencil mask. 44

Figure 3.9 (Top) The current-voltage (IV) curve in a linear scale and (bottom) the corresponding current density-voltage (jV) curve in a semi-log scale of the as-grown (left) and the annealed (right) CuI(140 nm)/SZTO diode, respectively. The range and the green solid lines in the IV curves represent the linear extrapolation to determine the turn-on voltage of a diode, $V_{turn\text{-}on}$, while the range and the green dashed lines in the jV curves correspond to the diode fitting results obtained by the Shockley diode equation (Equation 3.9). 46

Figure 3.10 Surface topography images measured by AFM in a contact mode for the samples of (left) CuI(54 nm)/glass, (middle) CuI(110 nm)/SZTO/ITO/glass, and (right) SZTO/ITO/glass. The bottom panels show the line profiles along the green dotted lines in the images. 47

Figure 3.11 The current-voltage IV curve (top) in a linear scale and the current density-voltage (jV) curve (bottom) in a semi-log scale of (left) the as-grown and (right) the annealed CuI(20 nm)/SZTO diode. The orange and the green solid lines in the IV curves represent the linear extrapolation to determine the turn-on voltage $V_{turn\text{-}on}$ of a diode, while the dashed line in the jV curves corresponds to the diode fitting results based on Equation 3.9... 51

Figure 3.12 Summary of various diode parameters; the current rectification ratio I_F/I_R, the offset current I_o, the reverse saturation current I_s, the ideality factor η, the series

resistance R_s, and the parallel resistance R_p. Black and red colors represent the data of the as-grown and annealed diode, respectively. All the parameters are estimated by fitting the *IV* curve results with Equation 3.9. Error bars represent the least square fitting error. The other parameters exhibit low fitting errors of less than 5 %, except for the parallel resistance. 52

Figure 3.13 Curve fitting simulation results with the η variation. The other diode parameters were fixed during the change in the η. The matched η with the measured curve is 2.89. 55

Figure 3.14 Curve fitting simulation results with the I_s variation. The other diode parameters were fixed during the change in the I_s. The matched I_s with the measured curve is 0.06 fA. 56

Figure 3.15 Curve fitting simulation results with the I_o variation. The other diode parameters were fixed during the change in the I_o. The matched I_o with the measured curve is 5.89 pA........ 57

Figure 3.16 Curve fitting simulation results with the R_s variation. The other diode parameters were fixed during the change in the R_s. The matched R_s with the measured curve is 11.5 kΩ. 58

Figure 3.17 Curve fitting simulation results with the R_p variation. The other diode parameters were fixed during the change in the R_p. The matched R_p with the measured curve is 1960 GΩ........ 59

Figure 3.18 Comparison of the current rectification ratios I_F/I_R of various heterojunction diodes composed of the *p*-CuI film. The color indicates different *n*-type films for the *pn* diodes and here high I_F/I_R values over 10^5 are summarized only. The I_F/I_R of the CuI/SZTO diode is obtained by the fitted values of I_F at +2 V and I_R at -2 V. The I_F/I_R of the $CuI_{1-x}Br_x$/IGZO diode is estimated by the measured I_F at +1.5 V and the fitted reverse saturation current [81]. The I_F/I_R of CuI/ZnO [29, 64], CuI/IGZO [80], and CuI/$BaSnO_{3-\delta}$ [58] diodes are calculated from the measured data at ±2 V............. 60

Figure 3.19 Electronic band alignment of several wide bandgap materials, including ITO, BSO, IGZO, CuI, and SZTO. The band energies of those materials are aligned at the vacuum energy level $E_{vac} = 0$........ 63

Figure 3.20 A proposed energy band diagram of the annealed CuI(140 nm)/SZTO diode representatively, based on the Anderson heterojunction diode model, exhibiting the type-II band alignment. 65

Figure 4.1 Schematic configuration of the built photocurrent setup. The specimen is loaded using the micro probestation, which can be directly attached to the monochromator exit port. The actual photograph demonstrates the sample loading during the light illumination at 400 nm........ 68

Figure 4.2 (left) Light power density which measured at the monochromator exit port and optical fiber, respectively. (right) The measured responsivity curve of the commercial

Si PIN diode compared to the spec sheet data, where R_λ is the responsivity, I_{ph} is the photocurrent, I_{light} is the current under the light illumination, I_{dark} is the dark current, P_{in} is the incident light power, S is the effective illumination area. 69

Figure 4.3 Schematic diagram of the frequency-dependent photocurrent measurement setup. The same light source of the Xe arc lamp and the monochromator as the wavelength switching system was used to generate the UV light. 70

Figure 4.4 Schematic structure and actual photograph of CuI(110 nm)/SZTO(27 nm)/ITO/glass for photoresponse measurements. 71

Figure 4.5 XRD θ - 2θ scan results of the CuI(110 nm)/SZTO/ITO/glass and SZTO/ITO/glass. The CuI film exhibits the preferential orientation of the CuI (111) plane and the additional peaks represent a polycrystalline ITO film indicated as *I*. 72

Figure 4.6 Top-view FE-SEM images of CuI/SZTO/ITO/glass specimen at different measured spots. Many grains with an average grain size of about 51.1 nm and the non-uniform large-size pinholes are observed. 72

Figure 4.7 The current-voltage (*IV*) curves under various illumination wavelengths in a full-scale (left) and an enlarged scale (right). The *IV* curves are nearly overlapped due to the high leakage current induced by the pinholes. 73

Figure 4.8 (left) The photocurrent and the incident light power density as a function of illumination wavelength. (right) The spectral responsivity at zero bias condition, which is a self-powered mode. The responsivity curve is obtained in Equation 4.1 by considering the effective illumination area S of the sample as 5 mm × 4 mm. 74

Figure 4.9 (left) Oscilloscope waveforms of the photovoltage switching on and off on the CuI/SZTO photodetector varying with the light intensity. The photo voltage measurements were conducted at 0 V for self-powered conditions under the 365 nm illumination at 1.4 Hz. (right) The measured photo voltage as a function of the incident light power density. The light power density was calibrated by the effective light illumination area of 5 mm × 4 mm. The red solid line represents the power-law curve fitting results with the exponent information. 75

Figure 4.10 The quantitative photo voltage data as a function of time for checking the long-term stability of the CuI/SZTO photodetector. The photo voltage preserved in the air was decreased, presumably due to the high humidity between 4 - 6 weeks. Reproducibility of the photo voltage was confirmed by preserving the photodetector in a desiccator. 77

Figure 4.11 (left) A peak-to-peak photo voltage measured by oscilloscope and lock-in amplifier as a function of the light modulation frequency. The measurements were performed at 0 V under 365 nm illumination. The cutoff frequency f_{3dB} bandwidth of the amplitude is estimated as 57.1 Hz as shown in the blue dashed line. (middle) A root-mean-square voltage R, X, and Y values and (right) the phase shift with a variation of frequency in the lock-in amplifier. The red dashed line represents the saturation line of the phase shift. 79

Figure 4.12 (left) The absorption coefficient of CuI/glass and SZTO/ITO/glass. The transmittance and reflectance measurements were conducted using a UV-VIS-NIR spectrometer. The absorption coefficient was calculated by using Equation 4.7. Film thicknesses of each layer are 54 nm, 27 nm, 50 nm, and 1 mm for the CuI, SZTO, ITO, and glass substrate, respectively. (right) Comparison of the responsivity to the absorption coefficient on the CuI/SZTO photodetector. The absorption coefficient is obtained from the measured extinction coefficient by ellipsometry data. 81

Figure 4.13 Various possible transitions of interband, trap-assisted, and Auger. Here, E_C, E_V, E_d, E_a, and E_t represent the conduction band offset, the valance band offset, the donor level, the acceptor level, and the trap level, respectively. 83

Figure 4.14 Calculated excitation rate by considering the intrinsic inter-band transition. The CuI is a direct bandgap material, so the CuI band was assumed as a parabolic band at Γ-point. 84

Figure 4.15 (left) PL spectra on the CuI/glass, SZTO/ITO/glass, and CuI/SZTO/ITO/glass. (right) Peak deconvolution result of the CuI/SZTO/ITO/glass PL signal. The envelope function is well-matched with the measured data. 85

Figure 4.16 Schematic structures and corresponding photographs for the large- and the small-size CuI/SZTO photodetectors. The lateral junction areas are 5 mm × 4 mm and $\pi \times (50\ \mu m)^2$ for the large-size and the small-size junction, respectively. 87

Figure 4.17 Current-voltage (*IV*) curves in a semi-log scale (left) and the enlarged *IV* curves in a linear scale (right) under dark, 300 nm, and 350 nm illumination conditions. The resultant *IV* curves in the semi-log scale under the UV light illumination clearly show the upper-right shift by the photocarrier generation. The I_{sc} and V_{oc} represent short-circuit current and open-circuit voltage, respectively. 87

Figure 4.18 (left) Photocurrent and light power density as a function of wavelength. The photocurrent was measured on the CuI/SZTO/ITO/glass structure by the bottom-side light illumination. The light power density was checked after passing through the SZTO/ITO/glass layers using a power meter. (right) Comparison of responsivity curve on the CuI/SZTO photodetectors with different junction areas. The small CuI/SZTO photodetector shows better performance. *S* represents the effective illumination area. 88

Figure 4.19 (left) The photocurrent with a power-law fitting curve and the linear dynamic range (LDR) as a function of incident light power density. The red solid line without symbols represents the power-law fitting result. The power-law exponent was estimated as 0.96, meaning that the photocurrent is directly proportional to the input light with a slight decrease of the photocurrent due to defects. (right) The LDR refers to the capability of the photocarrier generation of the photodetector. A high LDR value represents that the photodetector can effectively generate photocurrent when the light is illuminated. 89

Figure 4.20 (left) Photo voltage as a function of the light modulation frequency measured by two techniques, oscilloscope and lock-in phase-sensitive detection. A root-mean-square voltage R measured by the PSD has been converted to peak-to-peak based on

the oscilloscope waveforms. The blue dashed line represents the photodetector cutoff frequency bandwidth. (middle) The measured photovoltages R, X, and Y by lock-in and (right) phase shift upon varying with the light modulation frequency. 90

Figure 4.21 Comparison between the responsivity and the external quantum efficiency (EQE) as a function of wavelength. The EQE is obtained in Equation 4.11. 92

Figure 4.22 Comparison of responsivity on various CuI-based self-powered UV photodetectors. The summarized photodetectors have been made of *p*-CuI and *n*-type various materials in various forms. 94

Figure A.1 Schematic procedure of oxide membrane making process and an actual photograph of the obtained free-standing BLSO film on the PPC/PDMS polymer supports. 104

Figure A.2 The BAO target before (left) and after (right) the reconstruction process. 104

Figure A.3 XRD θ - 2θ scan results of BLSO free-standing film on the PPC/PDMS polymer support after the release process. 106

Figure A.4 (left) A schematic structure and actual photographs of the BLSO free-standing film for electrical measurements. (right) A microscope image, which has lots of cracks in the film, after the Hall effect measurements. The scale bar represents a 200 μm length. 107

Figure A.5 Electrical resistivity (ρ), sheet resistance (R_s), and electron mobility (μ) of BLSO films on SAO/STO, BAO/STO, and STO substrates as a function of electron carrier density (n). The inset presents a schematic structure of the rigid BLSO sample. 107

Figure A.6 Photograph of hand-made membrane transferring manipulator attached to the *xyz* micro positioner. 108

Figure A.7 Film thicknesses of the BZO film as a function of laser shots. The pulse shot was calibrated using the AFM apparatus. It confirms that one layer of BZO film requires 57 shots by PLD. 109

Figure A.8 XRD θ - 2θ and ω scan results of the BZO film on the STO subsrtate. The BZO film exhibits an epitaxial growth feature on the STO substrate with a narrow FWHM value in the rocking curve. 110

Figure A.9 Schematic structure and actual photograph of the BLSO free-standing film with the BZO capping layer on the PPC/PDMS polymer supports. 110

Chapter 1 Introduction

1.1 Transparent conducting materials

Over the past decades, transparent conducting materials (TCMs) especially for the transparent conducting oxides (TCOs), such as ZnO, In_2O_3, TiO_2, SnO_2, etc. [1], [2], have been commonly used for many optoelectronic devices in field-effect transistors (FETs) [3], light-emitting diodes (LEDs) [4], and solar cells [5].

The most common *n*-type TCO is the Sn-doped In_2O_3 (ITO), which has been widely used for more than six decades for industrial and aacdemic purposes as a passive transparent electrical component [6]. Other *n*-type TCOs, such as the F-doped SnO_2 [7] and Al-doped ZnO [8], have been adopted. These kinds of TCOs have typical electron carrier density (n) from 10^{18} to 10^{21} cm^{-3} and electron mobility (μ_n) from 10 to 100 cm^2 V^{-1} s^{-1}, depending on the growth methods and the material properties. The relatively large mn values are attributed to the nature of the electronic band structure of those *n*-type TCOs, in which the conduction band is usually composed of spatially delocalized by metallic *s* orbitals to result in the large dispersion as well as the low electron effective mass. Such behavior is generally observed in oxide materials with the cations having the closed-shell electron configurations of $4s^0$ or $5s^0$ [9], [10]. For the most favorable material ITO as one example, the electronic band structure is quite dispersive for the conduction band, which is composed of mainly In 5*s* orbital [11]. Such a large dispersion and a small electron-effective mass are required to reach a high electrical conductivity.

However, these various *n*-type materials still have some limitations, particularly in their stability at high temperatures and electrical mobility near room temperature [12]. It has boosted demands for finding alternative TCOs, being able to show better quality. For

instance, the long-term stability of oxide-based electronics especially for operating in the air has been often degraded by oxygen molecules in *pn* junctions and FETs [13]. Such an unstable electrical characteristic is probably originated from oxygen reactivity at high temperatures, inducing various unavoidable properties, such as leakage current and hysteresis. Furthermore, the high μ_n is a crucial parameter for realizing fast devices since the movement of electrons basically decides the operation speed of the devices [14], [15].

1.2 Transparent perovskite barium stannate : $BaSnO_3$

The perovskite oxide material system is a promising one, which shows various interesting physical properties of photovoltaic effects [16], [17], superconductivity [18], [20], magnetoresistance [21], ferroelectricity [22], [23], and multiferroicity [24], [25], etc. Numerous researches have been actively reported to facilitate superior physical properties of perovskite oxide materials. In this regards, ten years ago, we found that a new TCO system, i.e. donor doped $BaSnO_3$ (BSO) with a wide band gap energy of 3.0 eV, exhibits high electron mobility up to 320 $cm^2\ V^{-1}\ s^{-1}$ at an electron carrier density of $\sim 10^{20}$ cm^{-3} among perovskite oxides at room temperature and superior thermal stability [22], [26], [27]. The BSO has an ideal cubic perovskite structure of $Pm\bar{3}m$ space group with a lattice constant of 4.116 Å as shown in Figure 1.1.

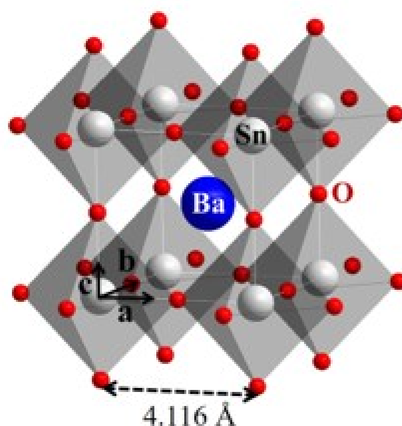

Figure 1.1 Crystal structure of cubic perovskite for $BaSnO_3$ with a lattice constant of 4.116 Å.

The stannate cubic structure is determined by a three-dimensional framework of corner-sharing SnO_6 octahedra, in which the Sn-O-Sn bonding angle is close to 180 °. The Sn-O-Sn bonding gives rise to an enhanced electron hopping process between neighboring Sn sites, contributing to the large conduction band dispersion. Moreover, the thermal stability of La-doped BSO (LBSO) shows a nearly constant conductivity under air conditions at a high temperature of 530 °C. It means that the BSO system can provide an opportunity to overcome the thermal instability problems of oxide electronics. Furthermore, LBSO thin films grown by pulsed laser deposition (PLD) methods exhibit good thermal stability at a high temperature as well as a high μ_n of about 70 $cm^2\ V^{-1}\ s^{-1}$ grown on $SrTiO_3$(001) (STO) substrates, though its mobility is lower than that of single crystals, presumably due to the threading dislocations by lattice misfit between the LBSO film and the STO substrate. Those versatile physical properties of the LBSO film have been attracting surge for a new optoelectronic devices.

1.3 A new promising *p*-type semiconductor : copper iodide

(CuI)

Although copper iodide (CuI) was firstly reported in 1907 by K. Baedeker at University Leipzig [28], it has been recently boosted by the M. Grundmann group in 2013 that a high quality transparent *p*-type semiconductor [29]. The γ-phase CuI has a cubic zincblende structure with a lattice constant of 6.054 Å as shown in Figure 1.2. According to the electronic band structure, the difference between the valance band maximum and the conduction band minimum at Γ-point is 3.1 eV, which indicates the direct bandgap material [30].

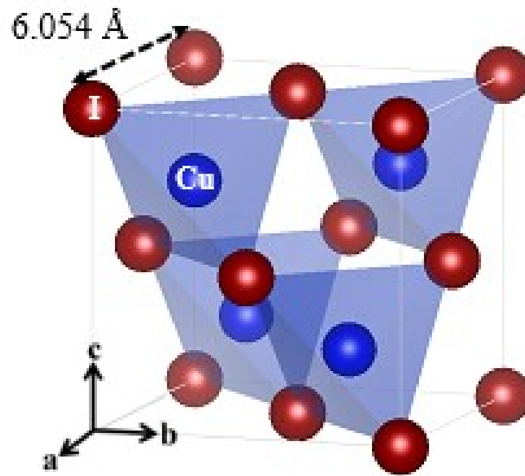

Figure 1.2 Crystal structure of zincblende for CuI with a lattice constant of 6.054 Å.

It is noted that the photon energy is directly proportional to the light frequency, which is often described in the electronvolt unit as Equation 1.1. In other words, the CuI is transparent in the visible range above 400 nm, which is the bandgap energy of 3.1 eV.

$$E(eV) = \frac{1240}{\lambda(nm)}$$ **Equation 1.1**

where E is the photon energy and λ is the wavelength.

In terms of electrical property, the positive Hall effect result says that the CuI has the p-type carrier. The hole mobility (μ_h) of γ-CuI single-crystal reaches as high as 43.9 $cm^2\ V^{-1}\ s^{-1}$ at room temperature [31], being much higher than those of conventional p-type oxides [32], [33], presumably due to the iodine p orbitals result in a smaller hole effective mass than that of oxides. Furthermore, the γ-CuI thin films show a high hole carrier density (p) of $>10^{16}\ cm^{-3}$ and a high μ_h of 25 $cm^2\ V^{-1}\ s^{-1}$ among p-type TCMs [34]. The main source of the p carrier in the CuI system is mainly copper vacancy (V_{Cu}) because it is known to be easily created as a native effect, being able to act as an acceptor to make hole carriers [30]. In order to facilitate its outstanding p-type properties, CuI thin films have been recently investigated to realize optoelectronic devices in many application fields, such as FETs [35] organic photovoltaics [36], LEDs [37], and UV photodetector [38], etc.

Chapter 2 Physical properties of transparent *p*-CuI/*n*-$BaSnO_{3-\delta}$ heterojunction diodes

2.1 Overview

The γ-CuI has been attracting surge attention as an emergent transparent *p*-type TCM with a high μ_h as well as high transparency as described in chapter 1. There are many *p*-type oxides with high conductivity, however, its transmittance their the visible range is rather low, being able to be a bottleneck for optoelectronic devices. In general, *p*-type TCOs have a flat valance band produced by oxygen 2*p* orbitals to result in the large hole effective mass. The flat band induces low hole carrier activation and the small μ_h. To overcome such a low electrical conductivity, large amounts of dopants have been inserted, recurring the low optical transparency. In this sense, the figure of merit (FOM) of a transparent semiconductor, which is defined as the ratio of the electrical conductivity to optical absorption coefficient in Equation 2.1, is a crucial parameter for device applications.

$$\mathrm{FOM} = \frac{\sigma}{\alpha} = \frac{\sigma}{1/t \ln[(1-R)^2 / T]}$$ **Equation 2.1**

where σ is the electrical conductivity, α is the absorption coefficient, t is the thickness, R is the reflectance, and T is the transmittance.

Figure 2.1 exhibits FOMs of various *p*-type TCMs, including CuI and many other *p*-type TCOs. The detailed information on each material is summarized in Table 2.1 Information of figure of merit (FOM) for various *p*-type TCMs. The high FOM value deduces high electrical as well as a high optical transparency, simultaneously, since the absorption coefficient increase with the decrease of the transmittance. It is thus likely that

the CuI exhibits a higher FOM value compared to the conventional *p*-type TCOs as a active component of various optoelectronic devices.

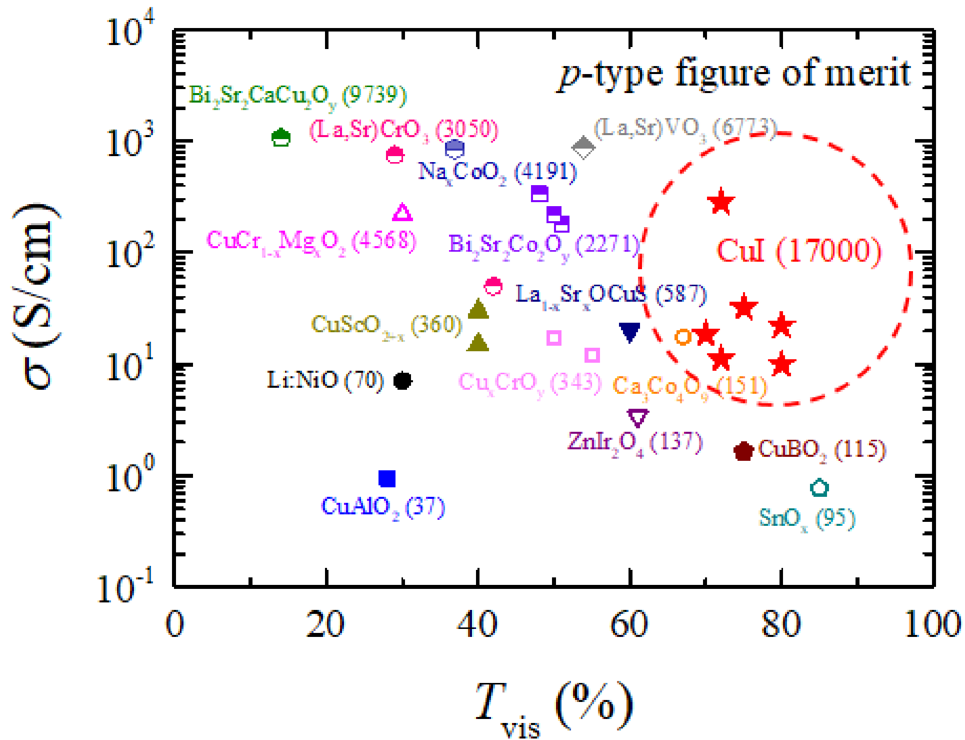

Figure 2.1 Summary of the figure of merit (FOM) at various *p*-type TCMs, including CuI and other *p*-type oxides.

Furthermore, there lately exists a surge of research attempts to fabricate CuI-based *pn* heterojunction diodes as fundamental building blocks for optoelectronic devices. In this respect, it will be worthwhile to realize the *p*-CuI/*n*-BSO heterojunction diode because the BSO-based basic devices still have lack of an appropriate *p*-type material as a counterpart of the highly conductive *n*-type TOSs. Once transparent CuI- and BSO-based *pn* diodes, it will be helpful to investigate diode behavior for practical applications. Therefore, we decided to realize totally transparent *p*-CuI/*n*-BSO heterojunction diodes for studying the capability of those materials. In this chapter, fundamental physical properties of CuI thin films grown by two deposition methods, iodization of Cu-sputtered film and thermal

evaporation, were measured for being structural, optical, and electrical. Furthermore, the successful fabrication of *p*-CuI/*n*-BSO heterojunction diodes with a high current rectification ratio has been investigated systematically. In order to analyze diode behavior, various diode parameters were examined upon changing the CuI film thickness in the diode. Finally, an energy band diagram for the heterojunction and attribute the current rectification ratio increase to the reduced diode built-in potential by the decrease of *p*.

Year	*p*-type TCMs	T_{vis} %	σ S/cm	t nm	R_s Ω/sq	FOM $(M\Omega)^{-1}$	Reference
1993	Li:NiO	30	7.1	118	12000	70	[39]
1996	CuI (sputtering)	70	18.5	100	5400	518	[40]
1997	$CuAlO_2$	28	0.95	500	21000	37	[41]
2000	$CuScO_{2+x}$	40	15	110	6000	180	[42]
2000	$CuScO_{2+x}$	40	30	110	3000	360	[42]
2001	$CuCr_{0.95}Mg_{0.05}O_2$	30	220	250	180	4568	[43]
2002	CuI (PLD)	80	10	~500	2000	2240	[44]
2002	$(La_{0.97}Sr_{0.03}O)CuS$	60	20	150	3300	587	[45]
2007	$ZnIr_2O_4$	61	3.39	200	14700	137	[46]
2007	$CuBO_2$	75	1.65	200	30300	115	[47]
2010	SnO_x	85	0.77	200	64900	95	[48]
2013	CuI (iodization)	49	5	500	4000	350	[49]
2013	CuI (evaporation)	75	32	240	1300	2670	[29]
2014	$Ca_3Co_4O_9$	67	17.5	100	5700	151	[50]
2014	$Bi_2Sr_2Co_2O_y$	51	181	50	1100	1350	[51]
2014	$Bi_2Sr_2Co_2O_y$	50	222	25	1800	801	[52]
2015	$SrCrO_3$	29	750	50	267	3050	[53]
2015	$La_{0.5}Sr_{0.5}CrO_3$	42	50	50	4000	291	[53]
2015	Cu_xCrO_y	55	12	80	10400	161	[54]
2016	CuI (DCS-iodization)	72	283	200	177	17000	[55]
2016	$Bi_2Sr_2Co_2O_y$:Au	48	333	50	600	2271	[56]
2016	Cu_xCrO_2	50	17	140	4200	343	[57]
2017	CuI (evaporation)	80	22.2	120	3750	1195	[58]
2018	$La_{0.66}Sr_{0.33}VO_3$	53.9	872	48	239	6773	[59]
2018	Na_xCoO_2	37	833	50	240	4191	[60]
2018	$Bi_2Sr_2CaCu_2O_y$	14	1063	180	52.2	9739	[61]
2019	CuI (DCMS-iodization)	72	11.1	300	3700	823	[62]

Table 2.1 Information of figure of merit (FOM) for various *p*-type TCMs.

2.2 CuI film growth I : iodization of sputtered Cu film

There exist various deposition techniques, such as iodization of sputtered Cu film, PLD, thermal evaporation, spin-coating, etc. In order to grow the CuI films, the most common method among those techniques is an iodization method of metallic Cu film deposited by often DC magnetron sputtering [29]. In our lab., the Cu film on the soda-lime glass substrate (Marienfeld) was grown by RF magnetron sputtering at 35 W for 10 min using a commercial Cu disk as source material in Ar partial pressure of 3 mTorr at 150 °C. The iodization process of Cu film is shown in Figure 2.2. The prepared metallic Cu films were put in a glass container with solid-phase iodine chunks, followed by thermal treatment at 120 °C for 15 min to sublimate the iodines. Once the Cu films react with the I_2 gas, the films have been immediately switched from Cu to CuI films. Subsequently, the vessel has been cooled using liquid nitrogen or iced water to return the I_2 gas as the iodine chunks.

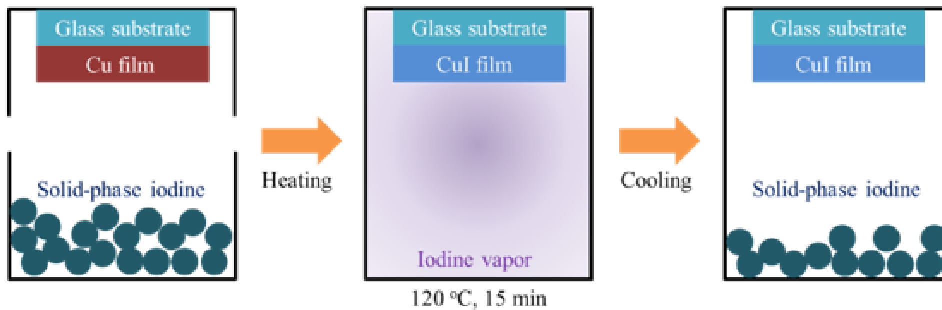

Figure 2.2 Schematic procedure of CuI film making using iodization of sputtered Cu films.

Figure 2.3 exhibits the resultant CuI film on the glass substrate after the iodization process. Film thicknesses for Cu and CuI films are about 17 nm and 100 nm, confirmed by atomic force microscopy (AFM) (NX10, Park Systems), respectively. The obtained CuI film shows a semi-transparent feature with a brownish-yellow color. To quantitatively investigate the optical property, the transmittance measurements were performed on glass

and CuI/glass samples by a UV-VIS-NIR spectrometer (Cary 5E, Varian). Transmittance data in the wavelength range from 350 nm to 550 nm is shown in Figure 2.4. Before measuring the transmittance of the CuI/glass specimen, a bare glass substrate with 1 mm thickness was tested, showing a nearly constant transmittance of 90 %.

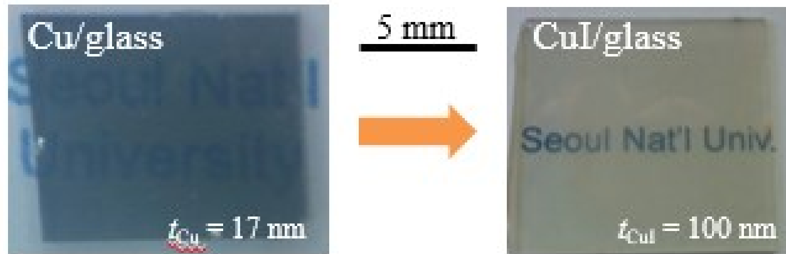

Figure 2.3 Cu and CuI films on the glass substrate before and after the iodization process.

The transmittance of the CuI film, which has a 100 nm film thickness, is 50 % at 550 nm and keeps decreasing with the decrease of wavelength, and 10 % at 350 nm, which is the consistent result with the photograph in Figure 2.3. The sharp deep of about 407 nm (3.05 eV) originated from the CuI excitonic absorption due to the high binding energy of 62 meV [29]. It is worth noting that the excitonic absorption peak often appears at slightly lower energy than the bandgap energy.

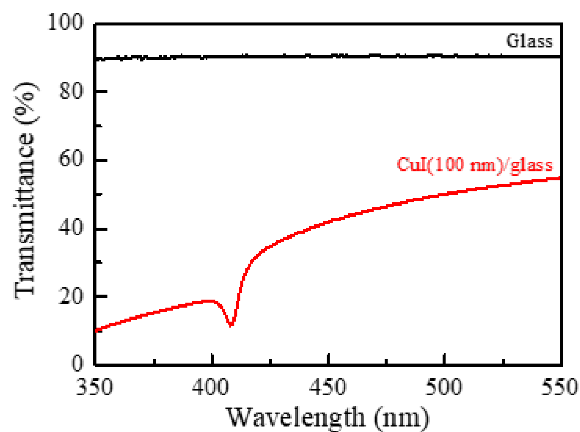

Figure 2.4 Transmittance as a function of wavelength of the bare glass substrate and the CuI(100 nm)/glass.

Low transparency has been confirmed once more by the transmittance spectrum after checking visually. To further figure out the semi-transparent behavior of the CuI film, surface topography images were obtained using AFM surface scans as shown in Figure 2.5. It is obviously observed that surface roughness is quite different after the iodization process. Along with the red dashed lines in the images, the surface profiles were obtained with root-mean-square (rms) surface roughness values. The obtained rms surface roughness is drastically increased after the iodization process from 2.4 nm for Cu film to 14 nm for CuI film.

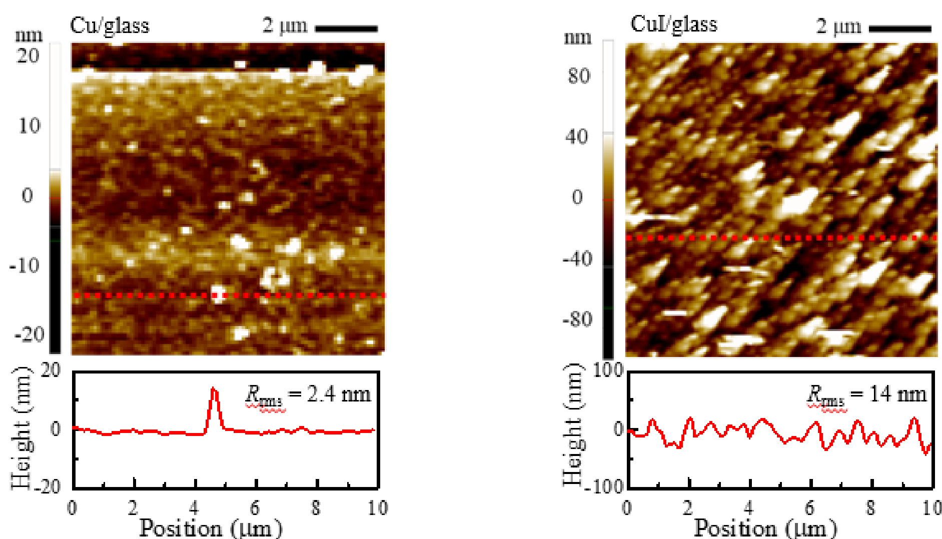

Figure 2.5 Surface topography images of Cu/glass and CuI/glass with root-mean-square surface roughness values and surface profile along the red dashed lines in each image.

The quite different rms roughnesses are attributed to the large volume expansion during the material transformation from Cu to CuI because the large increase of molar volume has occurred by about 5 times from 7.1 cm^3 mol^{-1} (Cu) to 33.2 cm^3 mol^{-1} (CuI). It is

a consistent result of the thickness variation from 17 nm for Cu film to 100 nm for CuI film. It is noted that the film crystallinity was checked by X-ray diffraction (XRD) for each film in Figure 2.6. Therefore, the large volume expansion induces a rough surface of polycrystalline CuI film after the iodization process resulting in the decrease of transmittance by the diffused reflection at the rough surface. Moreover, the brownish-yellow color infers often the existence of deep-level defect states, probably due to the structural fault during the phase transition.

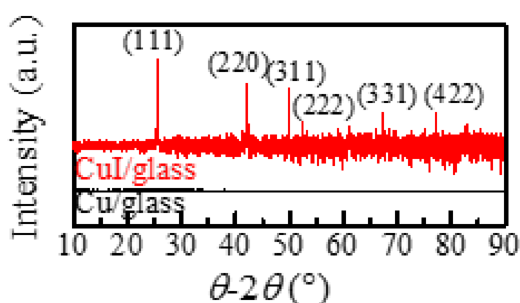

Figure 2.6 X-ray diffraction (XRD) patterns for metal Cu and polycrystalline CuI film on the glass substrate.

2.3 CuI film growth II : evaporated CuI film

High optical transparency is required to fabricate totally transparent *pn* junction diodes. To improve the rough surface of the CuI film, a new deposition method was adopted for growing CuI film. That is the thermal evaporation technique using the CuI power as source material to reduce the large volume expansion during the iodization process. Another merit of using the thermal evaporation method is the reduced process steps, meaning that only single-step deposition for thermal evaporation is needed. By using the thermal evaporation method, transparent CuI films on glass substrates were obtained as shown in Figure 2.7.

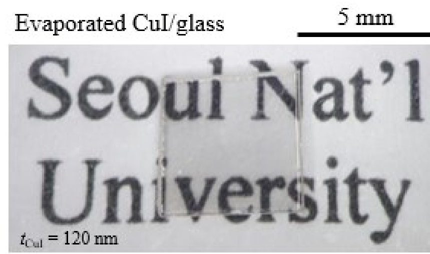

Figure 2.7 A photograph of evaporated CuI film on the glass substrate with a film thickness of 120 nm.

To systematically study and compare the transparency of the CuI film, the transmittance measurements were conducted using a UV-VIS-NIR spectrometer in Figure 2.8. The transmittance in the visible range of the evaporated CuI/glass sample is apparently improved since the film thicknesses are not that much different. An averaged transmittance value of the CuI(120 nm)/glass film between 450 nm and 750 nm is about 80 %, except for the sharp interband exciton absorption at 407 nm.

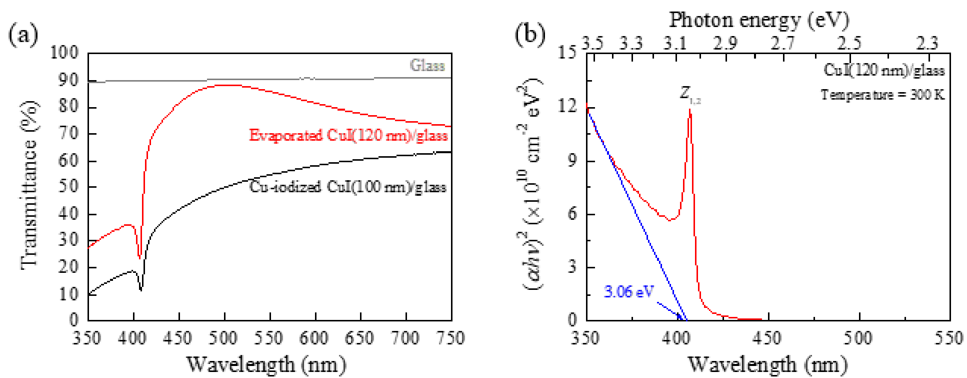

Figure 2.8 (a) Optical transmittance data on evaporated CuI(120 nm)/glass and Cu-iodized CuI(100 nm)/glass. (b) The absorption coefficient of the CuI film estimated using the Tauc plot.

The absorption coefficient of the CuI film can be estimated using the Tauc plot in Equation 2.2.

$$\alpha h\nu = A(h\nu - E_g)^n$$ **Equation 2.2**

where α is the absorption coefficient, $h\nu$ is the photon energy, A is the proportional constant, and E_g is the bandgap energy.

The exponent n expresses transition types for direct allowed transition (n = 1/2) or for indirect allowed transition (n = 2). It is noted that the CuI film is highly transparent in visible region resulting in the negligible reflectivity. The obtained absorption coefficient spectrum is in Figure 2.8(b). The estimated optical bandgap of the CuI film from the Tauc plot for a direct gap material is found to be 3.08 ± eV, which is commonly observed with E_g = 3.0 - 3.1 eV in many reports [29], [63]. Such a sharp excitonic absorption peak generally supports being of high film quality.

Figure 2.9 shows the surface topography of the CuI(120 nm)/glass grown by the thermal evaporator. A smooth surface was observed with a low rms roughness of 1.3 nm, which is comparable to or slightly better than the other reported data [29]. Moreover, such a low rms roughness value gives rise to a chance of making a clean interface of *pn* junction compared to the previous iodine reaction method. The typical rms roughness values of iodized CuI films are at least 20 - 30 nm in many formal CuI studies [29], [49].

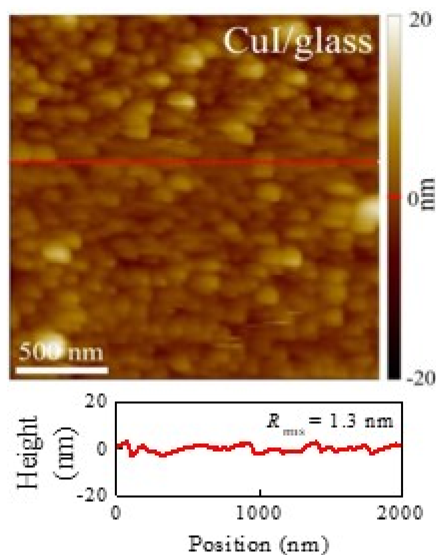

Figure 2.9 Surface morphology of the CuI(120 nm) film on the glass substrate grown by the thermal evaporation technique. The bottom panel exhibits a surface profile along the red dashed line in the figure.

To confirm the crystallinity of the evaporated CuI film with a 120 nm thickness, XRD θ- 2θ scanc were conducted in Figure 2.10. A high-resolution XRD (Empyrean, PANalytical) was used to examine the crystallinity. The most interesting thing is that the obtained CuI film shows a preferential alignment along the (111) plane, being consistent with the presented results [29], [34], [63]-[65]. It is noted that the bottom substrate is the glass, having an amorphous phase, which means that the preferential alignment of the CuI film is unlikely due to the epitaxial film. Besides, in the CuI system, it was indeed frequently observed that the (111) plane has the highest surface density of atoms as well as the lowest stability energy [66]. Therefore, the (111) preferential alignment of the CuI films turns out to be a stable state with a polycrystalline nature in the CuI systems [63].

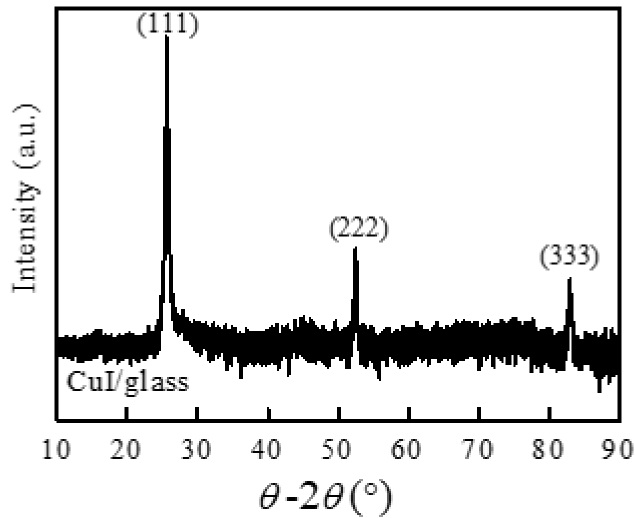

Figure 2.10 X-ray θ- 2θ scan results of CuI(120 nm)/glass, which exhibit the preferential alignment of the CuI film along the (111) plane.

To understand the electrical properties of the CuI films, the Hall effect measurements on the CuI/glass samples varying with the CuI film thickness were performed in the Van der Pauw configuration. Prior to carrying the measurements out, metallic Ni(5 nm)/Au(50 nm) electrodes were deposited by the use of stencil masks to form the ohmic contacts between the CuI films and the probe tips. In Figure 2.11, from the current-voltage (*IV*) curves, it has been confirmed that Ni/Au electrodes exhibited well-defined ohmic contacts with the CuI. Figure 2.12 shows the hole carrier density (p), resistivity (ρ), and hole mobility (μ_h)of the CuI films as a function of t_{CuI}. The Hall effect data of all the films basically turned out to have a positive sign, indicating that the CuI film is a indeed p-type semiconductor. All the *IV* measurements were performed at room temperature under ambient conditions without any light exposure.

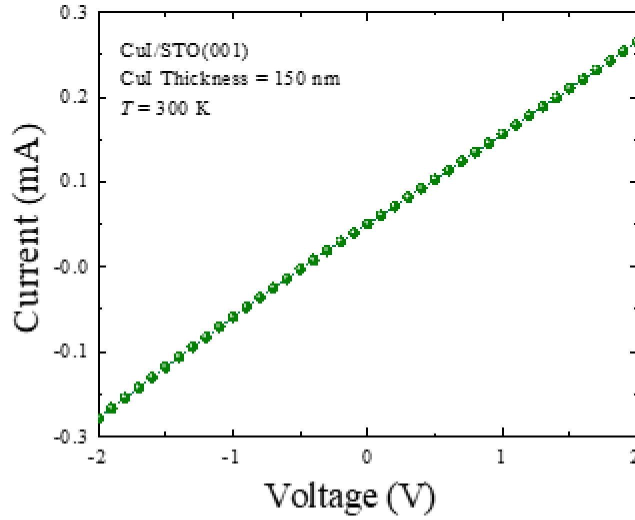

Figure 2.11 Current-voltage (*IV*) curve of the CuI film for confirming the linear behavior, indicating the ohmic contacts between the film and tungsten probe tips.

One interesting was found that the resultant p increases systematically as t_{CuI} is decreased. It has been figured out that a long-time deposition to grow a thick film by thermal evaporation processes can form the iodine vacancies (V_I). Because, in the CuI system, the V_{Cu} is known to be easily created as a native defect, which means a defect that is not intentionally created, but occurs naturally. The V_{Cu} acts as a dominant source of acceptor to induce the high p of typically ~10^{19} cm^{-3} [30]. In this situation, heat treatment has often caused the generation of V_I [34], [63], [67], followed by the decrease of the p as a result of V_{Cu} compensation. As the decrease of p, ρ increases with the increase of t_{CuI} due to the following equation:

$$\rho = 1/ep\mu_h \qquad \textbf{Equation 2.3}$$

where e is the elementary charge.

It was found that μ_h remained nearly constant or slightly decreases from 5 to 4.1 cm^2

V^{-1} s^{-1} with the increase of t_{CuI}. The μ_h variation might be proportional to t_{CuI} mainly due to ionized impurity scattering by V_{Cu} at the high p regime [29]. The obtained μ_h values are consistent with the typical reported values (2 - 4 cm^2 V^{-1} s^{-1}) of CuI films in literature at that p regime [29].

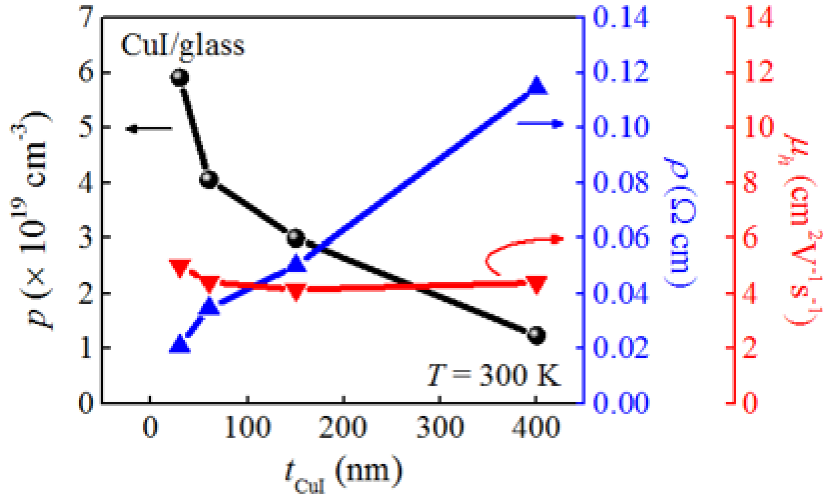

Figure 2.12 Hole carrier density (p), electrical resistivity (ρ), and hole mobility (μ_h) as a function of the thickness of the CuI films (t_{CuI}) grown on glass substrate by the thermal evaporation method.

2.4 Integration of *p*-CuI and *n*-BSO thin films for transparent heterojunction diodes

In this section, detailed experimental information is given to fabricate *p*-CuI/*n*-BSO heterojunction diodes. To synthesize the PLD target of polycrystalline $BaSnO_{3-\delta}$ (BSO) and $Ba_{0.96}La_{0.04}SnO_3$ (BLSO), a solid-state reaction method was used starting with high-purity $BaCO_3$, SnO_2, and La_2O_3 powders. All the compounds were weighed in a stoichiometric

ratio to make a pellet. The first calcination process was conducted at 1250 °C for 6 h and the final sintering process was carried out at 1450 °C for 24 h after several intermediate grindings. BSO and BLSO thin films were grown on STO substrate by the PLD method. A KrF excimer laser with a wavelength of 248 nm was used at a laser fluence of ~0.6 J cm^{-2} in oxygen partial pressure of 100 mTorr at 790 °C with a 10 Hz repeated rate. The obtained film was measured to measure the film thicknesses via AFM and the resultant thicknesses are 100 nm, 100 nm, and 0.5 mm for BSO, BLSO films, and STO substrate, respectively. Before the BSO film growth, the BLSO film was deposited as a structural buffered layer to reduce threading dislocations due to the large in-plane lattice misfit between BSO film (4.116 Å) and the STO substrate (3.905 Å). Here, the BLSO layer acts as an oxide electrode also because the BLSO film was not only a high electrical conductivity but also has good ohmic contact with the BSO film. Consequently, the BSO film was deposited under the same above PLD conditions with *in-situ* thermal annealing at 600 °C for 1 h under O_2 pressure of 600 mTorr to form oxygen vacancies in the film.

For CuI film growth, the high purity CuI powder (~99.998 %, 4N8) was evaporated at room temperature on the STO and BSO/BLSO/STO. To form *pn* heterojunctions with a small area, stencil masks that can make 5 - 15 junctions with a lateral size of 50 μm × 50 μm (square dot) or $\pi \times (50\ \mu m)^2$ (circular dot), respectively. The former was used for thin CuI films (t_{CuI} = 30 - 150 nm) and the latter was used for the 400-nm-thick CuI film. Besides, metallic Ti(5 nm) and Au(50 nm) electrodes were grown by the thermal evaporation to have ohmic contact between the BLSO film and the probe tips as shown in Figure 2.13. The lateral dimension of Ti/Au electrodes is about 0.2 mm × 2 mm. The tungsten probe tips were used to connect to electronics.

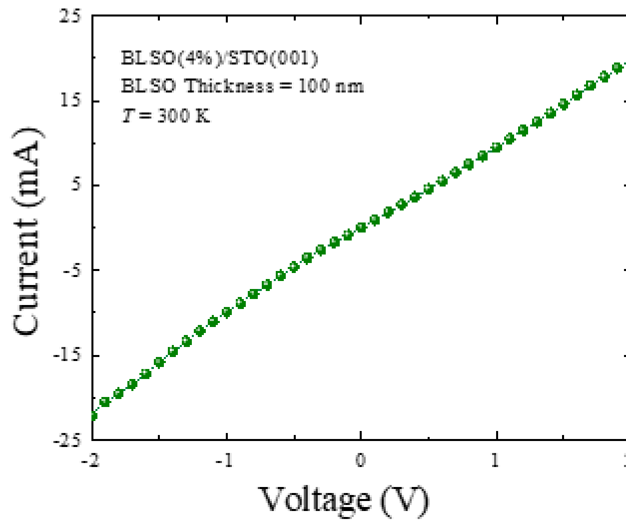

Figure 2.13 Current-voltage (*IV*) curve of the BLSO film to check the ohmic contact between the film and tungsten probe tips.

Figure 2.14 presents a schematic structure and an actual transparent photograph of the fabricated *p*-CuI/*n*-BSO heterojunction diode before the metallic film growths. As displayed in the figure, all the films are indeed transparent in visible light, demonstrating that the realized diode can be an optoelectronic component. It is noted that the film thicknesses of the CuI, the BSO, and the BLSO films are 120 nm, 100 nm, and 100 nm, respectively.

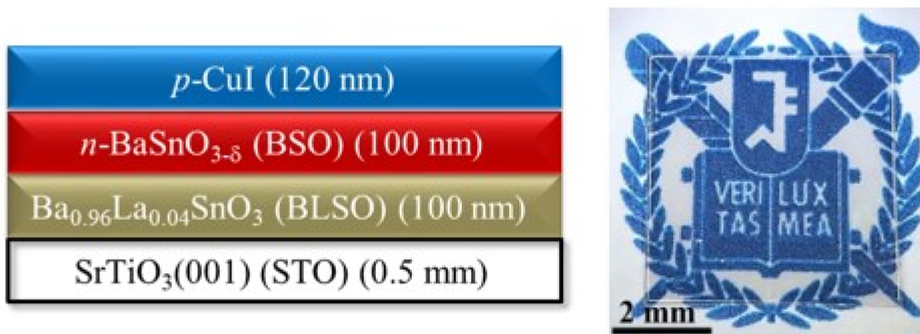

Figure 2.14 Schematic structure and actual photograph of the fabricated CuI/BSO/BLSO/STO sample without metallic electrode depositions.

To further understand the optical property of the realized CuI/BSO diode, optical transmittance spectra of the STO substrate, BSO/BLSO/STO, and CuI/BSO/BLSO/STO specimens were measured via UV-VIS-NIR spectrometer in the range of 350 - 750 nm in Figure 2.15. Both transmittance spectra of STO substrate and BSO/BLSO/STO exhibit high values of over 70 % in the visible regime. Though the exciton absorption and the Fabry-Perot interference pattern were observed, the CuI/BSO/BLSO/STO layers maintain high transparency of 70 %, which is consistent with the single film cases of BSO/BLSO or CuI. Once again, such a sharp exciton peak of the CuI film at 407 nm supports that the CuI film is of high quality on top of the BSO film. It is highly recommended in future optoelectronic devices that the high transparency of the diode.

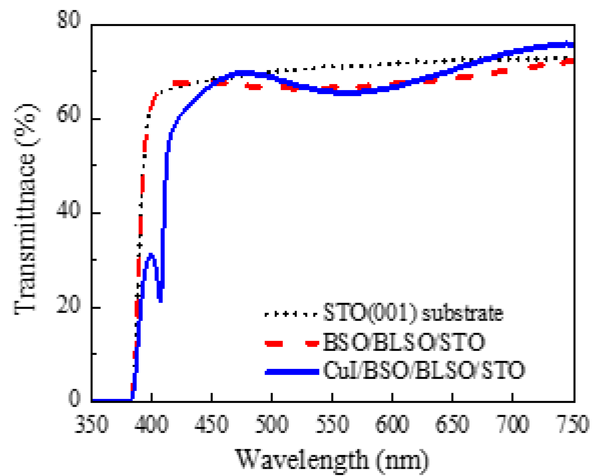

Figure 2.15 Optical transmittance spectra of STO substrate (black dotted line), BSO/BLSO/STO (red dashed line), and CuI/BSO/BLSO/STO (blue solid line). The Thickness of each layer is 0.5 mm, 100 nm, 100 nm, and 120 nm for STO substrate, BSO, BLSO, and CuI films, respectively.

Figure 2.16 shows XRD $\theta - 2\theta$ scan results of the CuI films on top of BSO/BLSO/STO, STO, and glass substrates. In all the cases, the CuI thickness is the same as the 120 nm. Regardless of the bottom layers, the CuI films exhibit a preferential alignment along the (111) plane as described in the previous section. It is remarkable that

the film crystallinity of the CuI film remains on the epitaxial (BSO/BLSO) layers as well as the amorphous (glass) phase.

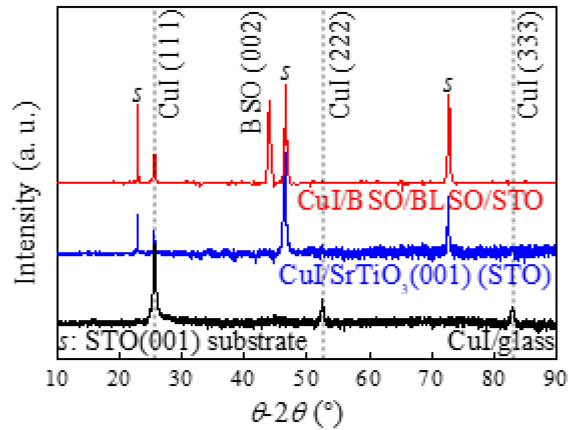

Figure 2.16 XRD θ - 2θ scan results of CuI/BSO/BLSO/STO, CuI/STO, and CuI/glass specimens, all of which show the preferential orientation of the CuI (111) plane regardless of bottom materials.

2.5 Current-voltage (*IV*) characteristics of the realized *p*-CuI/*n*-BSO diodes

Figure 2.17 exhibits current density-voltage (*jV*) curves of the *p*-CuI/*n*-BSO diode with variations of t_{CuI} from 30 nm to 400 nm. Both thin CuI films with 30-nm-thick and 60-nm-thick cases, show rather high forward current (I_F) at 2 V and reverse current (I_R) at -2 V, whereas for thick (t_{CuI} = 150 nm and 400 nm) CuI films I_R at off state (-2 V) are decreased. It is likely that the structural defects, such as grain boundaries and pinholes in the thin CuI films, can form additional current paths to result in the generation of the high leakage current. It is worth noting that the CuI film is not an epitaxial film, but a polycrystalline

film with the preferred orientation of the (111) plane, meaning that the random orientation of the in-plane crystal axes across the domains exists [64]. Such the leakage current due to the grain boundaries and pinholes increases the off-current I_R and it is generally reduced with an increase in film thickness. Therefore, reduced structural defect effects render the low I_R and high remained I_F at the high CuI film thickness.

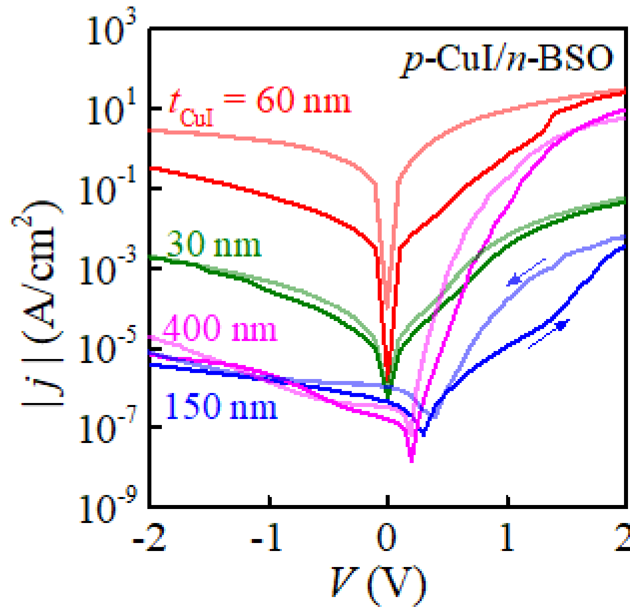

Figure 2.17 The current density-voltage (*jV*) curves of the *p*-CuI/*n*-BSO heterojunction diodes for various CuI film thicknesses (t_{CuI}).

In order to evaluate the diode performance, the most important parameter is the current rectification ratio (I_F/I_R), which refers to the ratio of the on-current (I_F) to the off-current (I_R). Figure 2.18 display the change in the current rectification ratio with the t_{CuI} variations. What is compelling in the diode behavior is the systematic increase of the current rectification ratio proportional to t_{CuI}. As explained just before, the off-current can be understood by the leakage current presumably due to the grain boundaries and pinholes. While, when the on-currents for t_{CuI} = 150 nm and 400 nm are compared, the I_F of the 400-nm-thick CuI film shows much higher than that of. This phenomenon can be comprehended

by the built-in potential (V_{bi}), which is commonly expressed in a *pn* diode in Equation 2.4.

$$V_{bi} = \frac{k_B T}{e} \ln\left(\frac{N_a N_d}{n_i^2}\right) \quad \textbf{Equation 2.4}$$

where V_{bi} is the built-in potential of a *pn* diode, k_B is the Boltzmann constant, T is the absolute temperature, e is the elementary charge, N_a is the acceptor concentration, N_d is the donor concentration, and n_i is the intrinsic density.

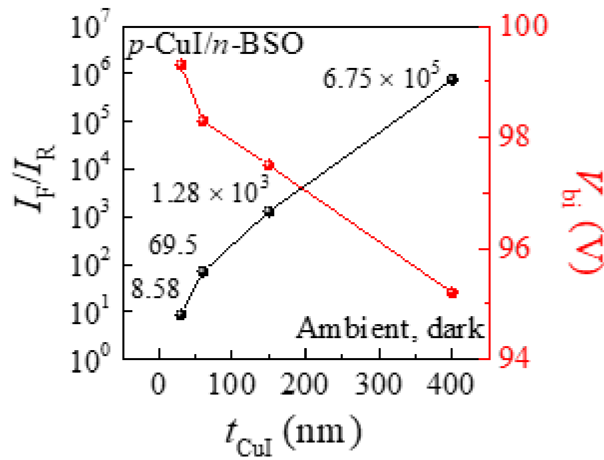

Figure 2.18 The current rectification ratio (I_F/I_R) and built-in potential (V_{bi}) in the *p*-CuI/*n*-BSO diodes at various t_{CuI}.

Upon changing the t_{CuI}, the varied parameter in Equation 2.4 is just N_a due to the modification of p ($N_a \sim p$). In other words, the V_{bi} is proportional to the p and an increase of p leads to the enhanced V_{bi} at the *pn* junction interface. Such behavior tends to reduce the injection of carriers at the interface resulting in the decrease of I_F/I_R. It is thus likely that the higher I_F/I_R in thicker CuI films should be originated from the increase of I_F due to the reduced V_{bi} by the decrease of p.

To further investigate the electrical property of the *p*-CuI/*n*-BSO diode, the current-

voltage (*IV*) and the current-density voltage (*jV*) curves are compared in Figure 2.19.

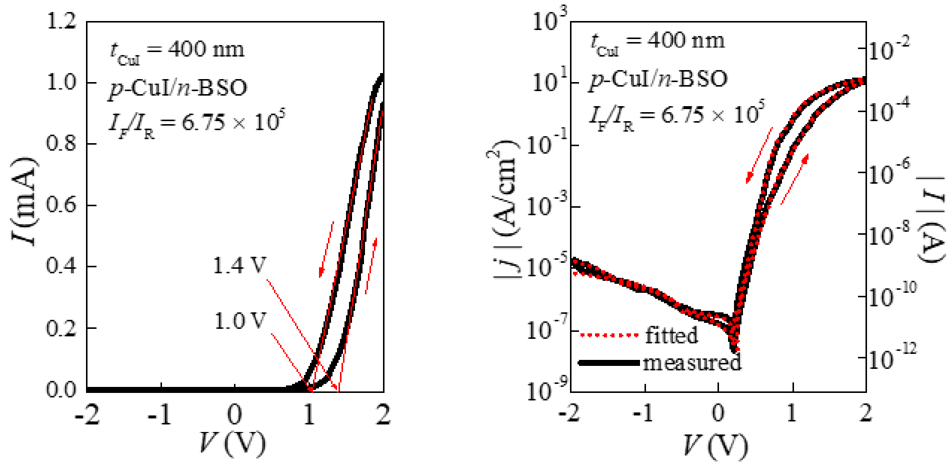

Figure 2.19 the current-voltage (*IV*) and the current-density voltage (*jV*) curves of the *p*-CuI(400 nm)/*n*-BSO(100 nm) diode. Red solid lines in the *IV* curve represent linear extrapolation to determine the turn-on voltage. The red dotted lines in the *jV* curve display the fitting curves based on the diode equation (Equation 2.6).

In the *IV* curve, the clear current rectifying behavior was observed, referring to the well-operated *pn* junction diode. Here, the turn-on voltage, which is an onset of the drastic increase of the current, is estimated from a linear extrapolation as presented as red solid lines in Figure 2.19. The turn-on voltages are turned out as 1.0 V and 1.4 V for the reverse and the forward directions, respectively. In general, such a difference between forward and reverse current is represented as the hysteresis, demonstrating the presence of charged trap states in the diode. Furthermore, in an ideal diode, the turn-on voltage should be directly associated with the band offset. The threshold voltage of the electron ($V_{\text{th-n}}$) and of the hole ($V_{\text{th-p}}$) can be determined from Equation 2.5.

$$V_{th-n} = V_{bi} + \left|\frac{\Delta E_C}{q}\right|,\; V_{th-p} = V_{bi} + \left|\frac{\Delta E_V}{q}\right| \qquad \textbf{Equation 2.5}$$

where ΔE_C and ΔE_V are the conduction and valance band offset, respectively.

The V_{th-n} and V_{th-p} imply the injection of electrons from *n*-side to *p*-side and the transportation of holes from *p*-side to *n*-side, respectively. The corresponding V_{th-n} and V_{th-p} are calculated as 2.85 V and 2.77 V, which are apparently smaller than the measured turn-on voltage of 1.0 V and 1.4 V, respectively. Such behavior can be observed when there exists the in-gap state in the bandgap, being able to form the additional current path at low voltage [29]. Based on the experimental results, an almost similar applied voltage of $V \sim V_{bi}$ seems enough to make the electron (hole) flow. Therefore, unintended impurity states, probably due to iodine vacancy or excess oxygen vacancy inside the bandgap, are attributed to electrical transport to be injected in an applied bias at low voltage [49].

To quantitatively study the diode performance, the diode curve fitting has been performed using the Shockley diode equation as follows Equation 2.6:

$$j(V) = js\{\exp[\frac{e(V - IR_s)}{\eta k_B T}] - 1\} + \frac{V - IR_s}{R_p} \qquad \textbf{Equation 2.6}$$

where j_s is the reverse saturation current density, η is the ideality factor k_B is the Boltzmann constant, T is the absolute temperature, R_S is the series resistance, and R_P is the parallel resistance [29].

The *jV* curve was fitted by the implicit equation for a heterojunction diode as shown in Figure 2.19. The curve fitting results are indeed well-matched with the measured *IV* curve and the corresponding diode parameters are summarized in Table 2.2. The obtained fitting was performed assuming the multi-contacts theory in the *pn* junction [64].

	Barrier 1 (>0.8 V)			Barrier 2 (<0.8 V)			
Sweeping direction	η	j_S (A cm^{-2})	R_S (Ω)	η	j_S (A cm^{-2})	R_S (Ω)	R_P (Ω)
Forward	2.53	1.44×10^{-9}	456	1.45	1.26×10^{-8}	16976	1.55×10^{9}
Reverse	2.11	6.54×10^{-9}	762	1.59	1.16×10^{-9}	12780	2.49×10^{9}

Table 2.2 Numerical fitting parameters obtained by diode curve fitting for the *IV*

curve of the *p*-CuI/*n*-BSO heterojunction diode.

From the fitting results, the resultant ideality factor for the *p*-CuI(400 nm)/*n*-BSO diode is about 1.5, which indicates that the diode governs diffusion (η = 1) and recombination (η = 2), simultaneously.

On the basis of experimental observations, we proposed an energy band diagram of the *p*-CuI/*n*-BSO heterojunction diode in Figure 2.20, especially for the best-performing case of t_{CuI} = 400 nm. In order to establish the band diagram, the Anderson heterojunction diode model was used with various input parameters as summarized in Table 2.3.

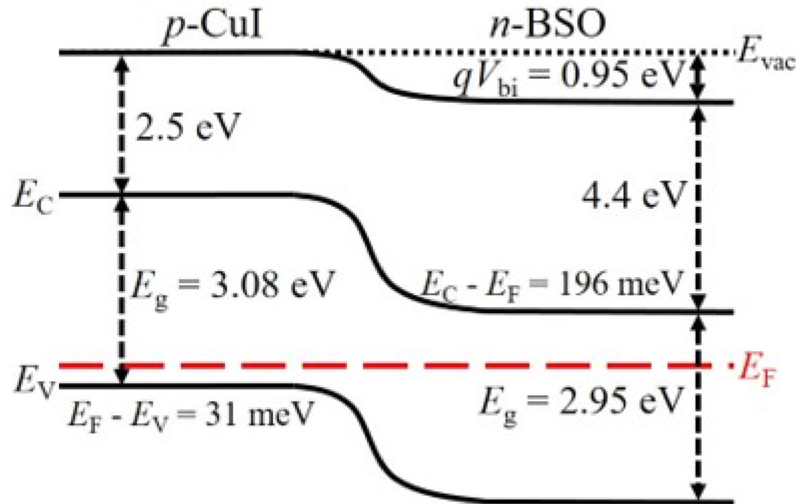

Figure 2.20 A proposed energy band diagram of the *p*-CuI(400 nm)/*n*-BSO heterojunction diode, exhibiting the best performance.

Film	Band gap (eV)	Electron affinity (eV)	Carrier density (cm^{-3})	Dielectric constant	Effective mass (m_0 : electron mass)
p-CuI	3.08	2.5 [29]	1.2×10^{19}	15.1 [68]	$1.4m_0$ [29]
n-$BaSnO_{3-\delta}$	2.95 [22]	4.4 [12]	2.6×10^{15} [12]	20 [69]	$0.35m_0$ [70]

Table 2.3 Input parameters of the Anderson diode model for the *p*-CuI/*n*-BSO heterojunction, where m_o is the electron mass.

From the calculation of the Anderson diode model for the built-in potential (V_{bi}), depletion width for *p*-type layer (x_p), and depletion width for *n*-type layer (x_n), those values were evaluated to be V_{bi} = 0.95 V, x_p = 0.03 nm, and x_n = 121 nm, respectively. The predicted space charge region is located mainly at the *n*-type region, which is called as one-side abrupt junction. The band formation demonstrates that the *p*-CuI/*n*-BSO heterojunction diode is the type-II band alignment, in which a conduction band offset of *n*-type material is located between the offsets of conduction and valance bands of *p*-type material. This type of band alignment is preferred in optoelectronic devices because carrier separation is enhanced. In these conditions, electrons (holes) can only flow to the *n*-(*p*-)type electrode and have been blocked to the *p*-(*n*-)type electrode by the V_{bi}. Figure 2.21 illustrates the current flow of free carriers. Furthermore, the established band diagram can systematically describe the variation of the current rectification ratio by the decrease of *p*.

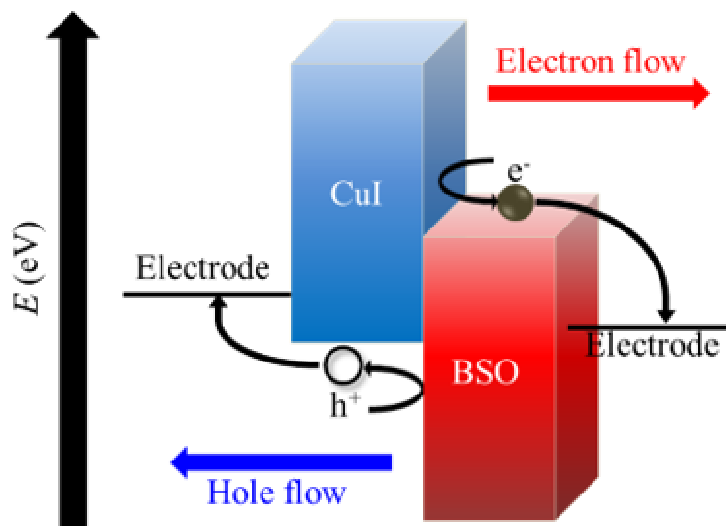

Figure 2.21 The cartoon figure of the electronic structure of *p*-CuI/*n*-BSO heterojunction with the demonstration of free carriers.

It is further noted that x_n of 121 nm is indeed larger than the *n*-type film thickness itself (t_{BSO} = 100 nm). In such a case, there exists an effective bias voltage because a finite

forward voltage can be required to erase the built-in potential effect, which is consistent with the experimental observation in the *IV* curve. It is thus likely that the finite voltage value in the turning point of 0.2 V (0.4 V) in the j*V* curves originated from the junction thickness being thinner than the space charge region.

2.6 A high current rectification ratio of the *p*-CuI/*n*-BSO diode among BSO-based heterojunctions

It will be worthwhile to compare the current rectification ratio of the *p*-CuI(400 nm)/*n*-BSO heterojunction diode to the other BSO-based heterojunction diodes, which have at least one wide bandgap material. The I_F/I_R values are summarized in Figure 2.22.

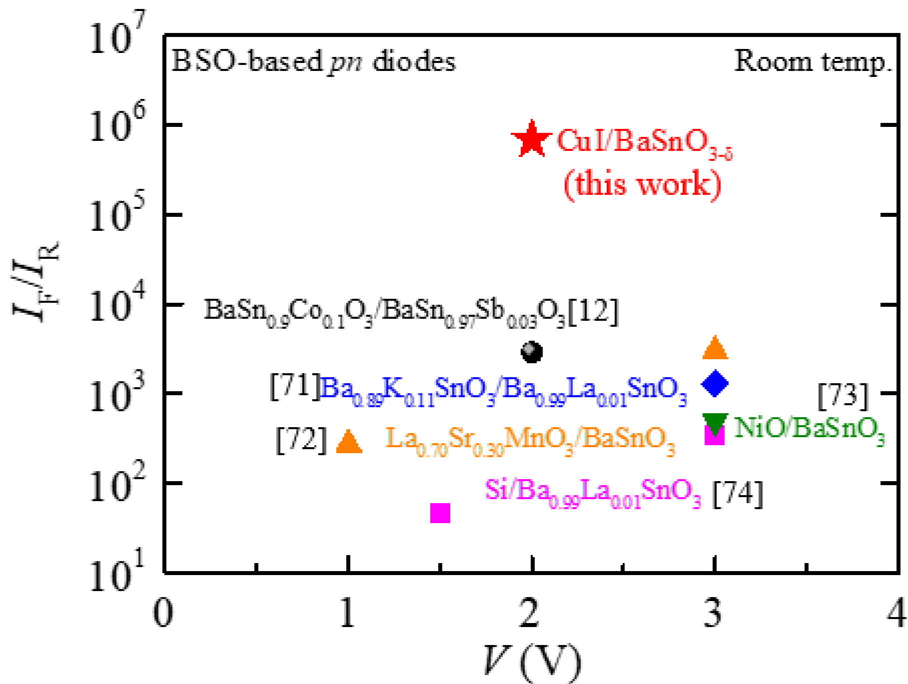

Figure 2.22 Comparison of the current rectification ratios (I_F/I_R) for various BSO-

based *pn* heterojunction diodes.

Various different types of *pn* heterojunctions have been tested to realize the high-performance *pn* diode, particularly for the current rectification ratio [12], [71], [74]. The I_F/I_R of the *p*-CuI/*n*-BSO is fairly high among various BSO-based *pn* diodes. Therefore, the clean junction made of *p*-CuI and *n*-BSO can give rise to opportunity as a transparent active component of next-generation optoelectronic devices.

2.7 Summary

In this chapter, we have tested two methods to grow CuI thin films for having a smooth surface to form a clean interface with the *n*-type materials of $BaSnO_3$ and La-doped $BaSnO_3$. The fundamental physical properties of CuI films on glass substrate grown by the thermal evaporation technique were investigated. Based on the improved structural properties of the evaporated CuI film, totally transparent *p*-CuI/*n*-$BaSnO_{3-\delta}$ heterojunction diodes have been successfully realized. We have studied the electrical characteristics of CuI/$BaSnO_{3-\delta}$ diodes, grown by thermal evaporation for the polycrystalline CuI film and by pulsed laser deposition for the epitaxial $BaSnO_{3-\delta}$(001) film. As the CuI film thickness increases in the formed diode, it turns out to be a decrease in hole carrier density and an increase to the current rectification ratio systematically. The current rectification ratio, which is the most critical parameter of the device, can be physically explained by the reduced built-in potential by the decrease of hole carrier density. Furthermore, we proposed the *p*-CuI/*n*-$BaSnO_{3-\delta}$ heterojunction diode, being have the type-II band alignment. For the best-performing diode, the high current rectification ratio of 6.75×10^5 and an ideality factor of about 1.5. Therefore, on the basis of all the experimental and calculation results,

the realized *p*-CuI/*n*-$BaSnO_{3-\delta}$ diode can be a promising alternative transparent component in next-generation optoelectronic devices.

Chapter 3 Characteristics of a transparent *p*-CuI/*n*-SiZnSnO heterojunction diode

3.1 Overview

In the previous chapter, we addressed for mainly *p*-CuI/*n*-$BaSnO_{3-\delta}$ heterojunction diodes and their structural, optical, and electrical properties to investigate the diode transport mechanism. The present diode exhibited a high current rectification ratio of 6.75×10^5 at ±2 V. In order to reach the high current rectification ratio of BSO-based *pn* diodes, it is required a high-quality BSO film with an epitaxial growth mode on a lattice-matched substrate such as STO, and a rather high growth temperature of above 800 °C. Such a constraint should be overcome for practical applications, such as low-cost and flexible devices. Thus, it will be worthwhile to test a heterojunction diode made of an alternative *n*-type film that can be grown at a relatively low-temperature growth condition comparable to that of the CuI film. For this motivation, we tried to find a new *n*-type material system for practical applications and adopted a novel *n*-type amorphous semiconductor SiZnSnO (SZTO) film, which shows a high optical bandgap of 3.7 eV with field-effect mobility of about 38 $cm^2\ V^{-1}\ s^{-1}$ [75]. Furthermore, the electrical performance of the *n*-type SZTO film under ambient conditions is much more stable than that of the most well-known amorphous *n*-type InGaZnO (IGZO) film [76], presumably due to reduced oxygen vacancies by strong Si-O binding energy of 799 kJ mol^{-1} than the Ga-O of 374 kJ mol^{-1} [77]. Furthermore, an amorphous phase gives rise to a change to reduce many kinds of structural defects, such as grain boundary, threading dislocation, pinhole, etc., to result in the enhancement of device performance. Once such defects have been reduced, the leakage current, which is a main demeaning factor for transport behavior, can be further decreased, leading to the lowering of power consumption in applications. In addition to the better oxygen controllability, the

n-type SZTO film is composed of non-toxic and abundant elements of Si and Sn, which can be reduced the prices of final products. Therefore, the SZTO system is desirable as a transparent passive layer to fabricate practical devices combined with the CuI system. In this chapter, a new *n*-type amorphous semiconductor SZTO has been introduced and the physical properties of the CuI film were studied before and after thermal annealing. In order to fabricate the *pn* junction, the realization of the *p*-CuI/*n*-SZTO heterojunction diode was investigated systematically. The diode mechanism has been quantitatively analyzed based on the diode curve fitting simulation. To establish the electronic structure of the realized diode, the energy band diagram was proposed. The high current rectification ratio of the *p*-CuI/*n*-SZTO diode is compared to the other CuI-based *pn* heterojunction diodes.

3.2 Introduction of a novel *n*-type amorphous semiconductor : SiZnSnO

It will be worthwhile to introduce the materials of SiZnSnO (SZTO) first. The SZTO is a novel *n*-type amorphous stannate semiconductor, constituting Si as an oxygen suppressor (carrier density controller), Zn as a network former (amorphous structure stabilizer), and Sn as a mobility enhancer (electron path former). According to the most famous amorphous semiconductor IGZO, the isotropic s orbital produces electron paths regardless of crystalline domains [78]. Such a feature can make the amorphous semiconductor, being comparable electron mobility to the crystalline semiconductor. Furthermore, amorphous materials typically have no structural defects, such as grain boundary or threading dislocation, so the electron scattering at grain boundary can be reduced. In addition, the smooth surface of an amorphous material can provide a uniform interface during the multi-layer integration. Moreover, the growth temperature of an

amorphous film is usually lower than the crystalline one, indicating a low-cost process as well as a large degree of freedom of the substrate selection. It is thus highly likely that amorphous semiconductors can be useful to fabricate specific flexible, cost-effective optoelectronic devices.

In this sense, it will be worthwhile to realize the *pn* heterojunction using the *n*-type amorphous semiconductor SZTO because it shows a high optical bandgap, comparable field-effect mobility, and superior electrical stability with low-price nontoxic and abundant elements as described in the previous section. Furthermore, the electronic energy band alignment of the *n*-type amorphous ZnSnO can be tuned by the Si amount due to the high binding energy of Si-O [77]. Such a capability can give arise to organize the *pn* junction band diagram, leading to the improvement of the device efficiency. As the Si content increases, band renormalization has been occurred, being an increase in the bandgap energy and work function of the SZTO film [76]. Upon various with not only the Si content but also oxygen partial pressure during the SZTO deposition by RF magnetron sputtering, the electronic band structure has been influenced as reported in the previous literature [75]. The SZTO films on ITO deposited boro-aluminosilicate glass substrate (EAGLE XG slim glass, Corning) were grown by RF magnetron sputtering (KVS-2004, Korea Vacuum Tech) at a power of 60 W in a mixed gas of Ar and O_2 at room temperature (Ar:O_2 = 40:1 sccm). The ITO film was prepared at 30 W in Ar partial pressure of 4 mTorr at room temperature using DC magnetron sputtering (KVS-2002, Korea Vacuum Tech). The as-deposited SZTO/ITO films were annealed at 500 °C for 2 hrs at ambient conditions to make a stable phase with better electrical conductivity. An amorphous feature of the SZTO film was confirmed by transmission electron microscope (TEM) and the electronic band structure has been proposed with the Si variation in an earlier report [76]. In order to establish the electronic band structure of the SZTO films, various measurements, such as TEM, high-resolution electron energy loss spectroscopy (HE-EELS), ultraviolet photoelectron spectroscopy

(UPS), Kelvin probe force microscopy (KPFM), and X-ray photoelectron spectroscopy (XPS) were conducted by Sang Yeol Lee's group at Gachon University as part of a co-work.

3.3 Annealing effects on the evaporated CuI films

Prior to the integration of *p*-CuI and *n*-SZTO films, the as-grown CuI films were annealed at 50 °C for 125 hrs under N_2 gas flowing condition of 20 mL/min to reduce grain boundary and *p*. The *p* of the CuI system is known to be controlled by the mild temperature heat treatment as following equations [34];

$$CuI \rightarrow Cu_{1-x}I + x(V_{Cu} + h)$$

Equation 3.1

The CuI generally creates the native defect of V_{Cu}, providing hole carriers to the system.

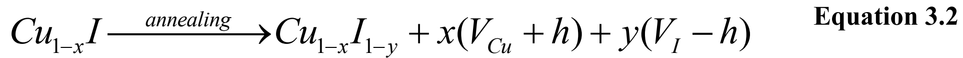

$$Cu_{1-x}I \xrightarrow{annealing} Cu_{1-x}I_{1-y} + x(V_{Cu} + h) + y(V_I - h)$$

Equation 3.2

The N_2 thermal annealing induces iodine evaporation, producing iodine vacancy (V_I).

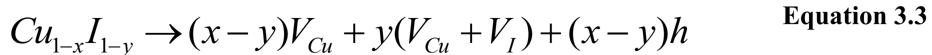

$$Cu_{1-x}I_{1-y} \rightarrow (x-y)V_{Cu} + y(V_{Cu} + V_I) + (x-y)h$$

Equation 3.3

The formed V_I compensates V_{Cu} to result in the decrease of *p*. Furthermore, the thermal annealing can give rise to providing additional kinetic energy to the system to be able to induce the migration of existing V_{Cu} from the inside of the CuI film to the outside of the surface or grain boundary.

$$\therefore CuI \xrightarrow{annealing} V_{Cu}^{*} + (x-y)h$$ **Equation 3.4**

Therefore, the N_2 thermal annealing can reduce not only V_{Cu}, but also p in the CuI films. In order to confirm the alteration of electrical properties, we have measured the Hall effect on the CuI films on glass substrates before and after the N_2 thermal annealing in Figure 3.1.

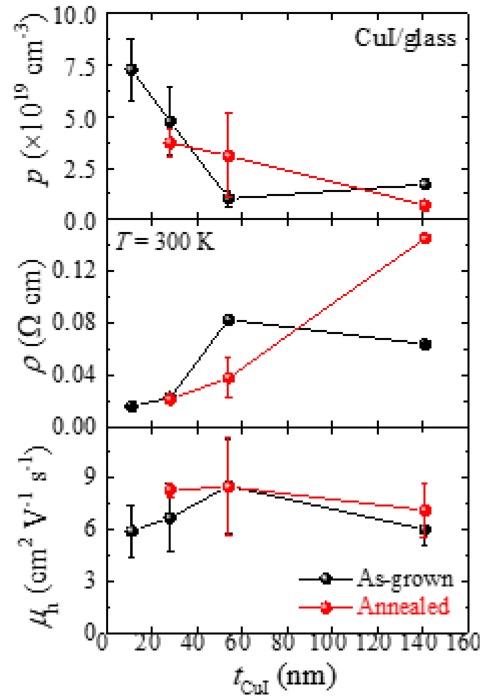

Figure 3.1 Room temperature hole carrier density p, electrical resistivity ρ, and hole mobility μ_h as a function of the CuI film thickness t_{CuI}. The black and red symbols represent the data of the as-grown and annealed CuI films on glass substrates, respectively. In the case of annealed CuI(11 nm)/glass, Hall resistivity could not be measured due to the high resistance.

As expected in Equations 3.1 - 3.4, the thermal annealing leads to the decrease of charged trap sites of V_{Cu}, the decrease of grain boundaries by the out-diffusion of V_{Cu}, and the decrease of ionized impurity scattering by the reduced p. According to the reduced

structural defects, the resultant CuI films exhibit better film quality, which is examined by XRD omega scan rocking curves in Figure 3.2. It is noted that the CuI films display the preferential orientation of the CuI (111) plane, which is consistent with our previous observations. The full-width at half-maximum (FWHM) values of the films have been reduced by the annealing, except for the thinnest 11-nm-thick CuI film. The sample degradation is commonly observed after the excess thermal annealing, presumably due to the weak resistance of the CuI system for the heat treatment [79]. If the CuI is subject to excessive thermal annealing, out-diffusion of V_{Cu} and the excessive formation of V_{I} is occurred to result in the degradation in the sample qualities. In that case, the specimen becomes porous, brownish-yellow, and eventually forms many cracks [80].

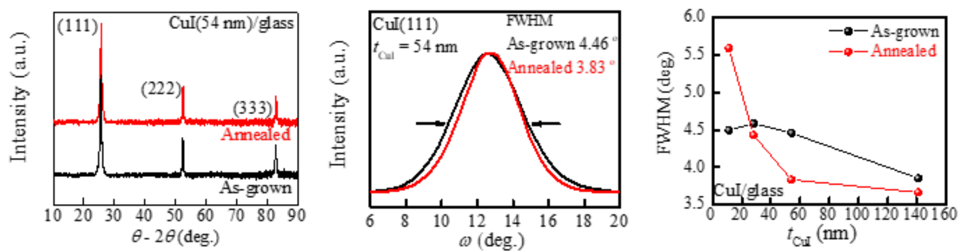

Figure 3.2 X-ray θ - 2θ and ω scan results of representative CuI(54 nm)/glass and FWHM values as a function of t_{CuI} before and after the thermal annealing.

To further understand annealing effects on the structural property of the CuI film, surface topography images were measured by AFM in a contact mode for the as-grown and the annealed CuI(140 nm)/glass cases. By performing the annealing, reduced grain boundaries can be verified in the AFM images in Figure 3.3. In the AFM image of the as-grown CuI (left), grains are represented by the red-colored region while the grain boundaries are shown as white-colored lines. The averaged grain size is estimated as about 48 nm in the as-grown film, whereas it is slightly increased to about 52 nm in the annealed film. In addition to that, rms surface roughness in the entire area of 2 μm × 2 μm decreases from 5.46 nm to 4.03 nm. After the thermal annealing, most of the grains are merged with

the nearest neighboring grains so that the white borderline indicating the grain boundary becomes ambiguous, implying the reduction of grain boundaries. It is thus likely that thermal annealing can effectively reduce the grain boundaries based on the experimental observation of the R_{rms} decrease and the connected grains in the AFM image. It should be noted that the lateral and height resolution of the AFM measurements are almost equal because the exact same conditions were used sequentially.

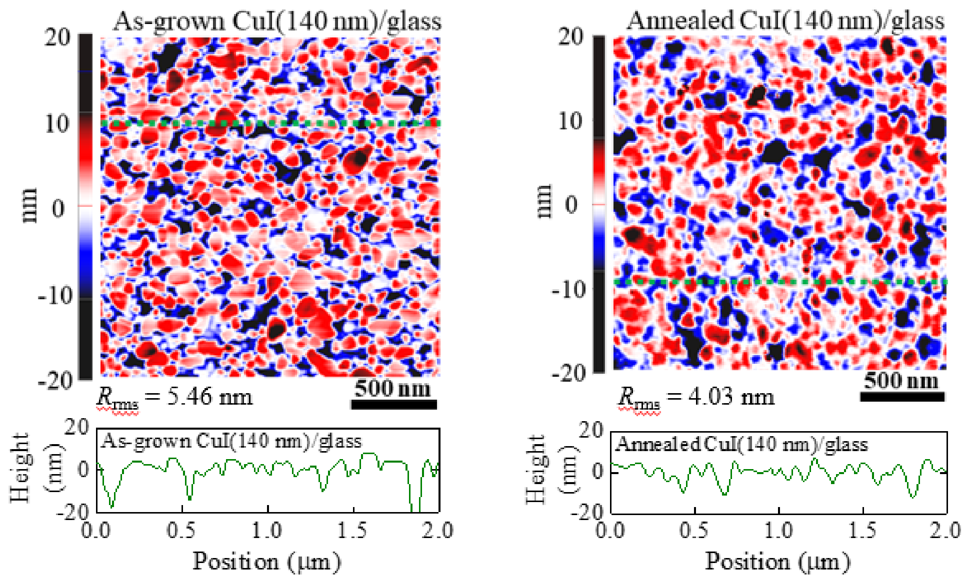

Figure 3.3 Surface morphology of as-grown and annealed CuI(140 nm)/glass measured by AFM in a contact mode. The bottom panels display surface line profiles along the green dotted lines presented in the images. A root-mean-square (rms) surface roughness in the whole area of 2 μm × 2 μm decreases from 5.46 nm to 4.03 nm after the thermal annealing.

Therefore, from the experimental evidence, thermal annealing with the optimum conditions can make the reduction of ionized impurity scattering by compensating V_{Cu} and also by reducing V_{Cu} from inside the CuI film. At the same time, the reduced grain boundaries of the CuI film turn out to form a smooth and uniform interface to effectively improve the diode performance.

3.4 Realization of transparent *p*-CuI/*n*-SZTO diodes

To grow ITO (t = 50 nm) and SZTO (t = 27 nm) films on boro-aluminosilicate glass substrates (t = 0.5 mm), the DC and RF magnetron sputtering were used with the ITO and SZTO ceramic disk as target materials. After photolithography patterning process, the SZTO film was grown as described in an earlier section. The as-grown SZTO/ITO film was annealed at 500 °C for 2 hrs under ambient conditions. For the CuI film growth, a custom-made thermal evaporator was used with the CuI powder (purity of 99.998 %, 4N8) at room temperature on a glass substrate (soda-lime for a microscope slide, Marienfeld) and SZTO/ITO/glass, respectively. For the realization of CuI/SZTO heterojunctions, both CuI and Au/Ni films have been sequentially deposited using the same metal stencil masks that can produce 10 circular cots with a typical radius of 50 μm. The Ni film (t = 5 nm) was first grown on the CuI film, followed by the deposition of Au film (t = 50 nm). Figure 3.4 exhibits that the Au/Ni metallic films on top of the CuI film shows linear *IV* curves. On the other hands, the Au/Ni films act as a metallic electrode and form an Ohmic contact between the CuI film and a tungsten probe tip. Here, additional SiO_2/Si specimen was used to check the Ohmic contact in the *IV* curve.

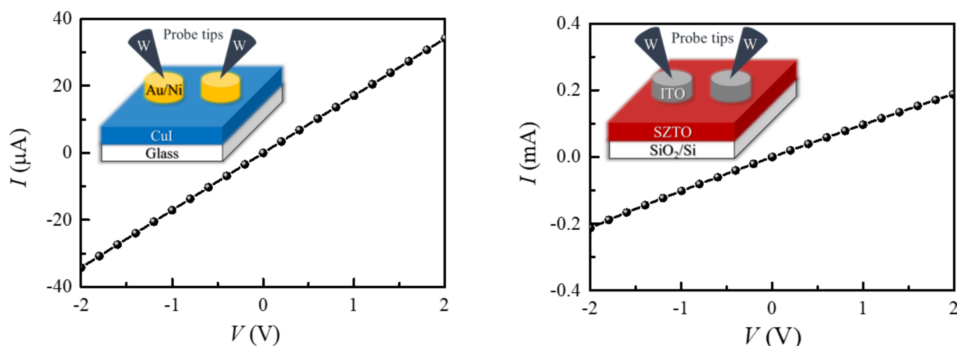

Figure 3.4 Current-voltage (*IV*) characteristics of Au/Ni/CuI and ITO/SZTO/SiO_2/Si,

respectively. The *IV* curves were measured at room temperature without any light exposure. Schematic drawings are presented the measurement configuration of the two-probe contact method.

To further improve the diode property, thermal annealing at 50 °C for 125 hrs under the N_2 gas flowing conditions of 20 mL/min was performned. The *IV* characteristics were measured under dark and air conditions at room temperature using the semiconductor characterization system (4200-SCS, Keithley).

Figure 3.5 shows a schematic structure of the realized CuI/SZTO diode for optical experiments and an specimen, revealing that all the films are indeed transparent under visible light conditions. A lateral size of the CuI/SZTO films (orange dashed line) and ITO/glass substrate (green dashed line) are 10 mm × 4 mm and 10 mm × 10 mm, respectively. It is noted that the film thicknesses of the CuI, SZTO, and ITO are 110, 27, and 50 nm, respectively.

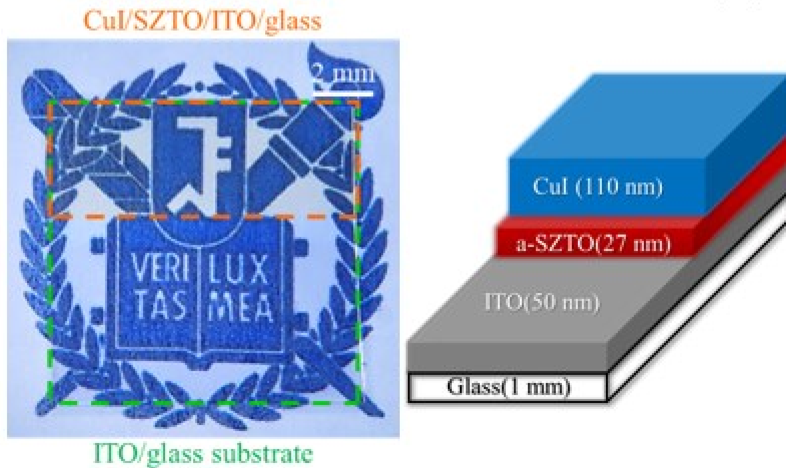

Figure 3.5 An actual photograph and a schematic structure of the *p*-CuI/*n*-SZTO diode grown on the ITO deposited glass substrate for optical characterization. The CuI(110 nm)/SZTO(27 nm) (orange dashed line) were deposited on top of the ITO/glass substrate (green dashed line), exhibiting optical transparency.

To further study the optical properties of the CuI/SZTO diode quantitatively,

transmittance (T_λ) and reflectance (R) spectra of the CuI/SZTO/ITO/glass sample were measured the UV-VIS-NIR spectrophotometer (Cary 5E, Varian). Figure 3.6 displays the T_λ, R, and absorption (A) spectra as a function of wavelength λ. It is noted that the transmittance has been represented as T_λ in this section to avoid confusion with the absolute temperature T. A bare glass substrate was tested as a standard specimen, showing a nearly constant T_λ of about 90 %.

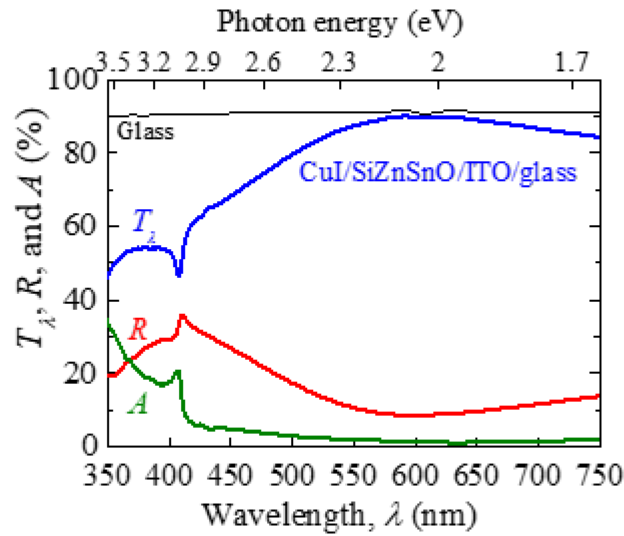

Figure 3.6 Optical transmittance (T_λ), reflectance (R), and absorbance (A) spectra of the CuI(110 nm)/SZTO/ITO/glass. The black solid line represents the T_λ of a bare glass substrate (t = 1 mm).

The absorbance spectrum is not measured data, but calculated spectra from Equation 3.5.

$$A = 100 - T_\lambda - R \quad \textbf{Equation 3.5}$$

The maximum T_λ of the CuI/SZTO/ITO/glass is always higher than 80 % in the visible spectral range of 500 to 750 nm and is basically found to be as high as about 90 %, which is

consistent results with the photograph. According to Equation 3.6, the transmittance of the remaining films except for the glass substrate is likely to be higher than about 88 % in the visible range.

$$T_{\lambda,\mathrm{film}} = T_{\lambda,\mathrm{measured}} / T_{\lambda,\mathrm{glass}}$$ **Equation 3.6**

All the optical spectra demonstrate the high transparency of the diode structure (CuI/SZTO/ITO/glass) in Figure 3.5.

Furthermore, it is worth noting that the peak at 407 nm (3.05 eV) originates from the excitonic absorption, which is frequently observed in CuI films [29], [63], [81]. From the excitonic transition peak and the exciton binding energy of the CuI, the bandgap energy E_g of the CuI film can be estimated as about 3.1 eV following Equation 3.7.

$$E_g = E_{Z_{1,2}} + E_{ex}$$ **Equation 3.7**

where $E_{Z1,2}$ is an excitonic absorption energy of CuI and E_{ex} is an exciton binding energy of 62 meV [82].

The estimated E_g is indeed consistent with our previous value (~3.08 eV in chapter 2) and other reports [29], [63], [80]. On the basis of the experimental evidence for the similar E_g of the CuI film, the other samples with the different tCuI are likely to be expected as transparent also, as confirmed in the previous chapter. Moreover, such a sharp excitonic absorption peak at 407 nm strongly assists that the film quality of the as-grown CuI film is good enough.

The film crystallinity of the fabricated CuI/SZTO/ITO/glass diode was confirmed by XRD θ - 2θ scans in Figure 3.7. The CuI film shows a preferred orientation along with the CuI <111> direction, as same as the results in Figure 3.2. Because the bottom layer is

amorphous materials of SZTO film or glass substrate, it is noted that the CuI (111) peak is not an epitaxial mode, but preferential orientation as confirmed in the previous chapter. Furthermore, the (111) orientation of the CuI film is a common feature in the CuI system due to the low surface stability energy of the CuI (111) plane [29]. The SZTO film cannot be distinguished in Figure 3.7 as the film is amorphous, as confirmed by the previous TEM and XPS studies [83], [84]. The extra peaks originated from the polycrystalline ITO film indicated as *I* in the figure.

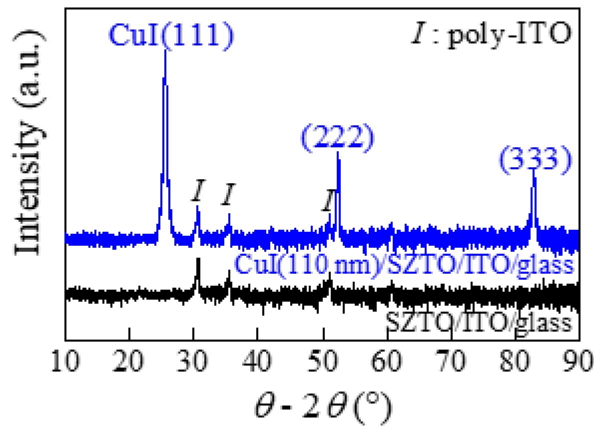

Figure 3.7 XRD θ - 2θ scan results of the CuI(110 nm)/SZTO/ITO/glass and SZTO/ITO/glass. The CuI film exhibits the preferential orientation of the CuI (111) plane and the additional peaks represent a polycrystalline ITO film indicated as *I*.

In addition, the average grain size of the CuI film has been estimated by the Debye-Scherrer formula in Equation 3.8 [85].

$$\beta_{total} - \beta_{inst} = \beta_{sample} = \frac{0.94\lambda}{D\cos\theta} \qquad \textbf{Equation 3.8}$$

where β is the full-width at half-maximum (FWHM), λ is the X-ray wavelength (Cu $K\alpha$ = 1.5406 Å), D is the crystallite size, and θ is the Bragg angle.

3.5 Current rectifying behavior of the *p*-CuI/*n*-SZTO diodes

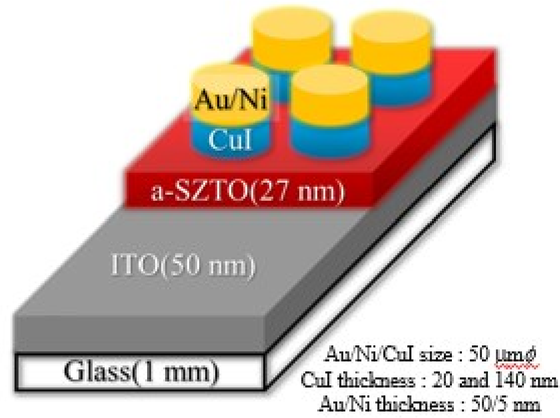

Figure 3.8 A schematic structure of the *p*-CuI/*n*-SiZnSnO (SZTO) diode grown on the ITO deposited glass substrate, which was used for electrical characterization. The CuI film of circular shape disk with a diameter of 50 μm was fabricated in two thicknesses of 20 nm and 140 nm, while the thicknesses of SZTO and ITO films were fixed as 27 nm and 50 nm, respectively. The metallic Au/Ni (*t* = 50/5 nm) films were subsequently deposited on top of the CuI film using the stencil mask.

Figure 3.8 exhibits *IV* curve results of the diodes before and after the N_2 annealing recorded by a semiconductor analyzer to conduct a transport study. To measure the *IV* curves, one probe tip was contacted to Au/Ni films for the *p*-type layer, and the other tip was connected to ITO film for the *n*-type layer, respectively. The resultant *IV* (black solid line) curve of the as-grown CuI(140 nm)/SZTO diode is shown in Figure 3.9. A drastic increase in the currnent level represents a turn-on voltage ($V_{\text{turn-on}}$) determined from a linear extrapolation of the *IV* curve as shown in the figure. The $V_{\text{turn-on}}$ of the as-grown diode was obtained to be 1.73 V. The bottom graph in Figure 3.9 displays the corresponding *jV* curve.

The clear current rectifying behavior was observed in both the *IV* and *jV* curves. Compared to the *p*-CuI/*n*-BSO as shown in the previous chapter, the most remarkable thing is that the off-current at -2 V has been quite suppressed, presumably due to the reduced structural defects and the oxygen vacancies by the high binding energy of Si-O. As we expected at the beginning, the amorphous *n*-type SZTO semiconductor makes that variation of the leakage-free diode under the off state. To further investigate the diode transport behavior, the measured *IV* curves were fitted in the overall voltage range from -2 V to + 2 V using the Shockley diode equation (Equation 3.9):

$$I(V) = I_s[\exp\{\frac{e(V - IR_s)}{\eta k_B T}\} - 1] + \frac{V - IR_s}{R_p} + I_o \qquad \textbf{Equation 3.9}$$

where I_s is the reverse saturation current, η is the ideality factor, k_B is the Boltzmann constant, T is the absolute temperature, I_o is the offset current, R_s is the series resistance, and R_p is the parallel resistance [64].

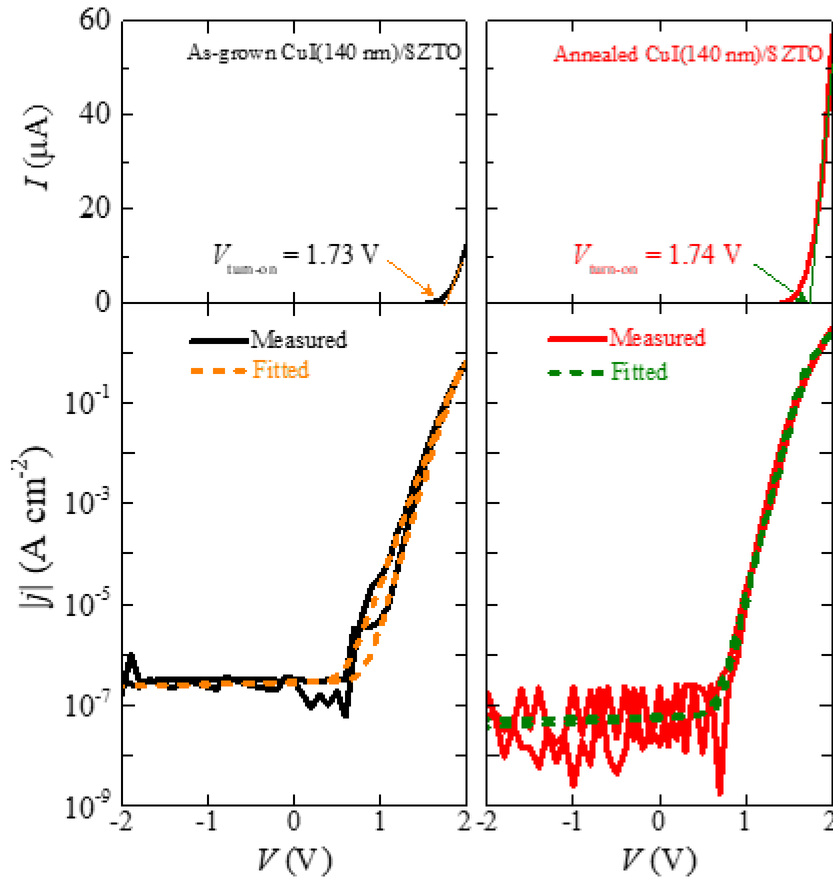

Figure 3.9 (Top) The current-voltage (*IV*) curve in a linear scale and (bottom) the corresponding current density-voltage (*jV*) curve in a semi-log scale of the as-grown (left) and the annealed (right) CuI(140 nm)/SZTO diode, respectively. The range and the green solid lines in the *IV* curves represent the linear extrapolation to determine the turn-on voltage of a diode, $V_{turn\text{-}on}$, while the range and the green dashed lines in the *jV* curves correspond to the diode fitting results obtained by the Shockley diode equation (Equation 3.9).

The orange lines for the as-grown diode in Figure 3.9 describe the fitting curves, which is consistent with the measured curves. It is noted that the slight difference between the fitting and the measured curves near 0.8 V is attributed to the irreversible charge trap effect. Similarly, the measured *IV* and *jV* curves in the annealed CuI(140 nm)/SZTO diode are plotted as red solid lines on the right side in Figure 3.9. Again, in the *jV* curves, apparent current rectifying behavior was observed with the increased current rectification

ratio (I_F/I_R) from 2.65 × 10^6 to 6.59 × 10^7. The green dashed lines of the jV curves represent the curve fitting results. What is the most prominent result in the annealed curve is the decrease (increase) of the current level in the negative (positive) bias region. Such a point is directly related to the increase of the I_F/I_R, where I_F is the current value at +2 V and I_R is the current at -2 V in this work. It is confirmed that the SZTO layer is thermally stable under CuI annealing conditions at 50 °C for 125 hrs. Thus, the enhancement of the I_F/I_R is attributed to the change in the electrical property of the CuI film. It is actually known that the copper vacancy V_{Cu} in the CuI acts as a dominant acceptor source and also as an ionized impurity scattering source as described in the previous chapter. In this situation, upon the N_2 thermal annealing at 50 °C for 125 hrs, iodine evaporation has occurred then iodine vacancies V_I can be additionally created, thereby compensating the native V_{Cu}. In addition to the compensation of V_{Cu} by V_I, thermal energy can give rise to the migration of point defects (V_{Cu} and V_I) from the inside of the film to the outside [80]. In order crossly check, similar to reduced grain boundaries from the AFM images of the CuI/glass, the change in the surface topography of CuI/glass, CuI/SZTO/ITO/glass, and SZTO/ITO/glass has been observed in Figure 3.10.

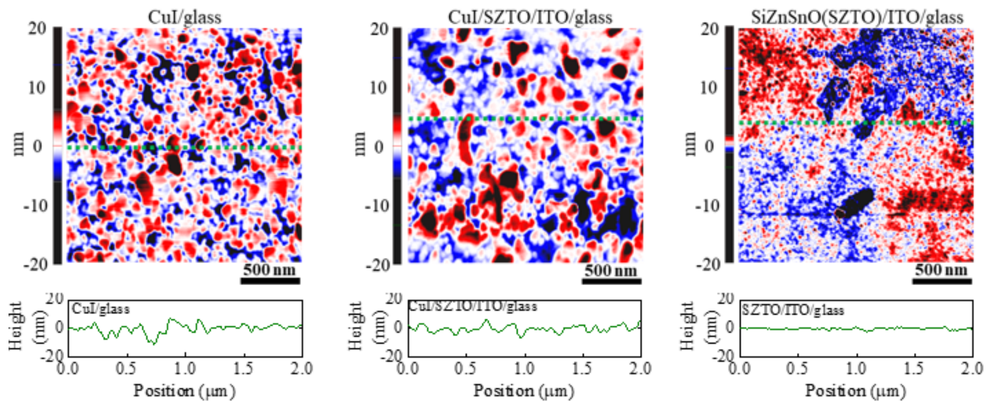

Figure 3.10 Surface topography images measured by AFM in a contact mode for the samples of (left) CuI(54 nm)/glass, (middle) CuI(110 nm)/SZTO/ITO/glass, and (right) SZTO/ITO/glass. The bottom panels show the line profiles along the green dotted lines

in the images.

A root-mean-square surface roughness (R_{rms}) of a polycrystalline CuI film is 3.11 nm in the entire area of 2 μm × 2 μm. The CuI film grown on top of SZTO/ITO/glass exhibits a similar value of 2.80 nm, indicating that the surface topography of the *p*-CuI/*n*-SZTO heterojunction is nearly maintained in the CuI film regardless of the bottom layers, and the film thickness (t_{CuI} = 54 nm or 110 nm). It is noted that the SZTO film has a smooth surface roughness of about 0.75 nm, which is much lower than the R_{rms} in the diode. Based on the experimental observations of reduced grain boundaries in the AFM images and the decrease of the *p* in the Hall effect results, it is highly likely that the N_2 thermal annealing can affect a positive influence on the *p*-CuI/*n*-SZTO diode.

Furthermore, several experimental observations support the improved diode characteristics in the *IV* or *jV* characteristics in Figure 3.9 after the annealing. That is the hysteresis of the *jV* curve between the forward and the reverse measurements, the $V_{turn\text{-}on}$ a bit increases from 1.73 V to 1.74 V, the offset current I_o decreases in the negative bias region from -2 to +0.7 V, and the noisy *jV* curve in the negative region. In order to further study transport mechanism, those behaviors should be discurssed microscopically one by one.

First, as explained before, irreversible charge traps mainly laed to diode hysteresis because free carriers are easily captured at the charged traps, such as V_{Cu}, resulting in the current flow delay with a slow responding component under an external bias voltage. On the other hands, the reduced hysteresis in the *jV* curve implys the reduced charged trap sites.

Second, the tiny increase of the $V_{turn\text{-}on}$ from 1.73 V to 1.74 V can support the reduced point defects. To understand this point, the difference between $V_{turn\text{-}on}$ and a threshold voltage V_{th}, which is an ideal voltage to begin the current flow, should be explained:

$$V_{th-p} = V_{bi} + |\Delta E_V / e|$$ **Equation 3.10**

$$V_{th-n} = V_{bi} + |\Delta E_C / e|$$ **Equation 3.11**

where V_{bi} is the built-in potential of a diode, e is the elementary charge, ΔE_V is the valance band offset, and ΔE_C is the conduction band offset between two semiconductors [29].

According to various physcial parameters, it turns out to be V_{bi} = 0.99 V, $|\Delta E_V/e|$ = 2.55 V, and $|\Delta E_C/e|$ = 2.89 V. It means that the $V_{th\text{-}p}$ and the $V_{th\text{-}n}$ are expected as 3.54 V for hole flow from *p*-CuI to *n*-SZTO and 2.89 V for electron flow from *n*-SZTO to *p*-CuI, respectively. It is thus likely that electrons are more favorable to move than the hole because the absolute conduction band offset value $|\Delta E_C/e|$ is 0.66 V less than $|\Delta E_V/e|$. The obtained $V_{turn\text{-}on}$ = 1.74 V in the *IV* curve of the annealed diode is apparently smaller than the calculated $V_{th\text{-}n}$ = 2.89 eV. Because the V_{Cu} forms an extra intermediate level that can act as a current path at the diode interface, the actual $V_{turn\text{-}on}$ should be lower than V_{th} in general. Thus, the subtle increased $V_{turn\text{-}on}$, in turn, demonstartes decreased V_{Cu} by the compensation of V_{Cu}.

Finally, the decrease of the I_o after the annealing refers to the reduced leakage current. The I_o often originates from the other leakage sources regardless of the bias voltage, probably due to instrumental factors or pinhole effects across two electrodes. If I_o exists at a diode, a constant current level has been appeared in the negative bias range. For CuI/SZTO diode case, the fitted I_o level of the as-grown *jV* curve is about 5.9 pA in the range from -2 to +0.7 V, whereas the I_o level was decreased in the annealed curve, which means that the side effect of the leakage source has been alleviated by the annealing. It seems that the

noise current has been increased, however, it should be noted that the instrument limitation is about ±1 pA, implying that the actual current is sufficiently low to reach the instrumental limit.

To compare the thermal annealing effect on the different thickness samples, we have identically measured the *IV* curves of the CuI(20 nm)/SZTO diode before and after the same N_2 annealing as shown in Figure 3.11. Sama as the thick diode, the apparent current rectifying feature was observed in the *IV* curve with a very low off current in the negative bias region. Moreover, the same effects, such as reduced and noisy off current level, increased $V_{turn\text{-}on}$, and the elimination of trap states at near 0.8 V, was appeared in the thin diode also. The *jV* curves have been fitted using the Shockley diode equation (Equation 3.9). Once again, the curve fitting results (orange and green dashed lines in the *jV* curve) show a well-matched curve with the measured data. The summarization of the diode parameters in the two diodes is provided in the next section with the explanation in detail.

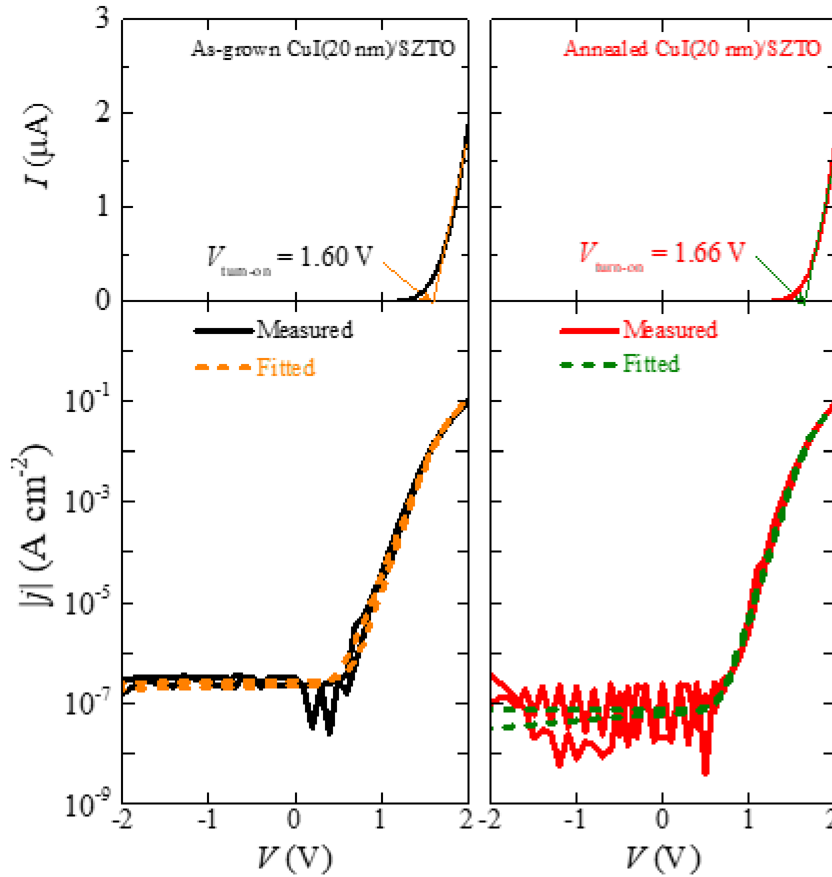

Figure 3.11 The current-voltage *IV* curve (top) in a linear scale and the current density-voltage (*jV*) curve (bottom) in a semi-log scale of (left) the as-grown and (right) the annealed CuI(20 nm)/SZTO diode. The orange and the green solid lines in the *IV* curves represent the linear extrapolation to determine the turn-on voltage $V_{turn-on}$ of a diode, while the dashed line in the *jV* curves corresponds to the diode fitting results based on Equation 3.9.

3.6 Diode curve fitting simulation

In this section, to further quantitative compare the diode parameters, all the obtained diode parameters, including I_F/I_R, I_o, I_s, η, R_s, and R_p, for both thin CuI(20 nm)/SZTO and

thick CuI(140 nm)/SZTO diodes with the annealing effects are summarized in Figure 3.12.

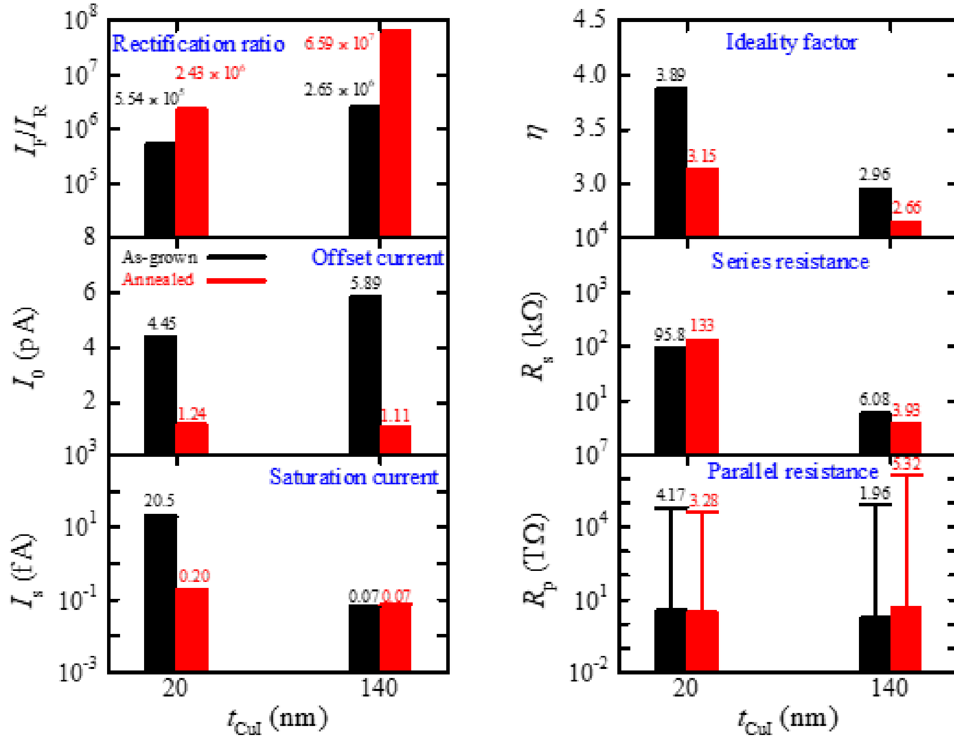

Figure 3.12 Summary of various diode parameters; the current rectification ratio I_F/I_R, the offset current I_o, the reverse saturation current I_s, the ideality factor η, the series resistance R_s, and the parallel resistance R_p. Black and red colors represent the data of the as-grown and annealed diode, respectively. All the parameters are estimated by fitting the *IV* curve results with Equation 3.9. Error bars represent the least square fitting error. The other parameters exhibit low fitting errors of less than 5 %, except for the parallel resistance.

Here, it should be reminded of the physical significance of individual parameters. The most important parameter among the various parameters is the current rectification ratio I_F/I_R, which is defined as the ratio between I_F and I_R, where I_F is the current level at a positive voltage (+2 V in our case) and I_R is the current level as a negative voltage (-2 V in our case). The high I_F/I_R stands for the well-operating diode with the high performance since if the diode shows a high I_F/I_R, then the current can easily flow in the positive region,

while the carrier flow has been blocked by the built-in potential to result in the low I_R. In other words, the high I_F/I_R means the high current rectifying behavior of the diode. It is thus highly likely that the high I_F/I_R should be obtained to facilitate the diode as optoelectronics. The offset current I_o is the same as the leakage current irrelevant to the bias voltage induced by instrumental factors or defects. The I_s refers to the reverse saturation current induced by the thermal drift of the minority carriers located at the space charge region at the diode interface. The η represents a diode transport mechanism; η is known to classify by diffusion (η = 1), recombination (η = 2), and numerous defects region (η > 2). The R_s describes the contact resistance at several interfaces between two films (or between film and substrate), and the R_p displays the parasitic parallel resistance ocurred by the leakage current.

For the thick CuI(140 nm)/SZTO diode case, all the parameters have been varied by the thermal annealing, such as the increase of I_F/I_R from 2.7×10^6 to 6.6×10^7 by about 25 times, the decrease of I_o from 5.9 pA to 1.1 pA, the almost constnat I_s being a low value of 0.07 fA, the decrease of η from 2.96 to 2.66, the decrease of R_s from 6.1 to 3.9 kΩ, and the subtle increase of R_p from 2 to 5 TΩ. The variations of diode parameters can be understoode based on the possible processes; the decrease of charged trap states of V_{Cu}, the decrease of grain boundaries by the out-diffusion of V_{Cu}, and the decreased of ionized impurity scattering. The reduced I_o represents that unintended leakage sources, such as pinholes across the CuI film are reduced by the reduced defects, *p*-type carriers, grain boundaries, etc. On the other hand, the R_s between the CuI film and the metallic Au/Ni films, the reduced grain boundaries can be influenced further. Moreover, the η = 2.96 of as-grown diode represents that the diode has a lot of defects at the interface, whereas the η = 2.66 demonstrates that the interface has been improved. The increase of R_p by about 3 TΩ also shows the reduced V_{Cu}, albeit having a large least-square fitting error close to the

instrumental measurement limitation. The I_s remains nearly constant, presumably due to sufficient low value under this configuration. Overall variations coherently explain that the annealing can improve the diode performance and the corresponding I_F/I_R was increased by about 25 times in the best-performing specimen.

In the case of the CuI(20 nm)/SZTO diode, diode parameters are changed; the decrease of I_o from 4.5 pA to 1.2 pA, the decrease of I_s from 20.5 fA to 0.20 fA, the decrease of η from 3.89 to 3.15, and the nearly same R_p of 4 TΩ. The initial values of I_s and η in the as-grown film seem to be all larger than the corresponding values for the CuI(140 nm)/SZTO diode, while I_o and R_p are comparable in the two diodes. It means that the V_{Cu} and grain boundary effects are much more dominant in the thin film, which shows the numerous defect behavior ($\eta = 3.89$). As the diode annealed, all the parameters of I_o, I_s, and η have been coherently improved as described in the thick diode. It is thus likely that the thermal annealing on the CuI film is one of the effective ways to improve the diode performance by reducing V_{Cu}, grain boundaries, and ionized impurity scattering.

The most noticeable discrepancy between the thin and the thick diodes is the variation of R_s and I_F/I_R. Upon conducting the thermal annealing, R_s increases from 95.8 to 133 kΩ, while I_F/I_R slightly linceases from 5.5×10^5 to 2.4×10^6. Note that the I_F/I_R was estimated from the fitting results to roll out the noise-rendered errors from the I_R. The R_s is commonly appearing that the I_F as the forward-biased current is dropped by the contact resistance at a few interfaces. Thus, the I_F is supposed to decrease, being roughly proportional to R_s. In other words, the moderate increase of I_F/I_R by a factor of 4 in the thin diode, as compared with the factor of 25 increase in the thick diode originates from the unintended R_s increasement. That is, if R_s degradation did not occur, the thin diode should have shown better diode performance. The unexpected increase of R_s by the annealing implies that the 20-nm-thick CuI film just begins to deteriorate, probably due to the formation of excess V_I.

The thermally degraded CuI film is typically observed in both thin films (t_{CuI} < 100 nm) [80] and even in a single crystal [79]. Therefore, especially for a very thin film limit of t_{CuI} < 100 nm, a short time or low-temperature annealing might be required to reach a high I_F/I_R.

To further investigate diode parameters one by one in more detail, we have conducted curve fitting simulations with the representative specimen of the as-grown CuI(140 nm)/SZTO diode. Figure 3.13 shows the η variations fixing the other parameters.

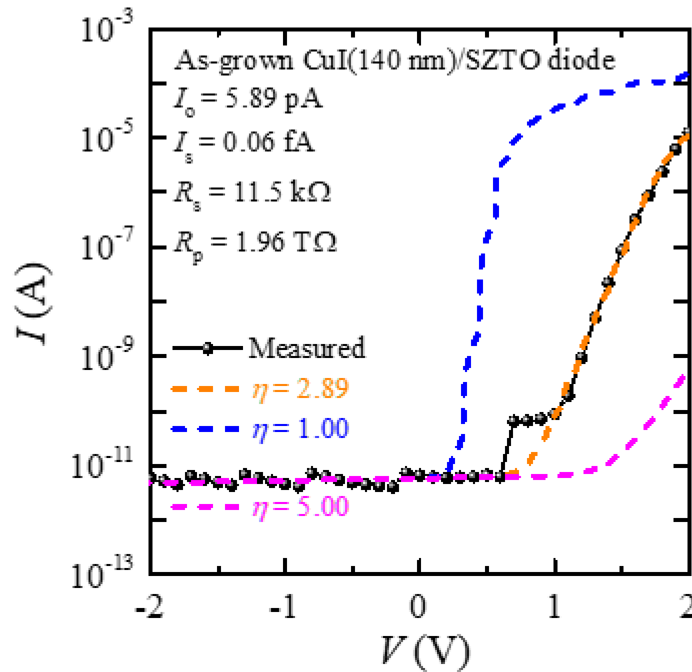

Figure 3.13 Curve fitting simulation results with the η variation. The other diode parameters were fixed during the change in the η. The matched η with the measured curve is 2.89.

The η explains the dominant transport mechanism at the diode interface. When the η is close to 1, its behavior follows well the ideal model and the current drastically increases with the increasing of bias voltage, whereas as the η increases, there exist many defects in the diode interface and the current increment is tardy.

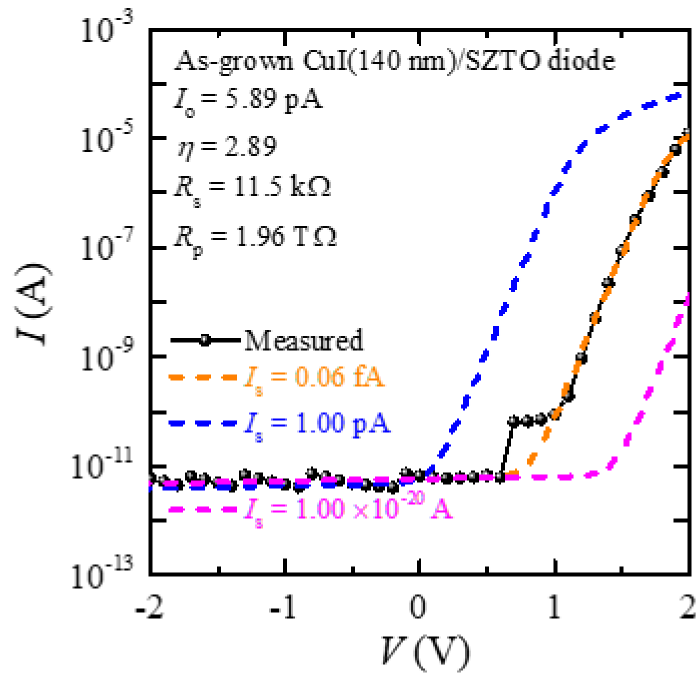

Figure 3.14 Curve fitting simulation results with the I_s variation. The other diode parameters were fixed during the change in the I_s. The matched I_s with the measured curve is 0.06 fA.

The reverse saturation current I_s expresses the current generated by thermal effects or interface drift. A low I_s makes the downward shift of the *IV* curve and a high I_s is vice versa as shown in Figure 3.14.

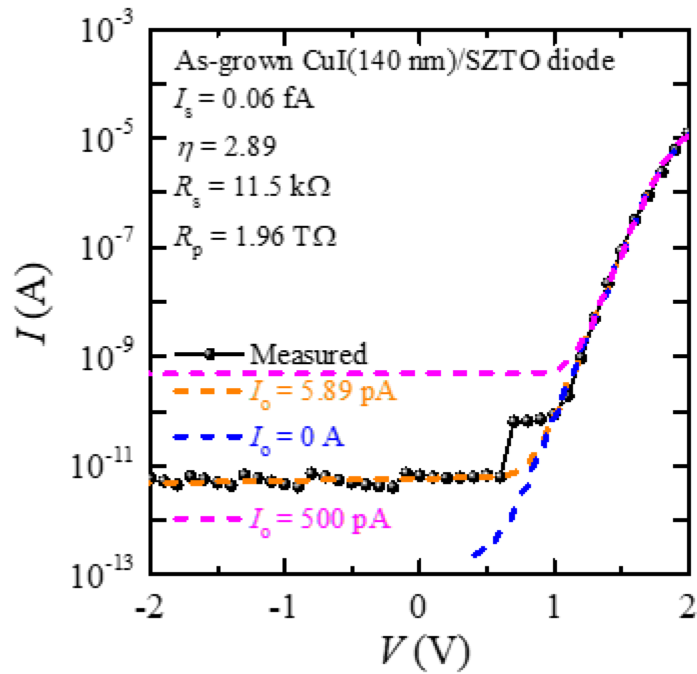

Figure 3.15 Curve fitting simulation results with the I_o variation. The other diode parameters were fixed during the change in the I_o. The matched I_o with the measured curve is 5.89 pA.

In Figure 3.15, the I_o is the offset current, which is determined by a leakage current component and a constant current level irrelevant to the bias voltage during the voltage sweeping. The change in the I_o provides the base current shift to up or downward.

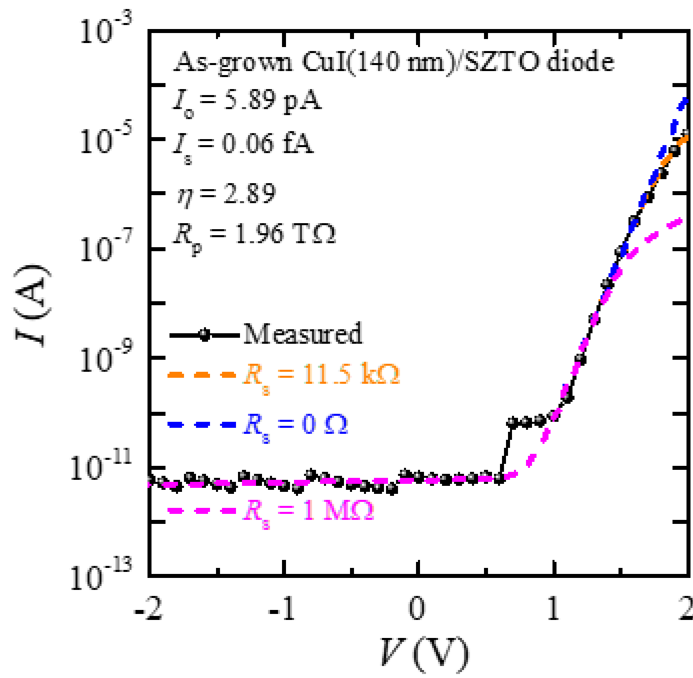

Figure 3.16 Curve fitting simulation results with the R_s variation. The other diode parameters were fixed during the change in the R_s. The matched R_s with the measured curve is 11.5 kΩ.

Figure 3.16 displays the variation with the R_s, which is the series resistance due to the contact resistance. It is attributed to mainly electrode-semiconductor interface contact, *pn* diode interface, and metal-metal junction to result in the drop of the flowing current at the high positive bias region.

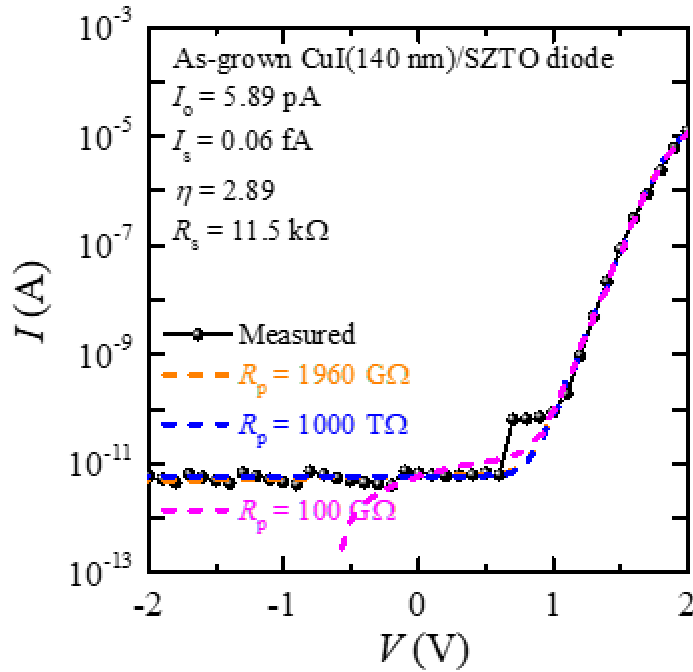

Figure 3.17 Curve fitting simulation results with the R_p variation. The other diode parameters were fixed during the change in the R_p. The matched R_p with the measured curve is 1960 GΩ.

The parasitic parallel resistance R_p is varied in Figure 3.17. Since the R_p represents the capability of blocking the current flow in the negative state, a high R_p indicates that the diode effectively impedes the current flow at the off state, while a low R_p can flow the current at the off state to result in the generation of the leakage current.

In summary for the diode curve fitting simulation of the as-grown CuI(140 nm)/SZTO diode, the overall diode transport has been improved by the thermal annealing; the decrease of η and R_s by the better interface formation and film quality due to the inter-diffusion process, the decrease of I_o and I_s by the use of amorphous material as well as reduction of structural and point defects. It is thus likely that optimal annealing conditions can be further improved the diode performance for each thin film with a different CuI film thickness, even though the thin diode does not have the best performance.

3.7 Comparison of a high current rectification ratio of the *p*-CuI/*n*-SZTO heterojunction diode

We obtained a high current rectification ratio of the *p*-CuI/*n*-SZTO heterojunction diodes with the physical interpretation in the previous sections. It is highlighted that $I_F/I_R = 6.6 \times 10^7$ is fairly high among the CuI-based heterojunctions. In this section, the I_F/I_R values of various *pn* diodes, composed of the *p*-CuI film and *n*-type semiconductors, are summarized and compared. Figure 3.18 shows the I_F/I_R of the CuI/SZTO and of the other CuI-based heterojunction diodes having at least high I_F/I_R over 10^5.

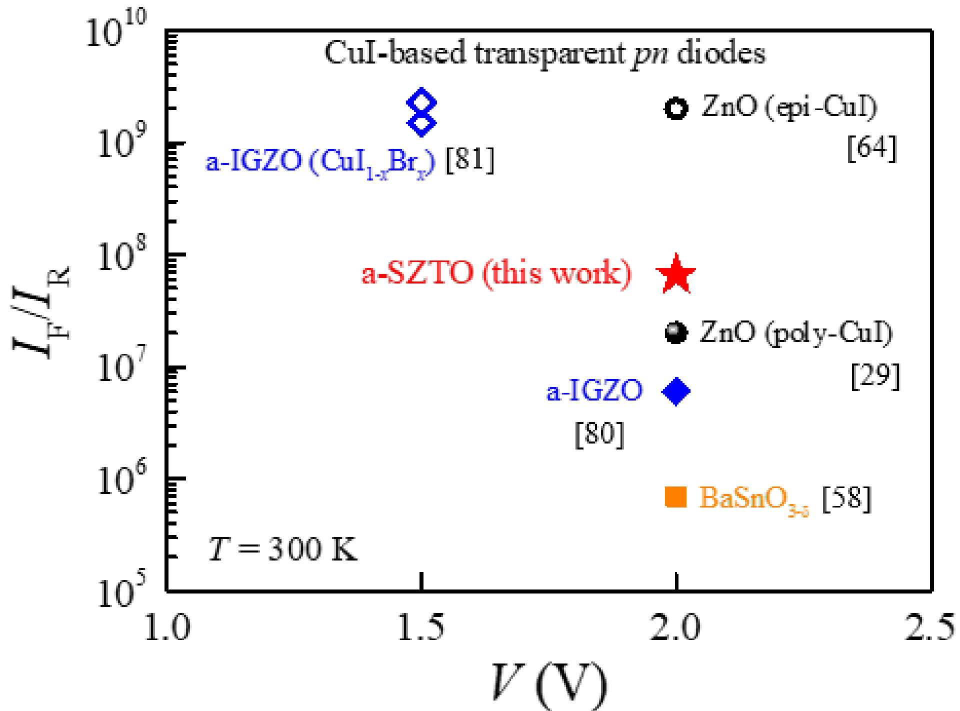

Figure 3.18 Comparison of the current rectification ratios I_F/I_R of various heterojunction diodes composed of the *p*-CuI film. The color indicates different *n*-type films for the *pn* diodes and here high I_F/I_R values over 10^5 are summarized only. The

I_F/I_R of the CuI/SZTO diode is obtained by the fitted values of I_F at +2 V and I_R at -2 V. The I_F/I_R of the $CuI_{1-x}Br_x$/IGZO diode is estimated by the measured I_F at +1.5 V and the fitted reverse saturation current [81]. The I_F/I_R of CuI/ZnO [29],[64], CuI/IGZO [80], and CuI/$BaSnO_{3-\delta}$ [58] diodes are calculated from the measured data at ±2 V.

The highest value is about 2×10^9 for the CuI/ZnO diode which is a higher value than the CuI/SZTO diode by about 30 times, while it requires specific growth conditions, for example, an epitaxial CuI film on top of an epitaxial ZnO film using the tricky method. It means that the high I_F/I_R value is hard to reproduce in a flexible device that needs often a low-temperature growth condition [64]. Although the I_F/I_R of about 10^9 in the $CuI_{1-x}Br_x$ diodes seems to be higher than the CuI/SZTO diode, a precise study should be necessary because they used the measured I_F and the fitted I_s to extract the I_F/I_R not using the measured I_R [81]. The exact values for all the summarized diodes are provided in Table 3.1. Focusing to the CuI/SZTO diode, I_F/I_R, which is the crucial parameter to characterize diode performance, is high enough except for two devices [86], [87]. The ideality factor η for the epitaxial ZnO-based and the amorphous IGZO-based didoes look lower than 2, while the present SZTO-based diode is about 2.8, indicating that undesirable disorders of the CuI film can be more mitigated by the optimum annealing or deposition conditions. The low I_s of the CuI/SZTO diode is attributed to the incorporation of the offset current I_o and the I_s in the fitting sequence. Albeit, the R_s of the CuI/SZTO diode is still higher than the other diodes, it refers to the diode performance can be further enhanced if the interface resistance will be further reduced. It is thus likely that the I_F/I_R will become higher by improving the R_s and the η. In order to instruct a future direction for applications, recent results for the photoresponse are also summarized in Table 3.1. Nowadays, the UV photodetector has been actively tested in the transparent *pn* diode made of the *p*-CuI, so that the CuI/SZTO diode can be utilized as the self-powered UV photodetector with flexibility, optical transparency, and a competitive price, once realized.

Table 3.1 Summary of diode parameters for various different *pn* junctions, consisting of the *p*-CuI films.

pn diode	Current rectification ratio I_F/I_R	Saturation current (A) I_s	Ideality factor η	Series resistance (Ω) R_s	Parallel resistance (Ω) R_p	Responsivity (wavelength) (mA W^{-1})
pc-CuI/epi-ZnO [29]	$2 \times 10^7 \pm 2$ V	1.3×10^{-11}	1.7	2.9×10^2	$> 10^{12}$	-
pc-CuI/epi-ZnO [29]	$4 \times 10^7 \pm 2$ V	6.2×10^{-15}	1.6	2.0×10^2	$> 10^{12}$	-
pc-CuI/epi-ZnO [29]	$2 \times 10^7 \pm 2$ V	3.2×10^{-13}	1.8	2.5×10^2	$> 10^{12}$	-
epi-CuI/epi-ZnO [64]	$2 \times 10^9 \pm 2$ V	1.1×10^{-12}	1.7	1.7×10^2	3×10^{12}	-
pc-CuI/epi-$BaSnO_{3-\delta}$ [58]	$7 \times 10^5 \pm 2$ V	9.9×10^{-13}	1.5	$\sim 5.5 \times 10^2$	2×10^9	-
pc-CuI/a-InGaZnO [80]	$6 \times 10^6 \pm 2$ V	-	1.6	2.0×10^2	-	0.3 (365 nm)
pc-$CuI_{1-x}Br_x$/a-InGaZnO [81]	$\sim 2 \times 10^9 \pm 1.5$ V	$\sim 2 \times 10^{-12}$	1.9	-	-	-
np-CuI/sc-$CsPbBr_3$ [86]	$3 \times 10^2 \pm 2$ V	-	-	-	-	1.4 (540 nm)
pc-CuI/sc-Ga_2O_3 [87]	$6 \times 10^3 \pm 2$ V	-	3.7	-	-	2.49 (254 nm)
pc-CuI(20 nm)/a-SiZnSnO [88]	$2 \times 10^6 \pm 2$ V	2.0×10^{-16}	3.2	1.3×10^5	3×10^{12}	-
pc-CuI(140 nm)/a-SiZnSnO [88]	$7 \times 10^7 \pm 2$ V	0.7×10^{-16}	2.7	3.9×10^3	5×10^{12}	-

epi: epitaxial film, pc: polycrystalline film, sc: single crystal, a: amorphous, np: nanoparticle

3.8 The electronic band alignment and the type-II energy band diagram

To better understand the diode transport mechanism, the electronic bands of various semiconductors are lined up in accordance with the vacuum energy level $E_{vac} = 0$, based on the experimental results from the literature. Figure 3.19 represents the electronic band alignment of various wide bandgap semiconductors, including CuI [29], [58], SZTO [76], [84], IGZO [56], [90], $BaSnO_3$ [12], [58], and ITO [91].

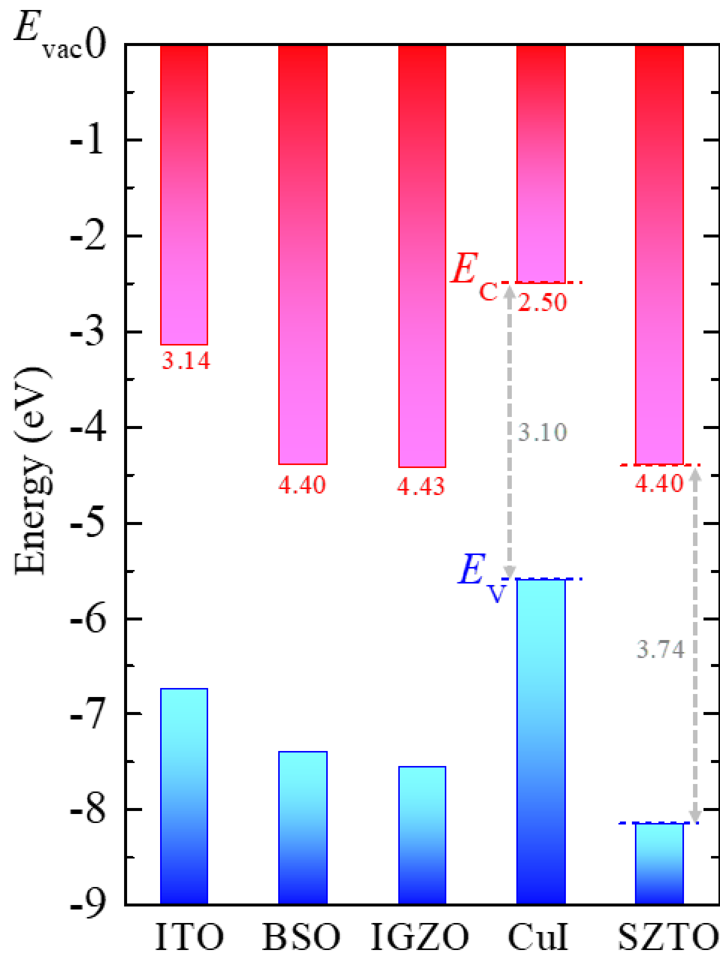

Figure 3.19 Electronic band alignment of several wide bandgap materials, including ITO, BSO, IGZO, CuI, and SZTO. The band energies of those materials are aligned at the vacuum energy level E_{vac} = 0.

The red top and blue bottom lines show the allowed conduction and valance states, respectively. To construct the energy band diagram, E_{vac}, valance band maximum E_V, and conduction band minimum E_C should be established first from the alignment. Then, the Fermi energy level E_F can be determined using the Anderson model for heterojunction diode [92] with various input physical parameters summarized in Table 3.2.

Table 3.2 Various input parameters of the Anderson heterojunction diode model for the annealed *p*-CuI/*n*-SZTO diode, where m_o is the electron mass.

Film	Bandgap (eV)	Electron affinity (eV)	Carrier density (cm^{-3})	Dielectric constant	Effective mass
p-CuI	3.1	2.5 [29]	9.4×10^{18}	5.1 [29]	$1.4m_o$ [93]
n-SZTO	3.7 [76]	4.4 [76]	6.8×10^{15} [76]	4.75 [84]	$0.2m_o$ [84]

Figure 3.20 exhibits the obtained band diagram that shows the type-II band alignment, in which the E_C of the *n*-type semiconductor is located inside of the E_g of the *p*-type semiconductor. The V_{bi}, depletion widths of *p*-CuI and *n*-SZTO are estimated as 0.99 V, 0.03 nm, and 37.1 nm, respectively. Moreover, the realized CuI/SZTO diode is practically the one-side abrupt junction, indicating that the most of the space charge region is positioned at the *n*-type SZTO side. Basically, the SZTO thickness (27 nm) is shorter than the *n*-type depletion length (37.1 nm). It is thus likely that a specific forward bias voltage should be required to erase the electric field for the current flow through the *pn* junction because the effective negative bias voltage is generated at the diode interface. In the *jV* curves, as shown in Figure 3.9 and in Figure 3.11, relatively high bias voltages were applied to the current flow, which is consistent with the above explanation. Another potential capability of the type-II band alignment is that such band type is preferred in many optoelectronic devices since free carriers can be easily separated by the built-in potential without immediate recombination due to the electronic band structure.

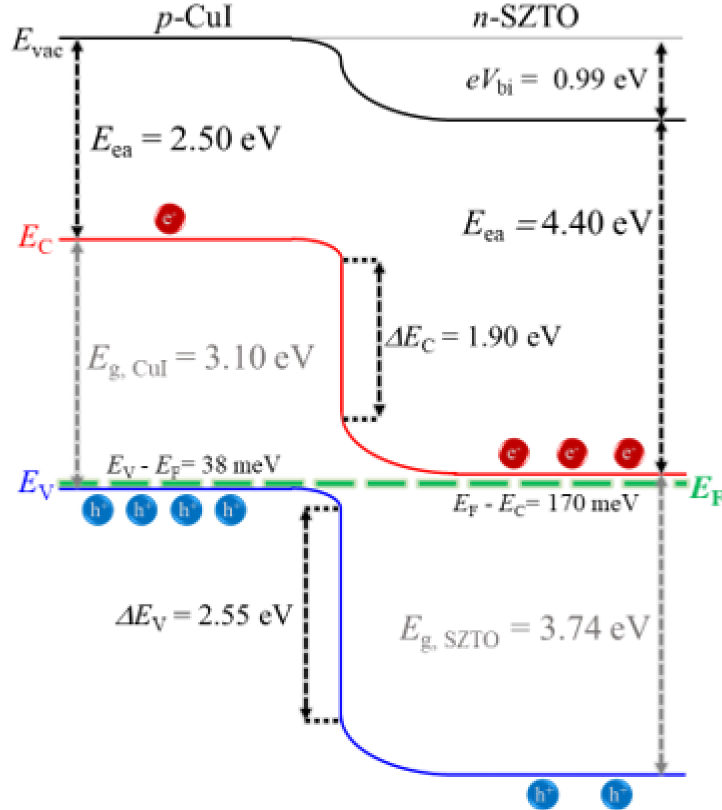

Figure 3.20 A proposed energy band diagram of the annealed CuI(140 nm)/SZTO diode representatively, based on the Anderson heterojunction diode model, exhibiting the type-II band alignment.

3.9 Summary

In chapter 3, the electrical properties of transparent *p*-CuI/*n*-SiZnSnO (SZTO) heterojunction diodes have been investigated upon variying with the CuI film thicknesses. To deposit the (111) oriented polycrystalline CuI and amorphous SZTO films, thermal evaporation and RF magnetron sputtering were used, respectively. The resultant CuI film was annealed at 50 °C for 125 hrs under an N_2 gas atmosphere to improve film quality and

diode performance. By the thermal annealing, the key diode parameter current rectification ratio I_F/I_R for the CuI(140 nm)/SZTO diode has been enhanced by about 25 times up to 6.6 $\times 10^7$. Moreover, all the diode parameters as systematically obtained by the curve fitting results from the Shockley diode equation are also improved by the annealing. Otherwise, the I_F/I_R of the CuI(20 nm)/SZTO diode has been moderately increased by about 4 times up to 2.4 $\times 10^6$, presumably due to the R_s increase. Thus, followed by the change in the CuI thickness with the estimated diode fitting parameters, the diode transport mechanism has been studied systematically. Furthermore, the physical explanation for all the diode parameters was systematically investigated upon varying the parameters using curve fitting simulation. On the basis of the electronic band alignment, the CuI/SZTO diode has been proposed as the type-II band diagram, which is a favorable band type for the device application. Therefore, the realized transparent *p*-CuI/*n*-SZTO heterojunction diode is likely to be a useful transparent active component in many optoelectronic devices, especially for LEDs or UV photodetectors.

Chapter 4 Investigation of a self-powered CuI/SiZnSnO UV photodetector

4.1 Overview

In this chapter, we have studied the photoresponse of the realized *p*-CuI/*n*-SZTO heterojunction diode as a photodetector constituent. Last decade, various CuI-based *pn* heterojunctions have been investigated to facilitate the diode as many optoelectronic devices, such as solar cells [94] LEDs [37], and UV photodetectors [38]. Because the CuI has a direct bandgap energy of about 3.1 eV, the CuI can absorb the UV light and shows transparency under the visible light. Thus, the CuI-based *pn* diodes can generate the photocurrent without any external bias voltage at 0 V by absorbing the UV light. In order to exploit the versatile physical properties of the CuI film, very recently various results have been reported for the CuI-based self-powered (zero bias) UV photodetector by many material groups [38], [87], [89], [95]. The self-powered UV photodetector can be an important component of smart windows for future automobiles or building constituents. In this regards, many types of CuI-based *pn* heterojunction diodes have been tested to realize a high-performance UV photodetector. We also have focused on those photodetector studies to utilize the transparent *p*-CuI/*n*-SZTO diode. The origin of the photocurrent on the CuI/SZTO diode was systematically investigated. Furthermore, a non-uniform pinhole with a large size, which can be a main leakage source, has been figured out by comparing the different sizes of the two junctions. With decreasing in the junction area, the corresponding responsivity value increases and reach a high value of 18.1 mA W^{-1} at 320 nm. The obtained responsivity was compared to the other CuI-based self-powered UV photodetectors to confirm the potential merit of the CuI/SZTO photodetector.

4.2 Establishment of the photocurrent measurement setup

In order to study the photocurrent of the *pn* junction diodes, a light illumination system is required. We established an experimental setup for photocurrent measurements, consisting of various components; a 150 W Xe arc lamp (LS 150 xenon arc lamp source, Abet Technologies), a custom-made ventilating Hume hood for ozone gas evacuation created from the Xe arc lamp, an optical chopper with a duty cycle of 50 % (SR540, Stanford Research Systems), 150 mm focal length monochromator (MonoRa150i, Dongwoo Optron), micro probestation (MPS-PTH, Nextron), semiconductor characterization system (KE4200, Keithley) as shown in Figure 4.1. The constructed photocurrent system can modulate wide-range light from 200 to 1200 nm with a frequency variation in a range of 2 – 400 Hz.

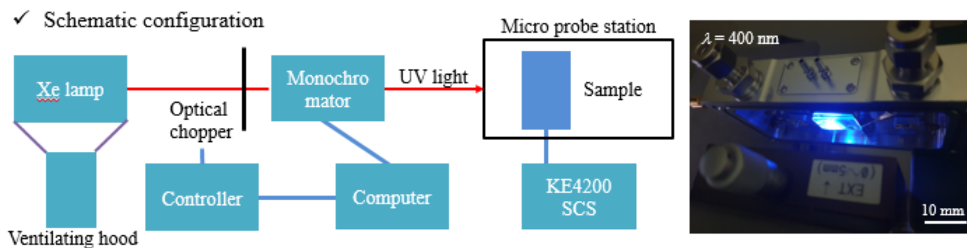

Figure 4.1 Schematic configuration of the built photocurrent setup. The specimen is loaded using the micro probestation, which can be directly attached to the monochromator exit port. The actual photograph demonstrates the sample loading during the light illumination at 400 nm.

After finishing the photocurrent setup, the light power was measured using a power meter (PM100D with a UV extended Si photodetector S120VC, Thorlabs.). The commercial Si PIN photodiode (S1722-01, Hamamatsu) was used to verify whether the system was working well or not. Figure 4.2 shows the calibrated light power density and

the responsivity curve of commercial Si photodiode compared to the spec sheet data. The obtained responsivity curve, which is defined as the photocurrent to the input power density, is indeed consistent with the provided data, indicating that the constructed photocurrent measurement system is working well.

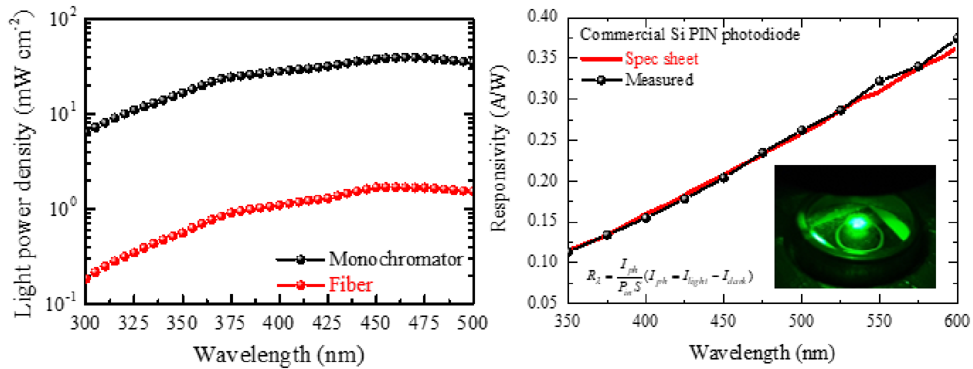

Figure 4.2 (left) Light power density which measured at the monochromator exit port and optical fiber, respectively. (right) The measured responsivity curve of the commercial Si PIN diode compared to the spec sheet data, where R_λ is the responsivity, I_{ph} is the photocurrent, I_{light} is the current under the light illumination, I_{dark} is the dark current, P_{in} is the incident light power, S is the effective illumination area.

Furthermore, in order to investigate the frequency-dependent photocurrent, a 500 MHz oscilloscope (WaveRunner 6051, LeCroy) and lock-in amplifier (SR830, Stanford Research Systems), and low noise voltage preamplifier (SR560, Stanford Research Systems) were used as shown in Figure 4.3.

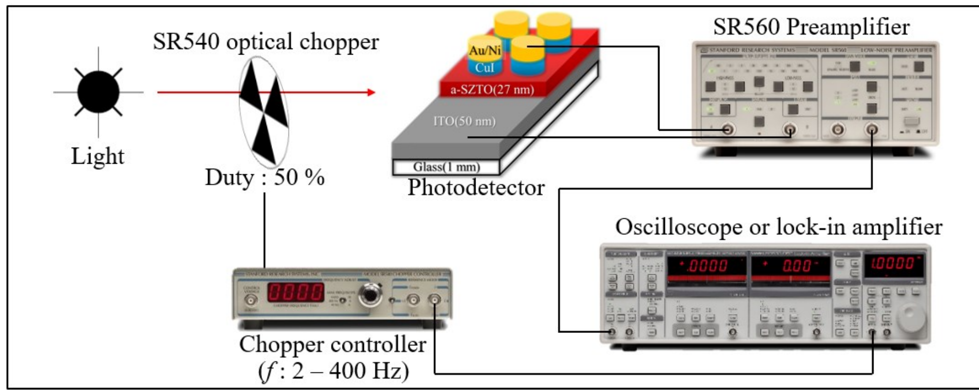

Figure 4.3 Schematic diagram of the frequency-dependent photocurrent measurement setup. The same light source of the Xe arc lamp and the monochromator as the wavelength switching system was used to generate the UV light.

4.3 Characterization of the CuI/SZTO photodetector

To investigate the photodetector performance, a transparent *p*-CuI/*n*-SZTO heterojunction diode was used as a photodiode in Figure 4.4. The lateral *pn* junction area is about 10 mm × 4 mm and Au/Ni (2/2 nm) metallic electrodes have an average width of 147 μm and length of 1.28 cm, respectively. The detailed information for film growth is described in section 3.4.

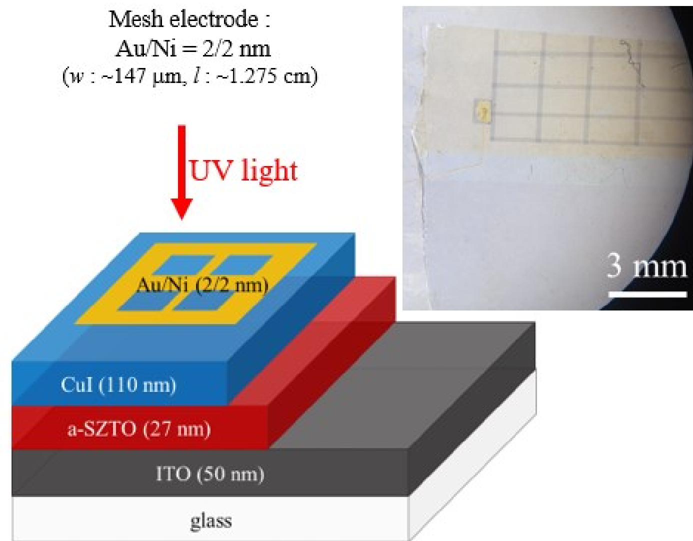

Figure 4.4 Schematic structure and actual photograph of CuI(110 nm)/SZTO(27 nm)/ITO/glass for photoresponse measurements.

Before conducting the photocurrent measurements, fundamental physical properties of the CuI/SZTO diode shown in Figure 4.4 have been investigated. First of all, Figure 4.5 shows XRD θ - 2θ scan results on the CuI/SZTO/ITO/glass and SZTO/ITO/glass. The consistent data was obtained with the previous observation in section 3.4.

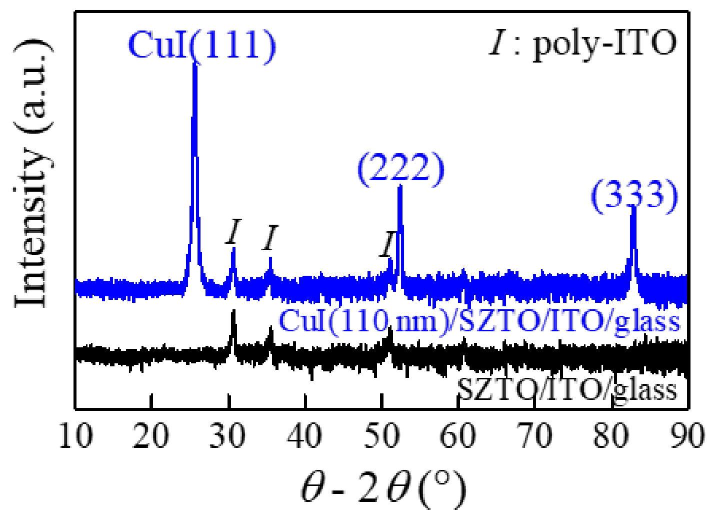

Figure 4.5 XRD θ- 2θ scan results of the CuI(110 nm)/SZTO/ITO/glass and SZTO/ITO/glass. The CuI film exhibits the preferential orientation of the CuI (111) plane and the additional peaks represent a polycrystalline ITO film indicated as *I*.

Here, we have found that the estimated average grain size from the Debye-Scherrer formula (Equation 3.8) is about 40 nm, which is a macroscopic observation including pinhole effects. In order to confirm the exact grain and pinhole sizes, local scanning experiments have been performed using field-emission scanning electron microscopy (FE-SEM) in Figure 4.6. The average grain size is estimated as 51.1 nm, which is slightly larger than the XRD results, presumably due to the microscopic estimation excluding pinholes. And, a large-size pinhole, which has larger than the grain size, was observed. Grain boundaries and pinholes often can influence electrical transport. These kinds of pinholes induce the leakage current, thereby degrading the photodetector performance.

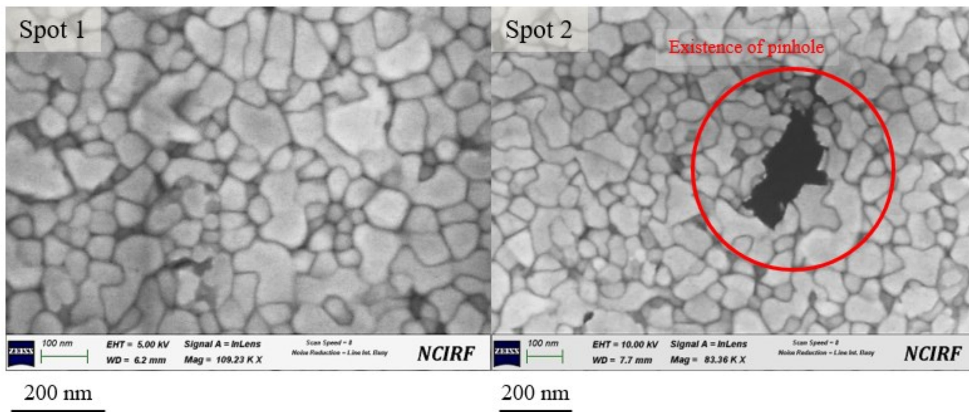

Figure 4.6 Top-view FE-SEM images of CuI/SZTO/ITO/glass specimen at different measured spots. Many grains with an average grain size of about 51.1 nm and the non-uniform large-size pinholes are observed.

The existence of the large-size pinholes gives arise to make direct contact between the top electrode and the *n*-type layer without passing through the *p*-type layer. In this situation, when the CuI film area increase, the probability of involvement of the pinhole gets higher to result in the non-rectifying *IV* behavior as shown in Figure 4.7. Once the leakage current

appeared in the *IV* curve, the current rectifying behavior of the diode can not detect regardless of excitation illumination wavelength. However, even though the leakage current conceals the photocurrent, there is obviously a difference between under dark and illumination conditions in the enlarged *IV* curves.

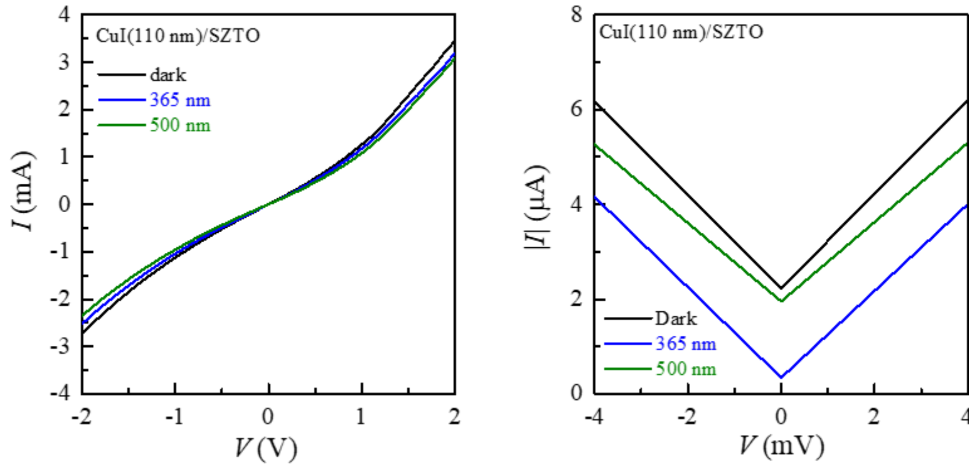

Figure 4.7 The current-voltage (*IV*) curves under various illumination wavelengths in a full-scale (left) and an enlarged scale (right). The *IV* curves are nearly overlapped due to the high leakage current induced by the pinholes.

4.4 Photocurrent of CuI/SZTO diode under the self-powered mode at 0 V

To further investigate photodetector performance, Figure 4.8 exhibits the spectral photocurrent, which is defined as the difference between dark and light current at zero bias voltage in Equation 4.1. The photocurrent increases with the increase of wavelength and then decreases after the 365 nm wavelength. It notes that the light source is not a fixed-intensity laser, but the Xe lamp combined with the monochromator, meaning that the light

power density can be varied with the change in the wavelength. By considering the variation of the light power density, spectral responsivity as a function of wavelength was investigated. The responsivity is defined as the followed equation;

$$R_\lambda = \frac{I_{ph}}{P_{in}S}(I_{ph} = I_{light} - I_{dark}) \quad \textbf{Equation 4.1}$$

where R_λ is the responsivity, I_{ph} is the photocurrent, I_{light} is the current under the light illumination, I_{dark} is the dark current, P_{in} is the incident light power density, S is the effective illumination area.

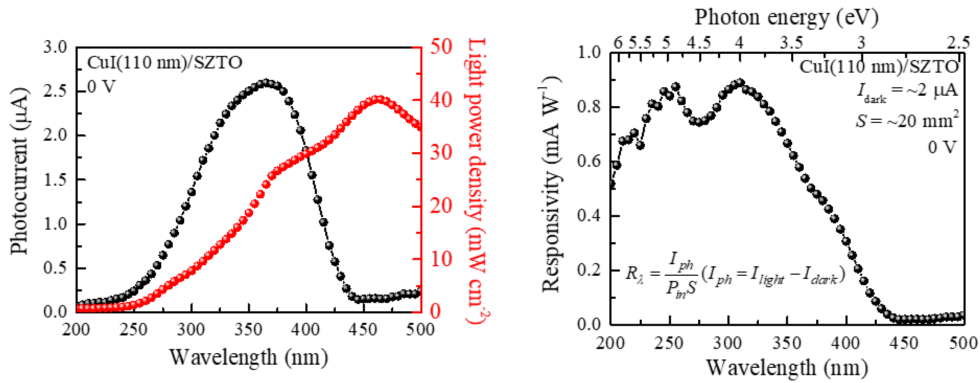

Figure 4.8 (left) The photocurrent and the incident light power density as a function of illumination wavelength. (right) The spectral responsivity at zero bias condition, which is a self-powered mode. The responsivity curve is obtained in Equation 4.1 by considering the effective illumination area *S* of the sample as 5 mm × 4 mm.

The obtained responsivity starts to increase at about 430 nm, exhibit peaks at 310 nm and at 260 nm, and then decreases with the decrease of the wavelength. The responsivity value at the maximum photocurrent wavelength of 365 nm is 0.54 mA W^{-1} and the maximum responsivity value at 310 nm is 0.89 mA W^{-1}. The main light-absorbing layer is the CuI film, having direct bandgap energy of about 3.1 eV, which is the same as 400 nm in wavelength. Thus, the starting point and the peak points should be figured out at least

intrinsically and it will be addressed in the next section.

To further investigate pinhole effects on the photodetector, upon increasing light intensity, the photovoltage was measured as shown in Figure 4.9. In order to clearly observe the waveforms using an oscilloscope, a low frequency of 1.4 Hz was tested at different intensities on the large-size CuI/SZTO photodetector. When the light intensity increases from 6.6 mW cm^{-2} to 23.0 mW cm^{-2}, the photovoltage increases that was fitted by the power-law equation described in Equation 4.2.

$$V_{ph}(I_{ph}) = AP_{in}^{\theta} \qquad \textbf{Equation 4.2}$$

where V_{ph} is the photo voltage, I_{ph} is the photocurrent, A is the proportional constant, and the θ is the power-law exponent.

The curve fitting was conducted to confirm the power-law exponent, which is the linearity relationship of the photo voltage to the incident light intensity. In other words, if the exponent closes to one, the photocurrent can be linearly generated to the incident light, whereas if the exponent is lower than one, then there might be some degrading factors, for instance in this case, mainly copper vacancy and pinhole.

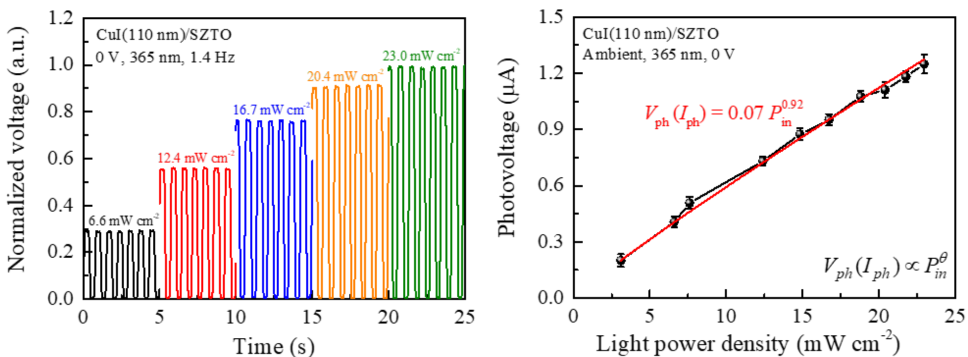

Figure 4.9 (left) Oscilloscope waveforms of the photovoltage switching on and off on the CuI/SZTO photodetector varying with the light intensity. The photo voltage

measurements were conducted at 0 V for self-powered conditions under the 365 nm illumination at 1.4 Hz. (right) The measured photo voltage as a function of the incident light power density. The light power density was calibrated by the effective light illumination area of 5 mm × 4 mm. The red solid line represents the power-law curve fitting results with the exponent information.

The long-term stability of the photo voltage on the CuI/SZTO photodetector is confirmed in Figure 4.10. The measurements were performed at 0 V under ambient conditions at 365 nm. The photodetector was preserved in air conditions until 6 weeks and preserved in a desiccator after that. It should be noted that it rained between 4 - 6 weeks. The most interesting thing is that the photo voltage drastically decreases to 25 % of the relative percentage, indicating that the CuI/SZTO photodetector can be acting as a water sensor. In order to check the reproducibility of the photo voltage, the photodetector was preserved in a desiccator after the decrease. As shown in the figure, the photovoltage was recovered from 96 μV to 130 μV after keeping the sample in a desiccator. Therefore, the time-dependent photo voltage curve shows reproducibility as well as long-term stability. The decrease of the photo voltage might be coming from the large-size pinholes because lots of dangling bonds exist at the pinholes, being able to capture the water molecule resulting in the degradation of the photodetector performance.

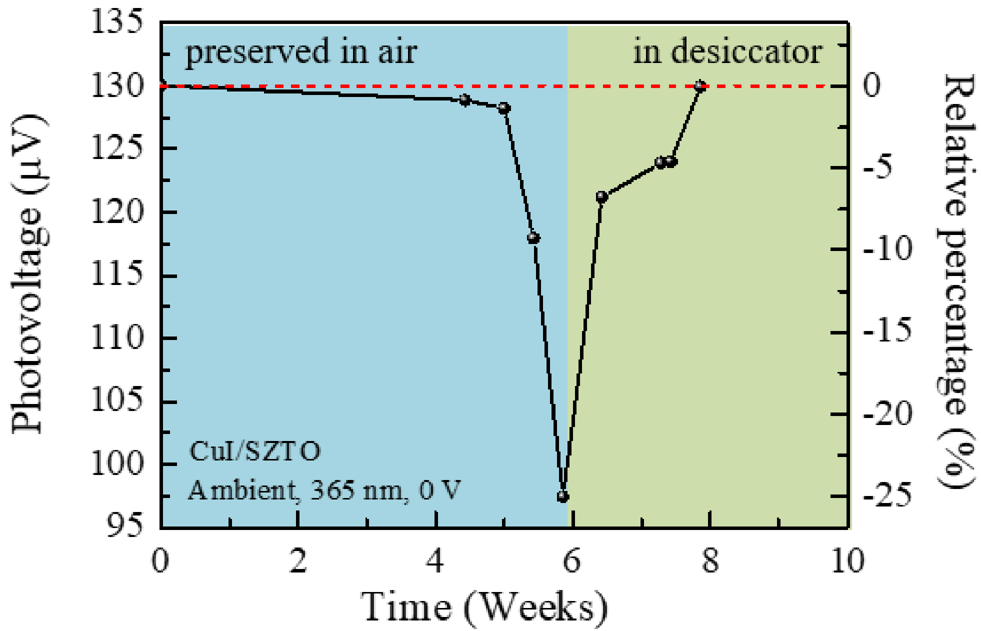

Figure 4.10 The quantitative photo voltage data as a function of time for checking the long-term stability of the CuI/SZTO photodetector. The photo voltage preserved in the air was decreased, presumably due to the high humidity between 4 - 6 weeks. Reproducibility of the photo voltage was confirmed by preserving the photodetector in a desiccator.

To investigate the frequency-dependent behavior of the realized photodetector, the phase-sensitive detection (PSD) measurements of the photo voltage on the CuI/SZTO photodetector were measured using the lock-in amplifier and the oscilloscope, respectively. Figure 4.11 exhibits the photo voltage sweeping the light modulation frequency of 365 nm illumination at 0 V, measured by two apparatus of the oscilloscope and lock-in amplifier, which provide the same photo voltage results. It is worth noting that the voltage values of the lock-in amplifier are the indeed root-mean-square (rms) values, whereas the oscilloscope displays the peak-to-peak values from actual waveforms. We have converted the rms values of lock-in values to the peak-to-peak values by considering the waveforms. The resultant photo voltages are well-matched with each other. The cutoff frequency (f_{3dB}) implies the device's operating bandwidth, which is defined at 70.7 % of photo voltage to

the maximum point. The estimated cutoff frequency is 57.1 Hz, indicating that the CuI/SZTO photodetector can operate in wide-range than the other CuI-based self-powered UV photodetectors [89].

In order to maintain the steady-state conditions to prevent the remnant effect just before measurements during the photo current measurements, the measurements were performed over a sufficient time at least 10 seconds waiting for every point. Here, the voltages R, X, and Y indicate the total, intrinsic, and capacitive voltages, respectively. In general, defects show a slow time reaction by capturing the photo-generated carriers resulting in the delay of the photo current. It is thus likely that the voltage Y term is referred to as the defective term of the photodetector.

To check whether the photo voltage is delayed or not, the phase shift was also recorded simultaneously by using the lock-in amplifier as shown in the figure. Upon increasing the light modulation frequency, the phase shift gets increasing and saturates after about 300 Hz. According to the change in the phase shift, the defective term of the voltage Y increases up to 62 Hz, which is a peak point, then looks to decreasing after 62 Hz. However, the influence of the defective term is keep increasing because when the frequency increases, the total photo voltage has been decreased by the fast light modulation, which generates reduced light intensity. Therefore, the voltage Y to the voltage R increases, whereas the voltage X decreases. It means that the dominant photo voltage is attributed to the capacitive term rather than the intrinsic term at a high modulation frequency.

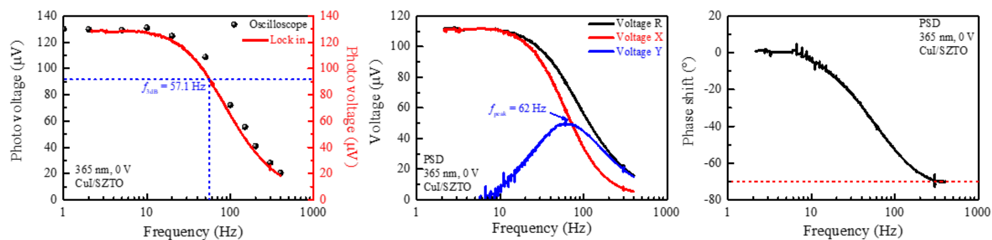

Figure 4.11 (left) A peak-to-peak photo voltage measured by oscilloscope and lock-in amplifier as a function of the light modulation frequency. The measurements were performed at 0 V under 365 nm illumination. The cutoff frequency f_{3dB} bandwidth of the amplitude is estimated as 57.1 Hz as shown in the blue dashed line. (middle) A root-mean-square voltage R, X, and Y values and (right) the phase shift with a variation of frequency in the lock-in amplifier. The red dashed line represents the saturation line of the phase shift.

To further verify the pinhole effect of the photo voltage, a possible reason for the higher cutoff frequency is investigated in terms of the diode current. By summing that the cutoff frequency obeys a simple *RC* circuit, the frequency should be determined by the resistance *R* and the capacitance *C* as described in Equation 4.3.

$$f_{cutoff} = \frac{1}{2\pi RC}$$ **Equation 4.3**

It should be compared to which component is critical to determine the cutoff frequency. The large-area CuI/SZTO photodetector exhibits linear-like *IV* characteristics due to the high leakage current so the capacitance might be a low value due to the high conductivity. Thus, the resistance term is much more contributed to the bandwidth and the resistance is followed Ohm's law.

$$R = \frac{V}{I},\ I(V) = I_s \exp(\frac{eV}{k_B T} - 1)$$ **Equation 4.4**

The leakage current can be described using Schockley-Read-Hall (SRH) (or trap-assisted) recombination process as shown in Equation 4.5.

$$I_s = S_t e n_o \exp(-\frac{eV_{bi}}{k_B T})$$ **Equation 4.5**

$$S_t = \sigma v_{th} N_t$$ **Equation 4.6**

where I is the current, I_s is the reverse saturation current, S_t is the trap recombination velocity, e is the elementary charge, n_o is the electron density in the equilibrium state, V_{bi} is the built-in potential of the *pn* junction, k_B is the Boltzmann constant, T is the absolute temperature, σ is the capture cross-section, v_{th} is the thermal velocity, and N_t is the trap density.

In other words, the total current is proportional to the leakage current, which is determined by the capture cross-section, the trap density, and the built-in potential, followed by the ohm's law. Therefore, the cutoff frequency is inversely proportional to the resistance so that the frequency is proportional to the leakage current. It means that the high leakage current on the CuI/SZTO photodetector gives rise to a possible source of the high bandwidth. The large-size pinholes in the CuI film can act as a recombination center. It is thus likely that the photodetector performance of the CuI/SZTO diode can be further improved when the large-size pinholes are effectively suppressed by the optimal growth conditions or the uniform film.

4.5 The physical origin of the responsivity curve on the CuI/SZTO photodetector

In order to figure out the origin of the responsivity curve on the CuI/SZTO

photodetector, the optical property of each layer was measured using the UV-VIS-NIR spectrometer and ellipsometry method as shown in Figure 4.12.

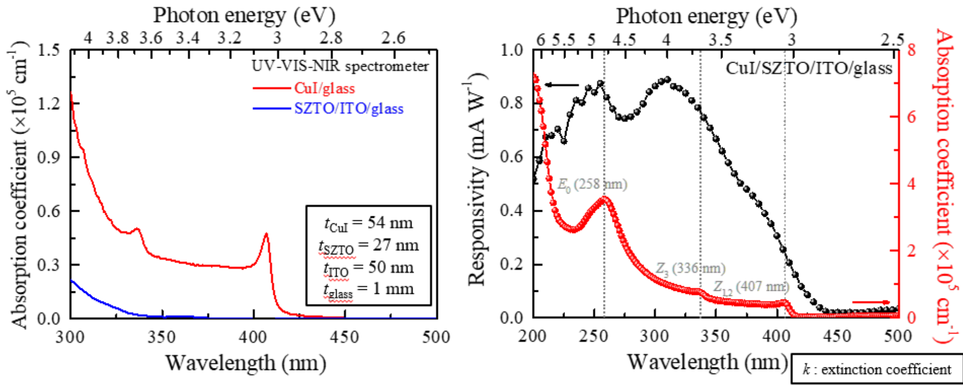

Figure 4.12 (left) The absorption coefficient of CuI/glass and SZTO/ITO/glass. The transmittance and reflectance measurements were conducted using a UV-VIS-NIR spectrometer. The absorption coefficient was calculated by using Equation 4.7. Film thicknesses of each layer are 54 nm, 27 nm, 50 nm, and 1 mm for the CuI, SZTO, ITO, and glass substrate, respectively. (right) Comparison of the responsivity to the absorption coefficient on the CuI/SZTO photodetector. The absorption coefficient is obtained from the measured extinction coefficient by ellipsometry data.

$$\alpha = \frac{1}{t}\ln\left(\frac{(1-R)^2}{T}\right) \qquad \textbf{Equation 4.7}$$

where α is the absorption coefficient, t is the film thickness, R is the reflectance, and T is the transmittance.

To obtain absorption coefficient, transmittance and reflectance measurements on the CuI/glass and the SZTO/ITO/glass were conducted. As we expected, the drastic change at 407 nm was observed due to the CuI excitonic absorption in the CuI film. In comparison to the CuI absorption, the SZTO/ITO/glass shows a slight increase at below 330 nm in the wavelength range of 300 - 500 nm. It is noted that the bandgap energy of each material is 3.1, 3.7, 3.9, and 3.8 eV for the CuI, SZTO, ITO, and glass substrate, respectively [76].

Furthermore, the absorption coefficient of the CuI/SZTO photodetector measured by ellipsometry exhibits consistent behavior with the CuI film. Three peaks appear at 258, 336, and 407 nm, respectively. The main source of the E_0 peak at 258 nm is the indirect interband transition, which occurs at a slightly higher *k*-point than the gamma point. The second and third peaks are known to be the excitonic transition of triplet Z_3, single and doublet $Z_{1,2}$, respectively [29]. However, still, the peak positions from the responsivity and the absorption coefficient look different.

In order to further investigate the origin of the responsivity curve of the CuI/SZTO photodetector, it should be considered the photocurrent flow mechanism first. The photo-generated carriers are formed at the *pn* junction interface because outside the junction interface the photo-carriers are easily recombined and can not contribute to the current flow. Moreover, the photo-carriers can be easily decayed by a few processes during the current flow from the junction interface to the electrodes. Figure 4.8 shows various transitions in a semiconductor, such as interband transition by the excitation in between bandgap, trap-assisted transition by the in-gap trap states, Auger transition, etc.

Interband

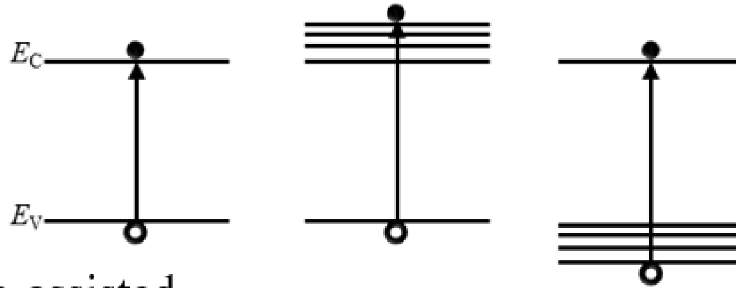

Trap-assisted

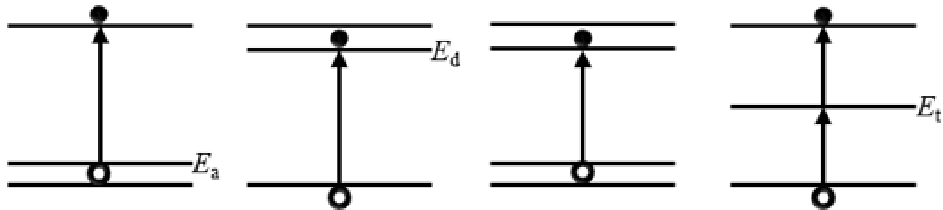

Auger

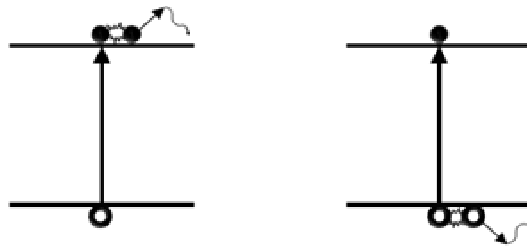

Figure 4.13 Various possible transitions of interband, trap-assisted, and Auger. Here, E_C, E_V, E_d, E_a, and E_t represent the conduction band offset, the valance band offset, the donor level, the acceptor level, and the trap level, respectively.

The minority carrier lifetime of the photo-generated carriers can be described as a followed equation;

$$\tau = \frac{\Delta n}{R(x)}, \quad \frac{1}{\tau_{bulk}} = \frac{1}{\tau_{band}} + \frac{1}{\tau_{defect}} + \frac{1}{\tau_{Auger}} \qquad \textbf{Equation 4.8}$$

where τ is the minority carrier lifetime, $R(x)$ is the recombination rate, and Δn is the excess carrier density.

Therefore, the photocurrent is mainly attributed to the intrinsic transition of the interband transition among various processes. The intrinsic interband transition can estimate by assuming the parabolic band at the gamma point due to the direct bandgap of the CuI. Then, the photocarrier excitation rate is expressed by Equation 4.9.

$$I(v) \propto v^2 \sqrt{hv - E_g} \exp(-\frac{hv - E_g}{k_B T}) \qquad \textbf{Equation 4.9}$$

where I is the excitation rate, hv is the photon energy, E_g is the bandgap energy, k_B is the Boltzmann constant, and T is the absolute temperature.

The calculated excitation rate as a function of wavelength or photon energy is shown in Figure 4.14. Here, the bandgap energy of 3.1 eV was used since a light-absorbing layer should be the CuI film. It is remarkable that the maximum excitation rate is obtained at 310 nm, which is consistent with the measured responsivity curve in Figure 4.14. It is thus likely that the intrinsic explanation for the responsivity curve of the CuI/SZTO photodetector is originated from the main light-absorbing layer of the CuI film.

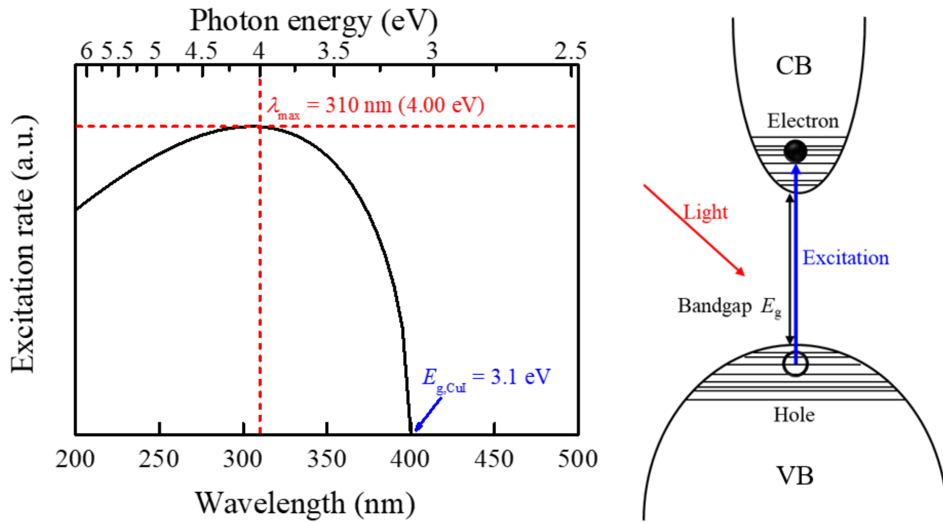

Figure 4.14 Calculated excitation rate by considering the intrinsic inter-band

transition. The CuI is a direct bandgap material, so the CuI band was assumed as a parabolic band at Γ-point.

It is noted that the experimental bandgap energy of the CuI is about 3.1 eV, which is slightly higher than the starting point of the responsivity curve at about 430 nm (2.88 eV). Therefore, there should be the other reason for the higher starting point of the responsivity curve. That can be explained by photoluminescence measurements on the CuI/glass, SZTO/ITO/glass, and CuI/SZTO/ITO/glass. Figure 4.15 shows the PL spectra of each layer under ambient conditions at 320 nm excitation. The SZTO/ITO/glass gives just broad-band background. In the CuI film, the sharp peak at 409 nm was observed overlapping with a shoulder peak at 418 nm. Those peak positions were checked from the peak deconvolution as shown in Figure 4.15. The assigned peak1 at 409 nm and peak2 at 418 nm are attributed to the CuI excitonic absorption and the shallow-level copper vacancy, respectively. The copper vacancy states are often observed in many CuI reports [29], [67]. The shoulder peak of peak 2 started at about 430 nm, which is consistent with the responsivity curve.

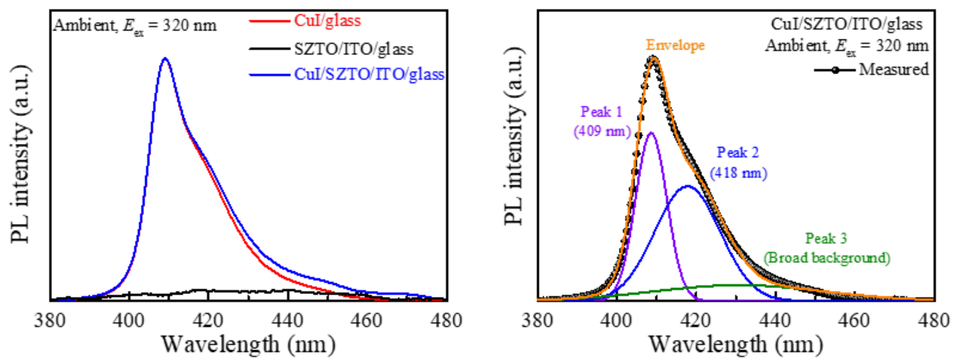

Figure 4.15 (left) PL spectra on the CuI/glass, SZTO/ITO/glass, and CuI/SZTO/ITO/glass. (right) Peak deconvolution result of the CuI/SZTO/ITO/glass PL signal. The envelope function is well-matched with the measured data.

Therefore, based on the experimental observation, the physical origin of the spectral responsivity curve on the CuI/SZTO photodetector is originated from several reasons; the

UV light absorption at the diode interface, interband transition in the CuI film, intrinsic photocarrier excitation rate, recombination and separation of electron-hole pairs, shallow-level V_{Cu} level, exciton absorption, etc.

4.6 Enhancement of the responsivity by reducing pinhole effects on the CuI/SZTO photodetector

In the previous section, we confirmed the critical defect of the large-size pinholes in the CuI film to the photocurrent. It is worthwhile to investigate the photodetector performance on the pinhole-free sample, which has a much small junction area to avoid the large-size pinholes. In order to decrease pinhole effects, we reduced *pn* junction area by about 2500 times from 0.2 cm^2 (= 5 mm × 4 mm) to 7.85 × 10^{-5} cm^2 (= π × 50 μm × 50 μm) in Figure 4.16. After the reduction of the junction area, Ag room temperature epoxy and 10 μm Au wire were used for making stable contact between the probe tip and the sample. On the small CuI/SZTO photodetector, backward illumination from the bottom side was used to shine the light since the lateral junction area is insufficient and the thick Ag epoxy obstructs the incident light.

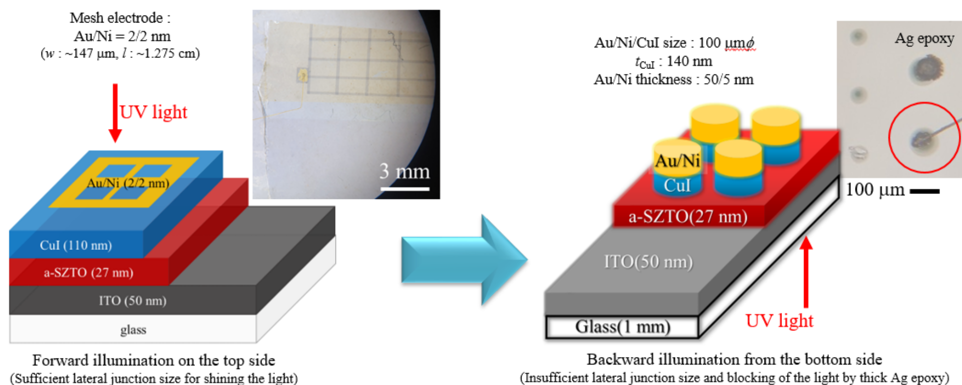

Figure 4.16 Schematic structures and corresponding photographs for the large- and the small-size CuI/SZTO photodetectors. The lateral junction areas are 5 mm × 4 mm and π × (50 μm)^2 for the large-size and the small-size junction, respectively.

The *IV* curve measurements on the small CuI/SZTO photodetector were performed upon varying the light wavelength from 200 to 500 nm. Among those curves, representative *IV* curves under dark, 300 nm, and 350 nm illumination conditions are presented in Figure 4.17.

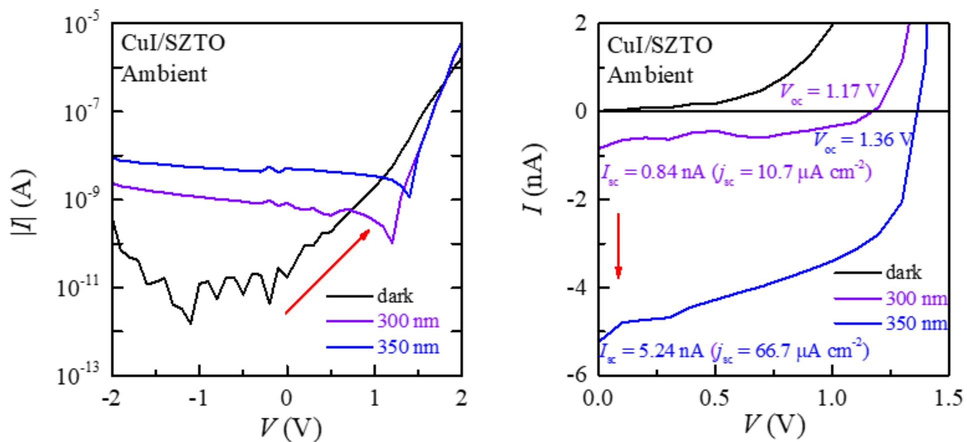

Figure 4.17 Current-voltage (*IV*) curves in a semi-log scale (left) and the enlarged *IV* curves in a linear scale (right) under dark, 300 nm, and 350 nm illumination conditions. The resultant *IV* curves in the semi-log scale under the UV light illumination clearly show the upper-right shift by the photocarrier generation. The I_{sc} and V_{oc} represent short-circuit current and open-circuit voltage, respectively.

When the excess carriers have been generated by the light, the photocurrent can flow and give the shift effect of *IV* curves in the linear scale to the down-side to result in the upper-right shift of *IV* curves in the semi-log scale as shown in the Figure 4.17. In other words, the reduced junction area can effectively avoid pinhole effects. The short-circuit current (I_{sc}) at 0 V and the open-circuit voltage (V_{oc}) at 0 A were estimated as 5.24 nA and 1.36 V at 350 nm, respectively. Those values are comparable to or slightly higher than that

of other CuI-based self-powered UV photodetectors [89].

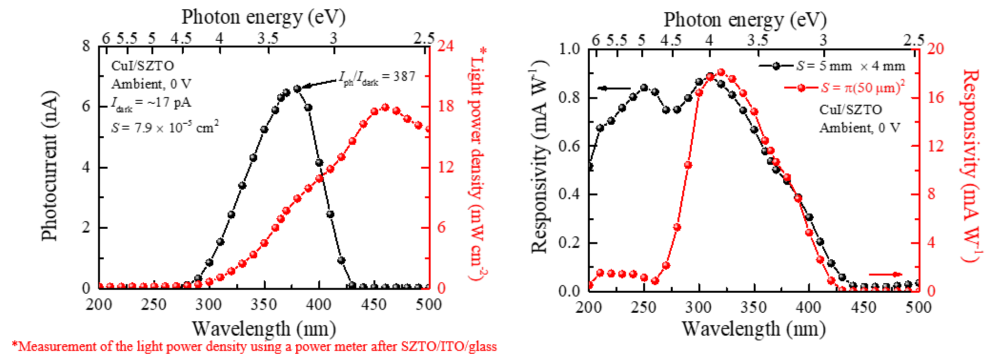

Figure 4.18 (left) Photocurrent and light power density as a function of wavelength. The photocurrent was measured on the CuI/SZTO/ITO/glass structure by the bottom-side light illumination. The light power density was checked after passing through the SZTO/ITO/glass layers using a power meter. (right) Comparison of responsivity curve on the CuI/SZTO photodetectors with different junction areas. The small CuI/SZTO photodetector shows better performance. *S* represents the effective illumination area.

According to the change in the junction area, the photocurrent was measured and represented in Figure 4.18. It looks similar to the previous large-size photodetector, although there is no distinguishable photocurrent because there is no detectable light power density below 280 nm. Here, the light power density was checked after the SZTO/ITO/glass using a power meter, due to the backward illumination. The obtained responsivity curve is compared to the previous responsivity curve of the large-size CuI/SZTO photodetector. The new responsivity on the small photodetector has been enhanced by about 20 times from 0.89 mA W^{-1} to 18.1 mA W^{-1}. There is a difference between the two curves below about 280 nm. It is attributed to the UV light blocking by the glass substrate. The most important point is that the maximum responsivities on the two samples are observed at about 310 nm (4 eV), due to the maximum excitation ratio of the CuI film as described before.

4.7 Various photodetector performances on the improved CuI/SZTO diode

There are various photodetector parameters, such as photocurrent on/off ratio I_{ph}/I_{dark}, linearity, external quantum efficiency (EQE), bandwidth cutoff frequency f_{3dB}, etc. In this section, we investigated the other parameters beyond photocurrent and responsivity. First of all, the photocurrent linearity, being able to be estimated from the power-law fitting, is shown in Figure 4.19.

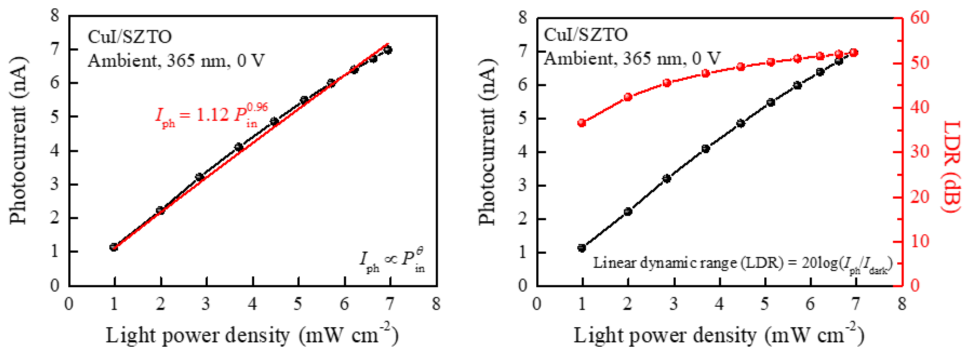

Figure 4.19 (left) The photocurrent with a power-law fitting curve and the linear dynamic range (LDR) as a function of incident light power density. The red solid line without symbols represents the power-law fitting result. The power-law exponent was estimated as 0.96, meaning that the photocurrent is directly proportional to the input light with a slight decrease of the photocurrent due to defects. (right) The LDR refers to the capability of the photocarrier generation of the photodetector. A high LDR value represents that the photodetector can effectively generate photocurrent when the light is illuminated.

In Figure 4.19, the photocurrent increases with the increase of the light power density, meaning that the CuI/SZTO photodetector generates the photocurrent linearly proportional to the incident light. The fitting curve is well-matched with the measured data, though the exponent is slightly lower than one due to probably defect effects. The main decrease

reason for the lower exponent value is probably the presence of point defects, which is confirmed by the PL signal. The typical power-law exponent value is in the range of 0.90 - 1.05, which is consistent results with the CuI/IGZO case [89]. Figure 4.19 shows the photocurrent as well as the linear dynamic range (LDR), which is the effectiveness of the photo current generation of the photodetector, as a function of light power density. The LDR is proportional to the photocurrent on/off ratio (I_{ph}/I_{dark}) as described in Equation 4.10.

$$LDR = 20\log(I_{ph}/I_{dark})$$ **Equation 4.10**

where I_{ph} is the photocurrent, I_{dark} is the dark current.

It is worth noting that the maximum photocurrent on/off current I_{ph}/I_{dark} at 380 nm is 387, which is about 52 dB in the LDR. For the case of the CuI-based self-powered UV photodetector, several reported LDR values are ~80 dB for Au/CuI/TiO_2 at 0 V [38], 77 dB for CuI/IGZO at 0 V [89], ~50 dB for CuI/ZnO at 5 V [96]. The obtained value of 52 dB of the CuI/SZTO photodetector is comparable to or slightly lower than that of others, possibly due to the suppressed photocurrent generation by the reduced area.

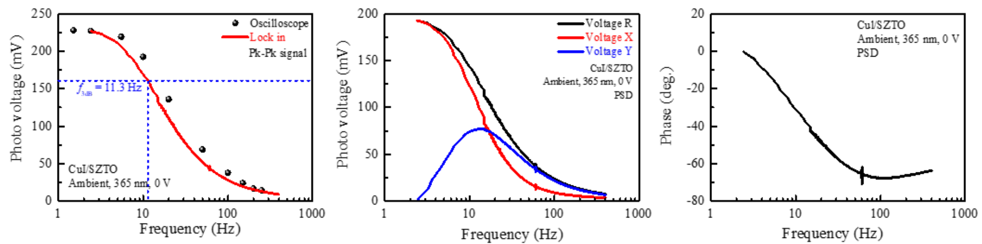

Figure 4.20 (left) Photo voltage as a function of the light modulation frequency measured by two techniques, oscilloscope and lock-in phase-sensitive detection. A root-mean-square voltage R measured by the PSD has been converted to peak-to-peak based on the oscilloscope waveforms. The blue dashed line represents the photodetector cutoff frequency bandwidth. (middle) The measured photovoltages R, X, and Y by lock-in and (right) phase shift upon varying with the light modulation frequency.

Figure 4.20 exhibits frequency-dependent photo voltage measured by the phase-sensitive detection method using a lock-in amplifier as well as an oscilloscope. The results of those two methods are well-matched with each other and the photovoltage decreases with the increase of the light modulation frequency. It is noted that the photo voltage measured by the PSD technique is a converted peak-to-peak value based on the oscilloscope waveforms because the lock-in apparatus measures a root-mean-square value. The measurements have been performed in the frequency range of 2 - 400 Hz on the small-size CuI/SZTO photodetector at 365 nm under ambient conditions without any external bias voltage. In order to maintain the steady-state during the photo voltage measurements using the lock-in apparatus, at least 5 seconds waited at one frequency and then increased the frequency. The cutoff frequency (f_{3dB}), which is defined at 70.7 % of the maximum amplitude point, is estimated as 11.3 Hz, which is a comparable value to the similar CuI/IGZO photodetector. Figure 4.20 represents measured data of voltage R, X, and Y by the lock-in apparatus. Upon increasing the light modulation frequency, as the phase difference is decreased as shown in the figure, the voltage R and the voltage X increase, whereas the voltage Y increases up to about 20 Hz and then starts to decrease. If charged trap states exist in the photodetector, the photo-generated carriers have been captured by the traps, which have a generally slow response time to the modulation frequency. Thus, the increase of the voltage Y ratio to the total voltage R as well as the decrease of the voltage X ratio to the total voltage R represents that the CuI/SZTO photodetector has defects of slow component, mainly copper vacancies in the CuI film.

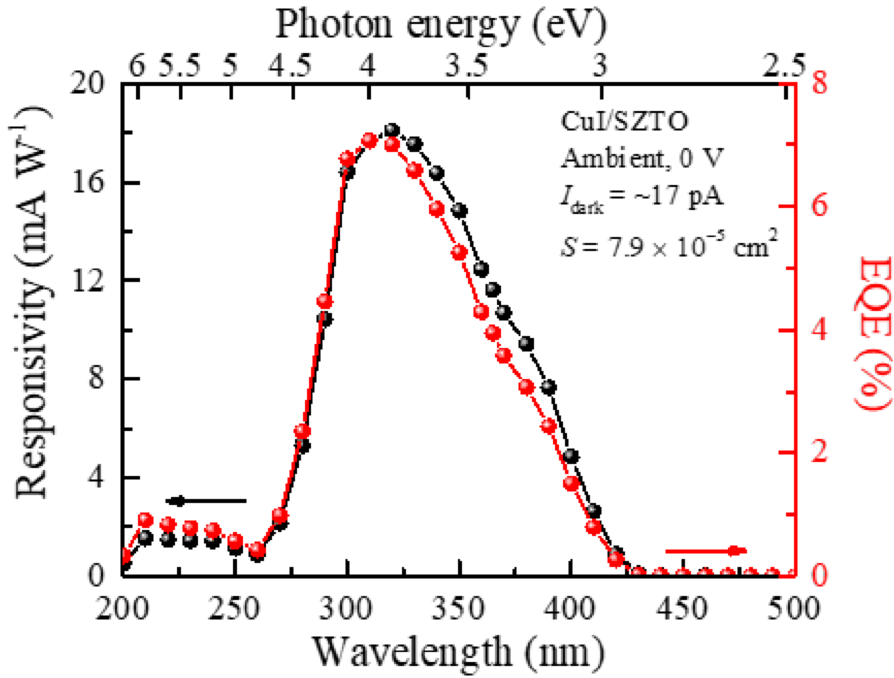

Figure 4.21 Comparison between the responsivity and the external quantum efficiency (EQE) as a function of wavelength. The EQE is obtained in Equation 4.11.

Figure 4.21 shows the responsivity and the EQE on the CuI/SZTO photodetector at 0 V self-powered under ambient conditions. The EQE is defined as the followed equation;

$$EQE = \frac{I_{ph}/e}{P_{in}/h\nu} = R_{\lambda}\frac{hc}{e\lambda} \quad \textbf{Equation 4.11}$$

where I_{ph} is the photocurrent, P_{in} is the incident light power, e is the elementary charge, h is Planck constant, ν is photon frequency, c is the speed of light, λ is the light wavelength, R_{λ} is the responsivity.

The EQE refers to the ratio between output electrons and input photons, meaning that the photocurrent to the incident photon by the photodetector. It is thus likely that the EQE curve follows the responsivity curve upon varying with the wavelength. The maximum

EQE of the CuI/SZTO photodetector at 310 nm is about 7 %, which is a high value among various CuI-based self-powered UV photodetectors. The obtained photodetector parameters are summarized in Table 4.1.

Table 4.1 Summary of various photodetector parameters for CuI-based self-powered UV photodetectors.

CuI-based *pn* diode	I_{sc} (nA)	V_{oc} (V)	Responsivity (mA W^{-1})	EQE (%)	Power law linearity	LDR (dB)	Detectivity (Jones)	NEP (W $Hz^{-1/2}$)	Cutoff frequency (Hz)	Reference
CuI/ TiO_2	-	-	4.5	1.36	-	57.7	1.1×10^{11}	2.3×10^{-12}	-	[97]
CuI/ TiO_2	-	-	0.67	0.32	1.02	~80	8.4×10^{11}	-	-	[38]
CuI/ ZnO	-	-	17.7	6.01	0.91	61.8	5.0×10^{9}	4.0×10^{-11}	-	[95]
CuI/ $CsPbBr_3$	-	-	1.4	0.32	-	63.5	6.2×10^{10}	1.1×10^{-12}	-	[86]
CuI/ β-Ga_2O_3	-	0.71	2.49	1.22	-	-	-	-	-	[87]
CuI/ InGaZnO	330	0.01	0.3	0.10	-	-	-	-	-	[80]
CuI/ InGaZnO	28	0.05	0.6	0.20	1.03	77	-	-	10	[89]
CuI/ SiZnSnO	**6.6**	**1.44**	**18.1**	**7.01**	**0.96**	**52.3**	**6.9×10^{10}**	**1.3×10^{-13}**	**11.3**	**This work**

4.8 Comparison of the high responsivity of the self-powered CuI/SZTO UV photodetector

In this section, we will discuss the various responsivity values of CuI-based self-powered UV photodetector. The responsivity is the most important parameter among various photodetector parameters. It will be thus worthwhile to compare the responsivity of the CuI/SZTO photodetector to the others. Figure 4.22 exhibits a summary of the responsivity values of CuI-based self-powered UV photodetectors made of *pn* junctions.

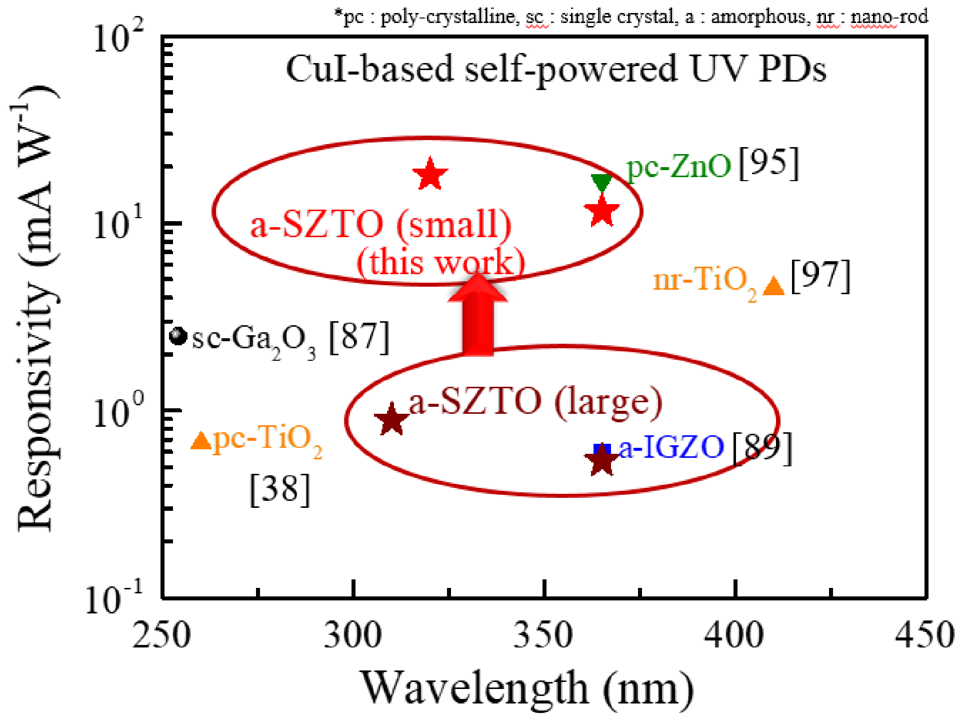

Figure 4.22 Comparison of responsivity on various CuI-based self-powered UV photodetectors. The summarized photodetectors have been made of *p*-CuI and *n*-type various materials in various forms.

Here, the materials in Figure 4.22 represents *n*-type layers to compose the photodetectors. The CuI/SZTO photodetector shows 18.1 mA W^{-1} at 320 nm (11.6 mA W^{-1} at 365 nm), whereas the other photodetectors have 17.7 mA W^{-1} at 365 nm for CuI/ZnO [95], 4.5 mA W^{-1} at 410 nm for CuI/TiO_2 [97], 2.49 mA W^{-1} at 254 nm for CuI/β-Ga_2O_3 [87], 0.6 mA W^{-1} at 365 nm for CuI/IGZO [89]. It is remarkable that the responsivity of the CuI/SZTO photodetector is the highest value among CuI-based self-powered UV photodetectors, consisting of *pn* junction diodes. Another important point of this result is that the CuI/SZTO photodetector has been made of amorphous-based materials, which are the glass substrate, ITO, and SZTO films, indicating that the CuI/SZTO photodetector can fabricate with high performance even on amorphous bottom layers regardless of substrate types. Furthermore, when the junction area is reduced by 2500 times, the responsivity

increase by about 20 times from 0.89 mA W^{-1} to 18.1 mA W^{-1}, implying the possibility of further improvement for the CuI/SZTO photodetector when the CuI film was much homogeneous. The main reason for the increase of the responsivity is the reduced pinhole effect, reducing a high leakage current to result in the decrease of the concealment for the photocurrent, as described in the previous section.

4.9 Summary

In this chapter, we have investigated the photodetector performance on the transparent *p*-CuI/*n*-SiZnSnO (SZTO) heterojunction diodes with a variation in the junction size. In order to study the photocurrent, we have first established the light illumination system, consisting of a Xe arc lamp, a ventilating hood, an optical chopper, a monochromator, a micro probe station, and a semiconductor characterization system. The constructed photocurrent system can generate monochromatic light with variations of wavelength (200 - 1200 nm) and modulation frequency (2 - 400 Hz) and it has been confirmed by power meter and commercial Si PIN photodiode. The large-area CuI/SZTO junction with a lateral area of 10 mm × 4 mm doesn't show the current rectifying behavior, of which a high current level has been observed by the high leakage current. Albeit there exists a high leakage current, which covers the clear photocurrent, the photocurrent nature of the CuI/SZTO photodetector was systematically investigated on the basis of various factors; coherence between responsivity and absorption coefficient, photocarrier excitation rate in the CuI film by the intrinsic interband transition, photoluminescence signal of the CuI/SZTO photodetector, and optical response of the CuI film. Furthermore, the influence of the leakage current was analyzed in the frequency-dependent photovoltage behavior. The presence of large-size non-uniform pinholes has been directly confirmed by the FE-SEM

top-view images with an average grain size of about 51 nm, which is consistent with the XRD results except for the pinhole broadening effects. The enhancement of the photocurrent, followed by the responsivity improvement by reducing the junction area by about 2500 times to avoid undesirable pinhole effects. The high responsivity of 18.1 mA W^{-1} at zero bias (0 V) on the small-size CuI/SZTO photodetector was compared to the various CuI-based self-powered UV photodetectors. The present CuI/SZTO photodetector exhibits a noticeable responsivity regardless of substrate types, indicating that the CuI film maintains its versatile physical properties even on amorphous bottom layers. Furthermore, the room-temperature growth of the CuI film is desirable to study flexible devices by preventing unexpected thermal effects, because thermodynamical (or chemical) reactions happen in high-temperature growth or thermal annealing at high temperatures. Therefore, once the pinhole effect has been further reduced, the self-powered CuI/SZTO UV photodetector will be much improved as an essential component in potential optoelectronic applications.

References

[1] D. S. Ginley and C. Bright, MRS Bull. **25,** 15 (2000)

[2] X. Yu *et al*., Nat. Mater. **15,** 383 (2016)

[3] R. C. Hoffmann *et al*., J. Mater. Chem. C **1,** 2577 (2013)

[4] H. Hosono *et al*., J. Cryst. Growth **237,** 496 (2002)

[5] S. Calnan, and A. N. Tiwari, Thin Solid Films **518,** 1839 (2010)

[6] H. He *et al*., Phys. Rev. B **74**, 195123 (2006)

[7] J. Son *et al*., Nat. Mater. **9**, 482 (2010)

[8] S. Ohta *et al*., J. Appl. Phys. **97**, 034106 (2005)

[9] L. F. Mattheiss *et al*., Phys. Rev. B **37**, 3745 (1988)

[10] R. J. Cava *et al*., Natrue **332**, 814 (1988)

[11] Y. Tokura and Y. Tomioka, J. Magn. Magn. Mater. **200**, 1 (1999)

[12] W.-J. Lee *et al*., Annu. Rev. Mater. Res. **47**, 391 (2017)

[13] G. H. Haertling J. Am. Ceram. Soc. **82**, 797 (1999)

[14] S. Mathews *et al*., Science **276**, 238 (1997)

[15] J. Wang *et al*., Science **299**, 1719 (2003)

[16] S. H. Wemple, Rhys. Rev. A **137**, 1575 (1965)

[17] A. Ohtomo and H. Y. Hwang, Appl. Phys. Lett. **84**, 1716 (2004)

[18] R. D. Shannon, Acta Crystallogr. A **32**, 751 (1976)

[19] E. H. Mountstevens *et al*., J. Phys.: Condens. Matter **15**, 8315 (2003)

[20] W. Zhang *et al*., J. Mater. Res. **22**, 1859 (2007)

[21] H. Mizoguchi *et al*., Inorg. Chem. **43**, 1667 (2004)

[22] H. J. Kim *et al*., Phys. Rev. B **86**, 165205 (2012)

[23] D. J. Singh *et al*., Phys. Rev. B **44**, 9519 (1991)

[24] H. F. Wang *et al*., J. Appl. Phys. **101**, 106105 (2007)

[25] B. Jadjarab *et al.*, J. Phys. D: Appl. Phys. **40**, 5833 (2007)

[26] H. J. Kim *et. al.*, Appl. Phys. Express **5** 061102 (2012)

[27] W.-J. Lee *et al.*, Phys. Status Solidi A **212** 1487 (2015)

[28] K. Baedeker, Ann. Phys. **327**, 749 (1907)

[29] M. Grundmann *et al.*, Phys. Status Solidi A **210**, 1671 (2013)

[30] J. Wang *et al.*, J. Appl. Phys. **110**, 054907 (2011)

[31] D. Chen *et al.*., Crys. Growth Des. **10**, 2057 (2010)

[32] P. Dordor *et al.*, J. Solid State Chem. **75**, 105 (1988)

[33] J. Tate *et al.*, Phys. Rev. B **80**, 165206 (2009)

[34] N. Yamada *et al.*, Chem. Mater. **28**, 4971 (2016)

[35] H. J. Lee *et al.*, ACS Appl. Mater. Interfaces **11**, 40243 (2019)

[36] S. Das *et al.*, Sol. Energy Mater. Sol. Cells **133**, 255 (2015)

[37] S.-D. Baek *et al.*, ACS Appl. Mater. Interfaces **12**, 6037 (2020)

[38] C. Zuo *et al.*, Nanotechnology **33**, 105202 (2022)

[39] H. Sato *et al.*, Thin Solid Films **236**, 27 (1993)

[40] T. Tanaka *et al.*, Thin Solid Films **281**, 179 (1996)

[41] H. Kawazoe *et al.*, Nature **389**, 939 (1997)

[42] N. Duan *et al.*, Appl. Phys. Lett. **77**, 1325 (2000)

[43] R. Nagarajan *et al.*, J. Appl. Phys. **89**, 8022 (2001)

[44] P. M. Sirimanne *et al.*, Chem. Phys. Lett. **366**, 485 (2002)

[45] H. Hiramatsu *et al.*, Thin Solid Films **411**, 125 (2002)

[46] M. Dekkers *et al.*, Appl. Phys. Lett. **90**, 021903 (2007)

[47] M. Snure and A. Tiwari, Appl. Phys. Lett. **91**, 092123 (2007)

[48] E. Fortunato *et al.*, Appl. Phys. Lett. **97**, 052105 (2010)

[49] F. L. Schein *et al.*, Appl. Phys. Lett. **102**, 092109 (2013)

[50] M. Aksit *et al.*, Appl. Phys. Lett. **104**, 161901 (2014)

[51] S. Wang *et al*., Opt. Mater. Express **4**, 10 (2014)

[52] R. Wei *et al*., Chem. Commun. **50**, 9697 (2014)

[53] K. H. L. Zhang *et al*., Adv. Mater. **27**, 5191 (2015)

[54] L. Farrell *et al*., Appl. Phys. Lett. **107**, 031901 (2015)

[55] C. Yang *et al*., Proc. Natl. Acad. Sci. **113**, 46 (2016)

[56] L. Sun *et al*., J. Mater. Sci. **51**, 1302 (2016)

[57] J. Crepelliere *et al*., J. Mater. Chem. C **4**, 4278 (2016)

[58] J. H. Lee *et al*., J. Phys.: Condens. Matter **29**, 384004 (2017)

[59] L. Hu *et al*., Adv. Electron. Mater. **4**, 1700476 (2018)

[60] D. C. Yuan *et al*., Sci. China-Phys. Mech. Astron. **61**, 10 (2018)

[61] R. Wei *et al*., Appl. Phys. Lett. **112**, 251109 (2018)

[62] A. Annadi *et al*., ACS Appl. Electron. Mater. **1**, 1029 (2019)

[63] M. Zi *et al*., Phys. Status Solidi A **212**, 1466 (2015)

[64] C. Yang *et al*., Sci. Rep. **6**, 21937 (2016)

[65] D. Kim *et al*., Phys. Rev. B **60**, 13879 (1999)

[66] W. Li and E. W. Shi, Cryst. Res. Technol. **37**, 1041 (2002)

[67] G. Lin *et al*., Materials **9**, 990 (2016)

[68] J. N. Plendl *et al*., Appl. Opt. **5**, 397 (1966)

[69] P. Singh *et al*., Japn. J. Appl. Phys. **47**, 3540 (2008)

[70] D. Seo *et al*., Appl. Phys. Lett. **104**, 022102 (2014)

[71] H. M. Kim *et al*., APL Mater. **4**, 056105 (2016)

[72] B. C. Luo *et al*., Phys. Status Solidi RRL **11**, 1700279 (2017)

[73] J. Zhang *et al*., Appl. Phys. Lett. **112**, 171605 (2018)

[74] B. C. Luo *et al*., Phys. Status Solidi A **3**, 705 (2014)

[75] B. H. Lee *et al*., Sci. Rep. **9**, 886 (2019)

[76] B. H. Lee *et al*., Sci. Rep. **9**, 19246 (2019)

[77] W. M. Haynes, D. R. Lide, and T. J. Bruno, *CRC handbook of Chemistry and Physics: A Ready-Reference Book of Chemistry and Physical Data*, 95th ed., CRC Press LLC: Boca Raton, FL, USA, 2014; pp. 65-70

[78] K. Nomura *et al*., Nature **432**, 488 (2004)

[79] A. N. Gruzintsev and W. N. Zagorodnev, Semiconductors **46**, 35 (2012)

[80] N. Yamada *et al*., Phys. Status Solidi A **216**, 1700782 (2018)

[81] N. Yamada *et al*., Adv. Funct. Mater. **30**, 2003096 (2020)

[82] T. Sauder *et al*., Solid State Commun. **51**, 323 (1984)

[83] B. H. Lee *et al*., Phys. B Condensed Matter **574**, 311629 (2019)

[84] E. Chong *et al*., Thin Solid Films **534**, 609 (2013)

[85] C. Moditswe *et al*., Ceram. Int. **43**, 5121 (2017)

[86] Y. Zhang *et al*., J. Phys. Chem. Lett. **10**, 2400 (2019)

[87] M. E. Ayhan *et al*., Mater. Lett. **262**, 127074 (2020)

[88] J. H. Lee *et al*., Nanomaterials **11**, 1237 (2021)

[89] N. Yamada *et al*., Appl. Mater. Today **15**, 153 (2019)

[90] K. Lee *et al*., J. Appl. Phys. **112**, 033713 (2012)

[91] T. Liu *et al*., Int. J. Photoenergy **2013**, 765938 (2013)

[92] S. L. Chuang, *Physics of Optoelectronic Devices*; Wiley: New York, NY, USA, 1995; pp. 21-80

[93] C. I. Yu *et al*., P. Phys. Soc. Jpn. **34**, 693 (1973)

[94] K. Jeon *et al*., Thin Solid Films **660**, 613 (2018)

[95] F. Cao *et al*., J. Alloys. Compd. **859**, 158383 (2021)

[96] S. Li *et al*., Adv. Mater. Interfaces **6**, 1900669 (2019)

[97] Z. Zhou *et al*., Opt. Mater. Express **12**, 2 (2022)

Appendix A Attempt to develop the membrane transferring technique for oxide free-standing films

A.1 Overview

Last several years, demands for oxide membrane research have been rapidly emerging to facilitate versatile properties of oxide materials to flexible devices, such as wearable devices, sensors, energy harvesting devices, etc [1]. Such membrane technique is an ideal platform for removing films from substrates using a chemical lift-off process for overcoming quite specific growth conditions of perovskite oxide semiconductors, e.g. a high growth temperature over 800 °C, an epitaxial crystallinity, and a limited substrate. Furthermore, the membrane technique gives rise to a chance to maintain high crystallinity without loss of own film properties. Therefore, the membrane method is worth establishing as an appropriate approach to expanding various perovskite oxide films, particularly the La-doped $BaSnO_3$ (LBSO) film. A common approach to employing the oxide membrane technique is the introduction of a sacrificial layer, which is a material easily removed by the selective etchant, remaining the crystalline thin film as a free-standing film. This selective etching is usually used by strong acids to release the film from the substrate and requires careful choice of a sacrificial layer. Thus, many researchers have tried to find out a proper material as a sacrificial layer for an oxide film. In 2016, H. Y. Hwang's group at Stanford University finally found the material $Sr_3Al_2O_6$ (SAO) as an epitaxial template for perovskite oxides of $SrTiO_3$ (STO) and $La_{0.7}Sr_{0.3}MnO_3$ (LSMO) [2]. The SAO is a hygroscopic material, having a pseudocubic structure $Pa\bar{3}$ with a lattice constant of 15.844

Å, which is close to 4 times the lattice constant of the conventional perovskite material STO (3.905 Å). What is the most important thing is that the SAO is water-soluble and selectively removed the remaining perovskite oxide film because perovskite oxide materials are often resistive to the water and reactive to acids.

In addition, to develop the SAO as a sacrificial material for the STO and the LSMO, they searched for another sacrificial layer for large lattice-mismatched materials, including $BaSnO_3$ (BSO) [3]. The BSO has a lattice constant of 4.116 Å that is hard to employ the SAO sacrificial layer due to a large lattice misfit of about 5 %. Such a large lattice mismatch induces lots of strain in the film resulting in the many cracks of the free-standing film after the release process. In this situation, a lattice-matched sacrificial material should be studied to reduce the strain effect in the free-standing film. $Ba_3Al_2O_6$ (BAO) has been adopted as a sacrificial material for the BSO membrane because the BAO is also a water-soluble material and has a similar lattice constate of 16.498 Å with the BSO (4.116 Å) [4]. The lattice misfit between the BAO and the BSO is just 0.21 %, being able to grow the almost strain-free BSO film.

In order to extend the optoelectronic applications of the *p*-CuI/*n*-BSO heterojunction diode or BSO-based *pn* junctions, we have tried to make a progress of the way that can apply the BSO-based *pn* junction to flexible devices. Once the CuI/BSO or BSO-based *pn* junctions are utilized, various superior properties of BSO and LBSO will be further realized as practical devices. In this sense, the oxide membrane technique is one candidate for the capability of BSO-based flexible devices. Following the recent stem, we have investigated the sacrificial materials and the oxide membrane technique for the fabrication of the BSO free-standing film. In this appendix material, we introduce how the oxide membrane platform has been established and the preliminary characteristics of the BSO free-standing film as a part of oxide membrane research.

A.2 Experimentals

Polycrystalline BAO target for the PLD deposition was synthesized by solid-state reaction method, using a stoichiometric mixture of high-purity (~99%) $BaCO_3$ and Al_2O_3 powders. The mixture was first calcined at 1200 °C for 5 hrs and finally sintered at 1400 °C for 10 hrs after several intermediate grindings. The BAO film was grown on the STO substrate by PLD at 850 °C in oxygen partial pressure of 0.1 mTorr at a laser fluence of 1.5 J cm^{-2} with a repeat rate of 10 Hz, followed by the *in-situ* $Ba_{0.96}La_{0.04}SnO_3$ (BLSO) deposition at 850 °C in oxygen partial pressure of 100 mTorr at a laser fluence of 0.4 J cm^{-2} with a repeat rate of 10 Hz. To make the BLSO as a free-standing film, the schematic procedure of the membrane-making sequence is shown in Figure A.1. The polydimethylsiloxane (PDMS) and the polypropylene carbonate (PPC) polymers were used as polymer support during the release sequence. A commercial PDMS toolkit (Sylgard 184, Sigma-Aldrich) was used to develop the PDMS polymer. PPC pelltes (Sigma-Aldrich) were dissolved in choloform (99.5 %, Daejung) as a solvent. PPC thin layer was grown on PDMS by spin-coating at 4000 rpm for 35 seconds, followed by the baking sequence on the hotplate at 60 °C for 10 minutes under ambient conditions. The prepared BLSO/BAO/STO by the PLD is placed on top of PPC/PDMS polymers by putting the films up, meaning that the BLSO film and the PPC layer face each other. The sacrificial layer of the BAO film between the STO substrate and the BLSO film has been hydrolyzed by water for 24 hrs at room temperature without any vibration. After the release of the BLSO film from the STO substrate, the STO substrate is carefully detached using double-sided tape on a glass base. The obtained oxide membrane maintains the film as a free-standing form on the polymer supports as shown in the figure.

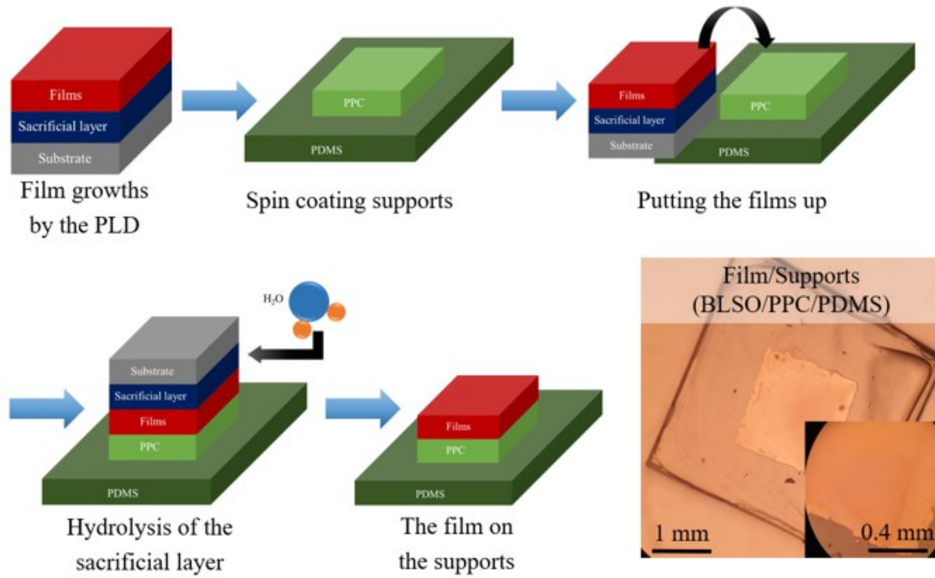

Figure A.1 Schematic procedure of oxide membrane making process and an actual photograph of the obtained free-standing BLSO film on the PPC/PDMS polymer supports.

It is noted that the BSO is a highly hygroscopic material so the target collapses after about 1 month. In order to reconstruct the target, we tried to find optimum conditions for reshaping the target form. Figure A.2 shows the broken BAO target to the powder form and the reconstructed target attached to the PLD target holder.

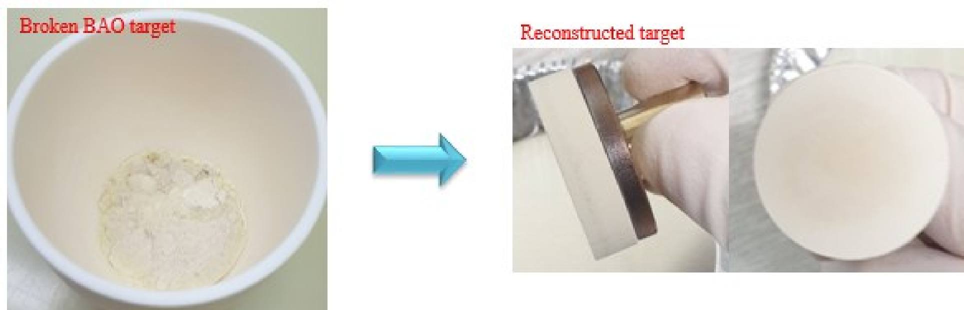

Figure A.2 The BAO target before (left) and after (right) the reconstruction process.

The BAO target easily absorbs water, swells, and eventually loses pellet form and breaks into powder. The broken BAO powder was sonicated with acetone in a beaker for 15

minutes to remove the Ag paste, which is used to attach the target to the holder. Subsequencially, obtained powder has been filtered using filter paper with a micro pore of 5 - 8 μm, followed by the acetone dry for 5 minutes at room temperature. In order to certainly get rid of the remnant Ag paste, steps 1 - 3 were repeated one more. The cleaned BAO powder was baked at 1100 °C for 24 hrs in ambient conditions to evaporate organic compounds in the powder. The baking powder was ground for a short time and pelletized. After the annealing at 1100 °C for 24 hrs was performed, finally the reconstructed BAO target can be obtained as shown in Figure A.2. According to the above procedure, the BAO target was successfully reshaped with a clean white crack-free surface, which is consistent with the previous target. It is thus likely that the hygroscopic BSO target can be repeatedly used without a new target making whenever the BAO deposition.

A.3 Results and discussions

In order to investigate the fundamental physical properties of the oxide membrane, XRD θ- 2θ scans were conducted first in Figure A.3. The BLSO free-standing film exhibits the (002) peak only without any additional peak from the STO substrate of the BAO remnant film. It confirms that the epitaxial BLSO film was successfully transferred by the above transferring procedure because the BLSO film shows an epitaxial nature on the BAO/STO (not shown).

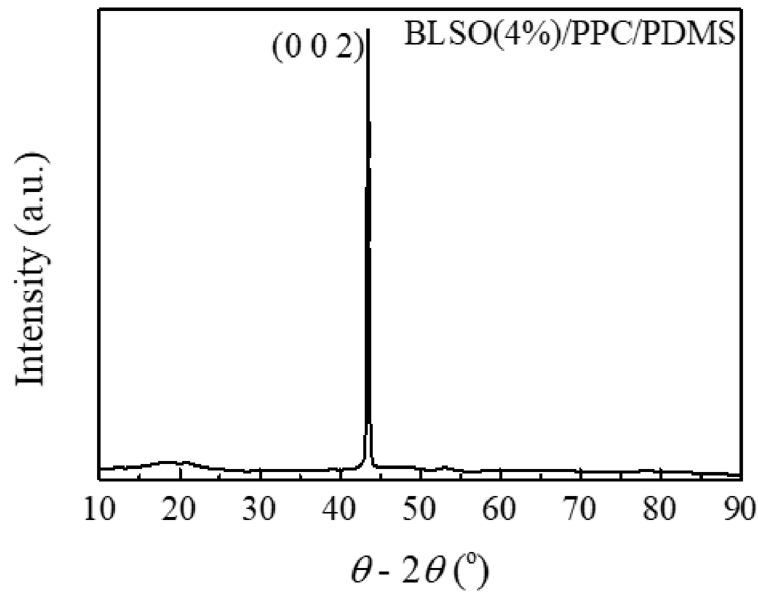

Figure A.3 XRD θ - 2θ scan results of BLSO free-standing film on the PPC/PDMS polymer support after the release process.

To further study the electrical property of the BLSO free-standing film, the Hall effect measurements were performed in the Van der Pauw method using the metallic Au/Ti(50/5 nm) electrode-deposited specimen in Figure A.4. Because membranes are often rather brittle, in order to avoid the damage to the free-standing film during pressing the probe tip, the probe tips were connected to the additional contact pads grown on the rigid glass substrate. However, although we have tried to careful contact as much as possible, a lot of cracks were formed to result in high resistance by disconnecting the electrodes.

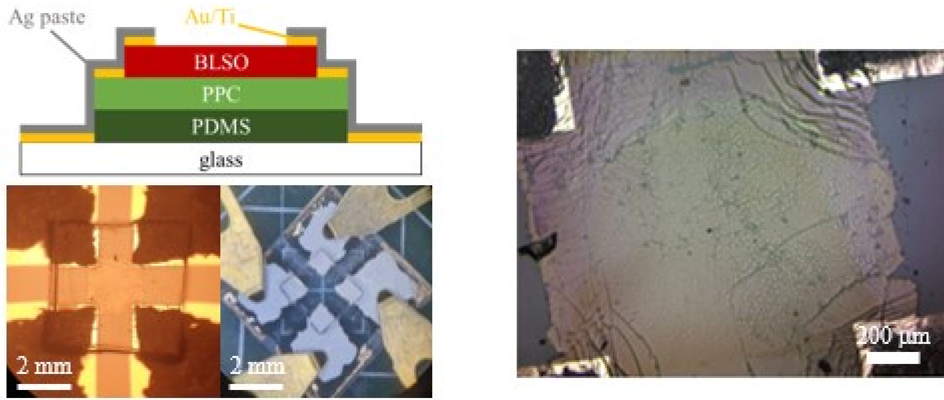

Figure A.4 (left) A schematic structure and actual photographs of the BLSO free-standing film for electrical measurements. (right) A microscope image, which has lots of cracks in the film, after the Hall effect measurements. The scale bar represents a 200 μm length.

It is worth noting that the BLSO film on the BAO/STO substrate before removing the sacrificial layer of the BAO film shows comparable electrical properties with the BLSO film on the STO substrate in Figure A.5. The Hall effect results of rigid BLSO films refer to the electrical property of the BLSO film itself maintains if there are no cracks in the film.

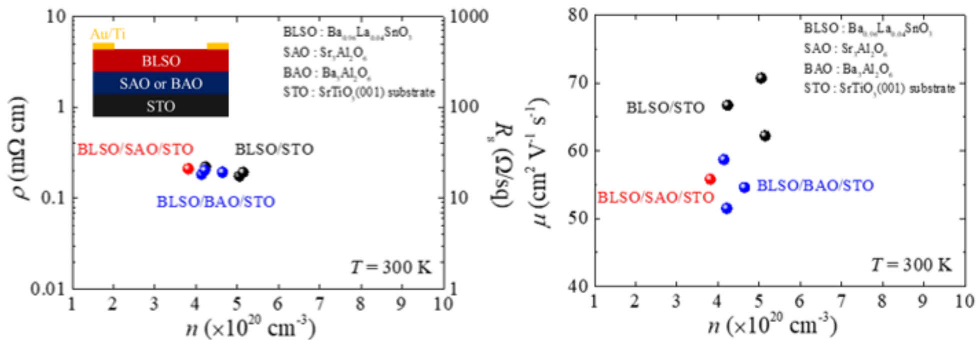

Figure A.5 Electrical resistivity (ρ), sheet resistance (R_s), and electron mobility (μ) of BLSO films on SAO/STO, BAO/STO, and STO substrates as a function of electron carrier density (n). The inset presents a schematic structure of the rigid BLSO sample.

There exists that the BLSO free-standing film shows almost the same mobility as the rigid BLSO film grown on the STO substrate [3]. However, the measured free-standing

film has a quite limited size of 60 nm to facilitate the film as a device application. In order to obtain the relatively large-scale BLSO free-standing films, an additional stabilization process should be needed further. As a stabilization effort, we made a lab-made membrane transferring manipulator, consisting of *xyz* micro positioner, aluminum support, sponge, slide glass, and balance weight in Figure A.6. By using the transferring manipulator, the detachment of the STO substrate can be controlled much more precisely.

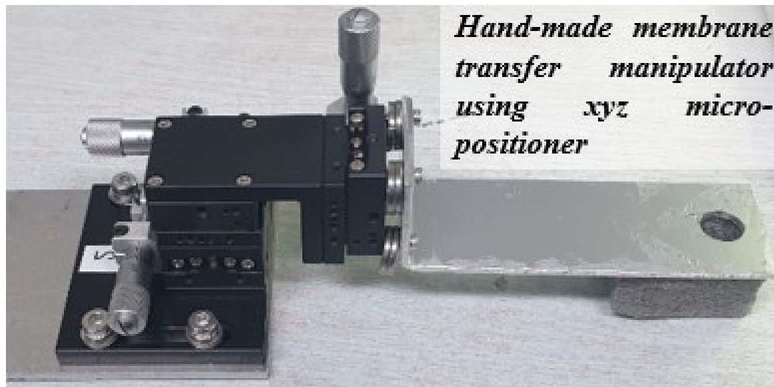

Figure A.6 Photograph of hand-made membrane transferring manipulator attached to the *xyz* micro positioner.

Another effort to reduce the cracks in the BLSO free-standing film is an adoption of a capping layer on top of the BLSO film to enhance the stability of mechanical stresses. Furthermore, once a mechanical strain of a film can be adjustable by a capping layer with suitable conditions, the free-standing film can be much more resistive to the mechanical stress during the transferring process [5]. The capping layer holds the strain and extents it from the film/substrate interface to the film surface to result in the interruption of in-plane stress in a wide range.

To employ the capping approach, the $BaZrO_3$ (BZO) dielectric material has been selected as a capping layer because the BZO has a similar lattice constant of 4.19 Å to the BSO (4.116 Å) [6]. The lattice misfit between the BZO and the BSO is about 1.7 %, being

able to induce a stain effect in the BLSO free-standing film. In addition, thicker films generally endure bending or stretching of films. For growing the BZO capping film, a polycrystalline BZO was synthesized using a stoichiometric solid-state-reaction method with high-purity BaO and ZrO_2 powders. The mixture was sintered at 1650 °C for 24 hrs in the air with intermediate grindings. The BZO film was grown *in-situ* on top of BLSO/BAO/STO by PLD at 850 °C in oxygen partial pressure of 100 mTorr at a laser fluence of 0.4 J cm^{-2} with a repeat rate of 10 Hz. The obtained films were measured by AFM to confirm the thickness per laser shot in Figure A.7. It confirms that one layer of BZO film requires 57 shots by PLD.

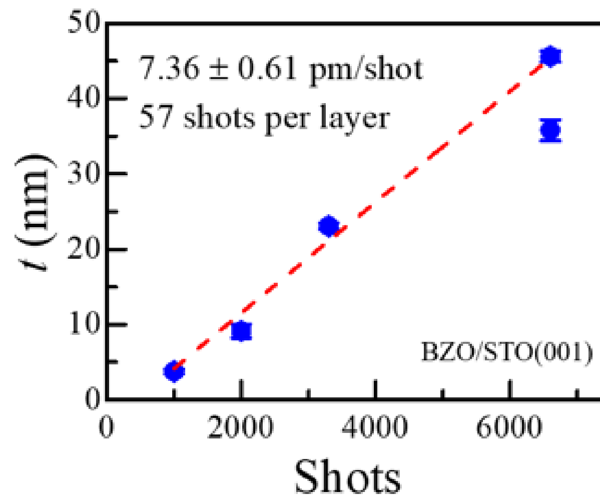

Figure A.7 Film thicknesses of the BZO film as a function of laser shots. The pulse shot was calibrated using the AFM apparatus. It confirms that one layer of BZO film requires 57 shots by PLD.

To investigate the crystallinity of the BZO film on the STO substrate, XRD θ - 2θ and ω scans were conducted in Figure A.8. Except for the STO substrate peaks, only (002) peak of BZO appears in the θ - 2θ scan results and a narrow FWHM value was obtained in the ω scan rocking curve. Therefore, the BZO film can be precisely controlled the thickness with high film quality.

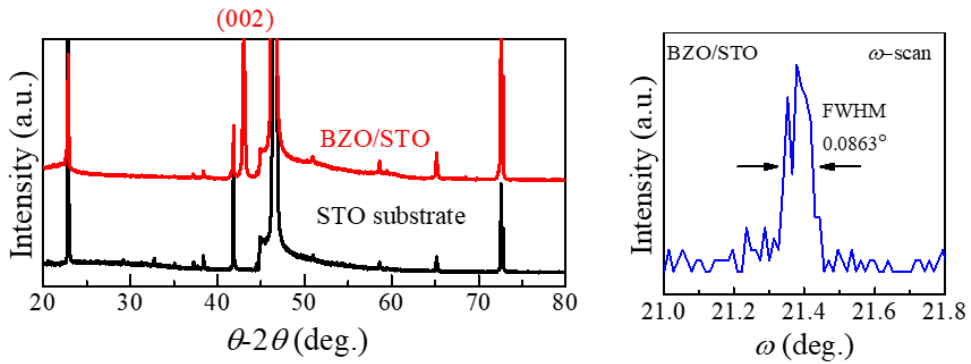

Figure A.8 XRD θ - 2θ and ω scan results of the BZO film on the STO subsrtate. The BZO film exhibits an epitaxial growth feature on the STO substrate with a narrow FWHM value in the rocking curve.

The BLSO free-standing film with the BZO capping layer has been made following the membrane-making procedure as described above. The schematic structure of the BZO-capped BLSO free-standing film on the PPC/PDMS polymer supports is shown in Figure A.9. However, a homogeneous and clean film is not obtained in the actual photograph, presumably due to the inadequate transferring conditions or the thickness control. These results are preliminary and still have a lot of supplement points. It is highly likely that the BLSO free-standing film can be a useful and efficacious platform to realize perovskite oxide-based flexible devices in the near future.

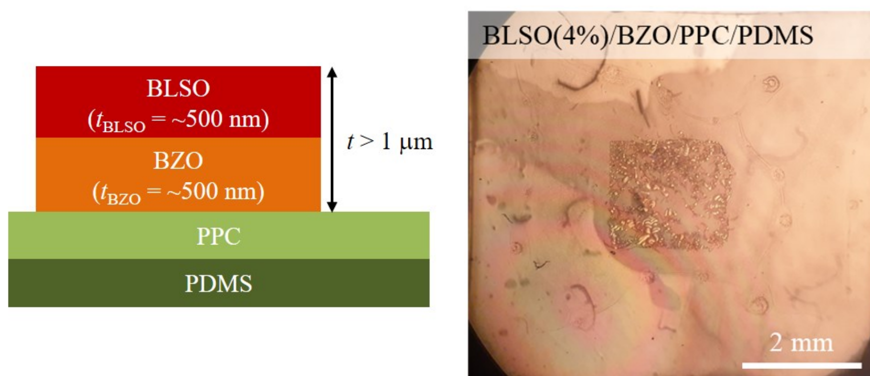

Figure A.9 Schematic structure and actual photograph of the BLSO free-standing film with the BZO capping layer on the PPC/PDMS polymer supports.

A.4 Summary

In this appendix material, we provide the oxide membrane results, especially for the BLSO free-standing film to facilitate the BSO-based pn junctions to flexible devices. To realize the BSO oxide membrane, a hygroscopic material BAO was used as a sacrificial layer between the BLSO film and the STO substrate. The epitaxial BAO film was grown on the STO substrate by the PLD method. To release the BLSO film from the STO substrate, PPC-coated PDMS polymer materials were used to support the free-standing film stably grown by the spin-coating technique. Membrane making procedure was provided with the experimental results of the successful BLSO free-standing film on top of PPC/PDMS polymer supports. The present BLSO free-standing film exhibits crack-free features with a relatively large area without conducting a lithography technique to obtain the clean membrane. In order to investiage fundamental physical properties, optimized transferring conditions from the membrane to the rigid substrate are still further studied using the transferring manipulator made of the *xyz* micro positioner and applying the BZO dielectric material as a capping layer to a thicker film. Once optimized transferring conditions, the BLSO free-standing film gives rise to an ideal platform of various perovskite oxides for many next-generation optoelectronic applications, such as wearable or bendable devices.

A.5 References

[1] A. Tsukazaki, Nature **578**, 41 (2020)

[2] D. Lu *et al.*, Nat. Mater. **15**, 1255 (2016)

[3] P. Singh *et al*., ACS Appl. Electron. Mater. **1**, 1269 (2019)

[4] B. Lazic *et al*., Solid State Sci. **11**, 77 (2009)

[5] H. S. Kum *et al*., Nature **578**, 75 (2020)

[6] D. Gim, …, J. H. Lee *et al*., Materials **15**, 4286 (2022)

List of publications

1. W.-J. Lee, H. J. Kim, J. Kang, D. H. Jang, T. H. Kim, **J. H. Lee**, and K. H. Kim "*Transparent perovskite barium stannate with high electron mobility and thermal stability*" Ann. Rev. Mater. Res. **47**, 391 (2017)

2. **J. H. Lee**, W.-J. Lee, T. H. Kim, T. Lee, S. Hong, and K. H. Kim "*transparent p-CuI/n-*$BaSnO_{3-\delta}$ *heterojunctions with a high rectification ratio*" J. Phys.: Condens. Matter **29**, 384004 (2017)

3. **J. H. Lee**, B. H. Lee, J. Kang, M. Diware, K. Jeon, C. Jeong, S. Y. Lee, and K. H. Kim "*Characteristics and Electronic Band Alignment of a Transparent p-CuI/n-SiZnSnO Heterojunction diode with a High Rectification Ratio*" Nanomaterials **11**, 1237 (2021)

4. J. Kang, **J. H. Lee**, H.-K.Lee, K.-T. Kim, and K. H. Kim "*Effect of Threading Dislocations on the Electronic Structure of La-doped* $BaSnO_3$ *Thin Films*" Materials **15**, 2417 (2022)

5. **J. H. Lee**, B. H. Lee, M. Diware, J. Kang, S. Y. Lee, and K. H. Kim "*Investigation of a self-powered UV photodetector based on the transparent p-CuI/n-SiZnSnO heterojunction diode*" in preparation.

6. D. Gim, Y. Sur, Y. H. Lee, **J. H. Lee**, S. Moon, Y. S. Oh, and K. H. Kim "*Pressure-dependent structure of $BaZrO_3$ crystals as determined by Raman Spectroscopy*" Materials **15**, 4286 (2022)

국문 초록

지난 수십년동안 투명 전도성 산화물 및 투명 산화물 반도체를 포함하는 투명 전도성 물질들은 현대적 광전소자를 이용한 응용 소자로 활용하기 위하여 점점 더 중요한 물질로 대두되고 있다. 특히, ZnO, In_2O_3, TiO_2, 그리고 SnO_2 등과 같은 두가지 성분으로 이루어진 산화물 물질들의 경우 필드-이펙트 트랜지스터 (FET), 발광 다이오드 (LED), 그리고 태양전지 응용 등에 활발하게 이용되고 있다. 그러나, 이러한 잘 알려진 물질들도 여전히 고온에서의 열적 안정성 및 상온에서의 낮은 전기적 이동도 등의 문제들에 한계가 있다. 이러한 상황에서 약 10여 년 전, 우리는 새로운 TCO 시스템을 발견했다. 이는 도너가 도핑된 $BaSnO_3$ (BSO) 시스템으로 입방 페로브스카이트 구조를 가지고 넓은 밴드갭 에너지 (약 3.0 eV)를 가지며, 상온에서 전자 농도가 약 10^{20} cm^{-3} 정도일 때 전자 이동도가 최대 320 cm^2 V^{-1} s^{-1} 정도로 산화물 페로브스카이트 물질 중에서 가장 높은 값을 보임을 발견하고, 이에 대한 고온 열 안정성, 높은 전자 농도 및 전자 이동도에 대한 물리적 근원을 밝혀 보고한 바 있다.

BSO 시스템의 우수한 물리적 특성을 이용하기 위하여 우리는 특히 La 을 도너로 도핑한 BSO (LBSO) 박막에 대하여 연구하였고, 박막 증착을 위하여 페로브스카이트 산화물 기판인 $SrTiO_3$(001) (STO) 기판 위에 펄스 레이져 증착법을 이용하였다. 증착된 LBSO 박막의 경우 상온에서의 전자 이동도가 약 70 cm^2 V^{-1} s^{-1} 정도로 높은 값을 보였고, 이 값은 물론 단결정의 값에 비하면 낮은 수치이기는 하나, 이는 주로 STO 기판과 LBSO 박막 사이의 5 % 정도의 격자 상수 불일치에 기인하여 발생한 전위 밀도 (threading dislocation)에 의함임을 알 수 있었다. 또한, LBSO 박막은 단결정의 특징과 같이 열 안정성이 뛰어남을 알 수 있었고, 특히 온도의 변화에 따라서 전하 농도가 변하지 않는 축퇴된 반도체 (degenerate semiconductor) 의 특징을 보임을 확인하였다.

이러한 LBSO 박막의 우수한 성질을 이용하여, 최근에 BSO 기반의 필드-이펙트 트렌지스터 및 *pn* 접합 다이오드와 기초 소자에 대한 연구가 활발하게 일어나고 있으며, 이를 통하여 많은 종류의 광전 소자 연구로 확장되고 있다. 그 중 특히 *pn* 접합 다이오드의 경우, 고성능 다이오드를 위하여 다양한 BSO 기반의 *pn* 접합 다이오드가 연구되고 있다. 그러나 *n*-형 반도체의 대응 물질인 *p*-형 산화물 반도체의 경우 여전히 *n*-형 산화물 반도체에 비하면 굉장히 낮은 정공 농도를 보이는데, 이는 상온에서의 전하 생성이 낮아서 전자 농도가 10^{15} cm^{-3} 보다 낮은 값을 갖게 되기 때문이다. 또한, 정공 이동도의 경우 일반적인 홀 이펙트로 측정하기 힘든 낮은 수치를 보이는데, 산화물 전자 *p* 오비탈이 가장 높은 가전자대(valance band)에서 평평하여 정공 유효 질량이 높아지기 때문이다. 한편, *p*-형 전도성 반도체 중 *n*-형 BSO 시스템과 깨끗한 *pn* 접합 다이오드를 구성할 수 있는 연구는 그 자체로 굉장히 의미있는 결구이다. 그러나 BSO 기반의 *pn* 접합 다이오드의 연구는 아직 많은 결과가 보고되어 있지 않

은 상황이다. 이러한 상황에서 BSO 시스템을 이용하여 투명한 *pn* 접합 다이오드를 구성할 경우 한 번 구현되기만 하면 그 이후에는 우수한 성능을 가질 것으로 예상되어 추후 광전 소자 연구에 의미가 있을것으로 생각된다. 따라서, 우수한 성능의 *p*-형 전도성 반도체를 찾기 위하여 BSO 시스템 및 다른 물질계를 포함한 다양한 연구가 진행되는 것은 충분히 의미가 있는 일이다.

감마(γ)상의 요오드화 구리 (CuI) 는 직접 천이형 반도갭을 가지는 물질로 밴드갭 에너지가 약 3.1 eV 정도로 가시광선 영역에서 투명하며, *p*-형 산화물 반도체에 비하여 높은 정공 이동도를 가지기 때문에 투명 *p*-형 반도체 물질로 최근 각광받고 있는 반도체 물질이다. 이는 요오드가 가지는 전자 *p* 오비탈로 인하여 정공의 유효 질량이 작기 때문이다. 한편, 전기 전도성의 측면에서만 보면 *p*-형 산화물 반도체에서도 높은 전도도를 가지는 물질들이 많이 있으나, 이들 물질의 경우 대부분 도핑을 많이 하여 투명도가 떨어지기 때문에 광전 소자로 응용되기 어려운 점을 가지고 있다. 따라서, 산화물의 성능 지수 (figure of merit, FOM)로 정의되는 전기 전도도와 광학적 흡수율의 비율이 소자 응용에 중요한 지표 중 하나이다. 다시 말해서, 흡수율이 커지면 투과율이 낮아지기 때문에 FOM 이 커지고 전기 전도도와 투명도가 동시에 높아 소자 응용에 적합한 물질이 될 수 있다. 이러한 점에 착안하여, CuI 의 경우 *p*-형 전도성 반도체 물질로 필드-이펙트 트렌지스터, 발광 다이오드 및 UV 광센서 등과 같은 다양한 종류의 소자 응용으로 적합한 새롭게 떠오르는 물질이다.

CuI 박막의 증착을 위해서 구리(Cu) 박막을 증착한 뒤 요오드화 시키는 방법, 펄스 레이져 증착법, 열 증착법 및 스핀코팅 방법 등 다양한 방법이 연구되어 왔다. 이러한 여러 방법 중 가장 흔히 사용되는 방법은 Cu 박막의 요오드화 방법이었다. 그러나 이러한 요오드화 박막의 경우 요오드화 과정에서 Cu 와 CuI 사이의 약 5 배 정도의 큰 부피 차이로 인한 부피 팽창으로 거친 표면의 박막이 형성되기 쉬우며, 이 때문에 깨끗한 계면을 가지기 힘든 이유가 된다. CuI 분말을 이용한 열 증착법의 경우 우수한 막질을 가지는 CuI 박막을 합성할 수 있는데, 이 때 CuI 박막의 정공 농도, 정공 이동도 및 투명도가 높은 장점이 있다. CuI 박막의 물리적인 특성을 분석하기 위하여 우리는 가장 흔히 사용하는 Cu 박막의 요오드화 방법 및 CuI 분말의 열 증착법 두 방법을 모두 사용하여 CuI 박막 증착을 시도하였다.

나아가서 다이오드의 물리적 성질 확인을 위하여, 펄스 레이져 증착법을 이용하여 합성한 $BaSnO_{3-\delta}$ (001) 박막 위에 열 증착법을 이용하여 CuI (111) 박막을 증착하여 전체적으로 투명한 *p*-CuI/*n*-$BaSnO_{3-\delta}$ 이종접합 다이오드를 제작하였다. CuI 박막의 두께를 30 nm 에서 400 nm까지 변화시킴에 따라 정공 농도가 체계적으로 감소하여 6.0×10^{19} cm^{-3} 에서 1.0×10^{19} cm^{-3}로 변화하였고, 그에 따른 다이오드의 전류 정류 비율은 비례하여 약 10 에서 약 10^6으로 향상되었다. 이종접합 다이오드의 행동 양상을 묘사하기 위하여 에너지 밴드 다이어그램을 확인하였고, 타입-II 밴드 얼라인먼트를 하는 것을 확인하였다. 이를 통해 내부 전위(built-in potential)의 변화

가 CuI 박막 두께의 변화에 의한 정공 농도 변화로 발생하여 전류 정류 비율에도 영향을 미치는 것을 알 수 있었다. 가장 다이오드 성능이 좋은 CuI 박막 두께 400 nm 시료의 *p*-CuI/*n*-$BaSnO_{3-\delta}$ 다이오드의 경우 2 V 에서 6.75×10^5의 높은 전류 정류 비율과 1.5의 이상 계수를 보였다.

우수한 막질을 가지는 BSO 박막의 경우 종종 STO와 같은 특정 기판위에서 에피탁셜 박막으로 성장되어야 하는 제한적인 조건을 가지고, 800 °C 보다 높은 증착 온도를 가진다. 따라서, 플렉서블 소자와 같은 응용 연구를 위해서는 상대적으로 낮은 증착 온도에서 증착되어 CuI 박막과 접합가능하며 에피탁셜 박막이 아니더라도 우수한 막질을 갖는 새롭게 대체된 *n*-형 박막을 이용항 새로운 형태의 이종접합 다이오드의 연구가 필요한 상황이다. 이러한 이유로 우리는 새로운 형태의 비정질 반도체인 SiZnSnO (SZTO) 박막에 초점을 두고 연구를 시작하였다. SZTO 박막의 경우 광학적인 밴드갭 에너지가 3.7 eV 이상으로 높고, 필드 이펙트 전자 이동도가 약 38 $cm^2 V^{-1} s^{-1}$ 정도로 예측되는 *n*-형 반도체 물질이다. 또한, SZTO 박막의 경우 잘 알려진 *n*-형 반도체 박막인 InGaZnO (IGZO) 에 비하여 높은 실리콘-산소 결합 에너지로 인한 감소된 산소 공핍에 의하여 전기적 안정성이 뛰어난 장점이 있다. 한편, SZTO에 이용되는 실리콘과 주석의 경우 독성이 없고, 지구상에 풍부한 물질이기 때문에 소자로서의 또다른 장점을 갖고 있다. 따라서, 우리는 SZTO 박막을 투명 *n*-형 박막으로 도입하여 *p*-형 CuI 박막과 결합한 새로운 형태의 이종접합 다이오드에 대한 연구를 시작하였다.

구현된 *p*-CuI/*n*-SZTO 이종접합 다이오드의 경우 또다른 강점을 갖고 있는데, 바로 자가동력 UV 광센서로의 활용 가능하다는 점이다. 이는 CuI 박막이 직접천이형 밴드갭 에너지를 갖고 있고, 밴드갭 에너지가 3.1 eV 인 것에서 기인한 것으로 가시광선 영역에서는 투명하고 자외선 영역의 빛은 흡수하기 때문이다. 실제로 최근 *p*-형 CuI 박막과 다양한 형태의 *n*-형 물질들을 결합하여 광센서로 활용한 연구 결과들이 나오고 있다. 이렇게 CuI 박막을 이용한 *pn* 접합 다이오드를 통해 광센서를 제작할 경우 자가동력 특성과 자외선 영역에서 안정적인 빛 반응성을 갖는 것을 예상할 수 있다. 따라서, *p*-형 CuI 와 *n*-형 SZTO 박막을 이용하여 만든 다이오드는 플렉서블하면서도 투명한 UV 광센서의 구현을 위한 새로운 플랫폼으로 자리잡을 수 있을 것이다. CuI/SZTO 광센서 구현을 위해서는 먼저 다이오드의 성능과 물리적 특성을 정량적으로 분석하여 이해하고 에너지 밴드 얼라인먼트를 통하여 다이오드 계면이 광소자에 적합한지 여부에 대한 연구가 선행되어야 한다. 따라서, CuI/SZTO 다이오드의 체계적인 연구를 수행하고, 이를 바탕으로 나아가 광전류를 측정하여 자가 동력 UV 광센서르 활용가능한지 여부를 확인하였다. 구현된 다이오드의 접합 면적 변화에 따른 광센서 성능 변화를 분석하여 광센서에서 핀홀이 미치는 영향을 확인하고, 이들이 광전류 및 광센서에 미치는 영향이 누설 전류의 증가를 야기한다는 사실을 확인하였다.

위와 같은 실험적인 근거에 기반하여 우리는 CuI 박막이 새로운 *p*-형 반도체 물질로 떠오

르고 있으며, 상온 증착이 가능하여 여러 *n*-형 반도체 물질, 그 중에서도 특히 주석 산화물 기반의 *n*-형 반도체 물질과 결합할 경우 CuI 기반의 UV 광센서와 같은 광전 소자로 응용이 가능함을 제안하였다. 구현된 CuI/SZTO 다이오드의 경우 자가 동력 UV 광센서로 동작함을 확인하고, 비정질 물질 위에서도 우수한 막질을 가지고 상온 증착이 가능한 CuI 박막의 특성을 이용하여 플렉서블 소자로서 활용가능함을 확인하였다. 따라서, 신소재 반도체들을 활용하여 구현된 CuI/SZTO 다이오드의 경우 그 물리적 특성에 대한 체계적인 연구를 통하여 추후 다양한 형태의 광전 소자로 응용 가능함을 알 수 있다.

주요어 : 바륨 주석산화물, 실리콘으로 억제된 아연-주석 산화물, 요오드화 구리, *pn* 이종접합 다이오드, 전류 정류 비율, 자기 출력형 자외선 광센서

학번 : 2015-20346